Infrared Thermography-Based Heat Transfer Analysis and Thermal Boundary Layer Evaluation on Upscaled Models of Additively Manufactured Rough Surfaces

Supervisor

Prof. Gaetano IUSO

Dr.-Ing. Mats KINELL

Candidate

Fabio GISSI

In collaboration with

SIEMENS energy

24th July 2025

Stay hungry.
Stay foolish.

Abstract

Additive Manufacturing (AM), and in particular Laser Powder Bed Fusion (L-PBF), enables the fabrication of complex internal geometries that are not feasible with traditional manufacturing techniques such as casting or milling. This capability is especially beneficial for gas turbine components, where advanced cooling channel designs are required to sustain high thermal loads and improve overall engine efficiency. However, a direct consequence of the AM process is the formation of unique surface roughness (SR) patterns, which affect both pressure loss and convective heat transfer (HT) mechanisms. In particular, AM-induced SR tends to be irregular and highly stochastic in nature, deviating from traditional roughness characterizations based on sand grain analogs.

To better understand the effect of such SR on local heat transfer behavior, a dedicated experimental rig—the *Surface-Roughness-Heat-Transfer (SRHT)* rig—was developed at the *Fluid Dynamics Laboratory* of *Siemens Energy AB*. The rig enables the study of convective heat transfer on upscaled physical models of AM surfaces using infrared (IR) thermography, with air as the working fluid. Upscaled geometries are modeled from real AM surfaces using scanning electron microscopy and surface topography data, allowing detailed spatial evaluation of the local heat transfer coefficient (HTC).

In this study, the SRHT rig was extended to promote fully developed channel flow conditions and improved thermal diagnostics. With the upgraded facility, existing upscaled Aluminium and Inconel test objects were retested to re-evaluate previously obtained heat transfer data. A comprehensive repeatability analysis was conducted by varying the infrared camera positions to verify the robustness and spatial consistency of the HTC measurements.

Additionally, this work introduces—for the first time within the project—a systematic investigation of the thermal boundary layer development along the flow direction over AM-induced surface roughness. Boundary layer profiles were obtained through distributed surface temperature measurements and analyzed in conjunction with spatial HTC maps. This dual approach allowed deeper insight into the interplay between local flow behavior and convective heat transfer augmentation due to roughness features.

The results confirm the combined influence of increased effective surface area and roughness-induced turbulence on the heat transfer enhancement observed on AM sur-

faces. This study consolidates the infrared thermography methodology, validates the robustness of the experimental process, and extends the project's scope by integrating thermal boundary layer analysis into the heat transfer characterization framework.

Contents

Contents

List of Figures

List of Tables

Chapter 1

Introduction

This introductory chapter presents the motivation for the current study, followed by a review of the state-of-the-art research in the field. The chapter concludes by outlining the objectives of the thesis.

1.1 Motivation

Global energy consumption has nearly doubled over the past three decades and it is predicted it will keep on rising [89]. Fig. 1.1 illustrates that the majority of the world's energy production still relies on non-renewable sources such as coal, which significantly contribute to atmospheric pollution through the emission of greenhouse gases and nitrogen oxides. To mitigate climate change, global efforts are increasingly focused on expanding the share of renewable energy and minimizing the environmental footprint of existing energy sources, with the ultimate goal of achieving net-zero emissions by 2050.
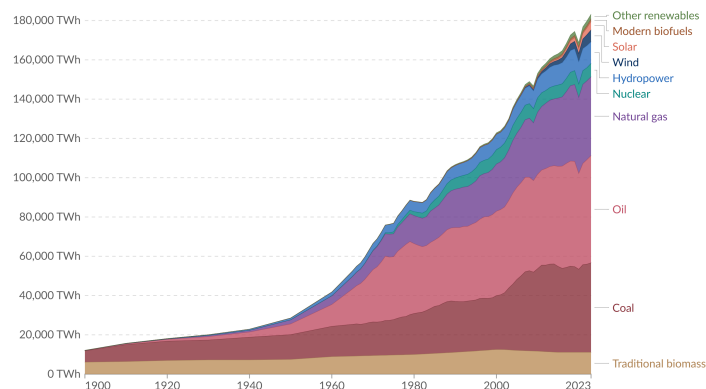
Figure 1.1: Global primary energy consumption by source [89]

Total energy demand spans three key sectors: electricity, heating, and transportation.

In this context, Land-Based Gas Turbines (LBGTs) play a pivotal role in energy supply, serving applications such as peak load coverage and baseload power generation. As internal combustion engines, gas turbines are used extensively across all three sectors. In gas-steam and combined heat and power plants, they are core components for electricity and thermal energy production. Additionally, gas turbines are employed in aircraft propulsion and marine power systems. Their widespread adoption stems from their high power density, broad power range, fuel flexibility, operational reliability, and low pollutant emissions. In line with these benefits, Siemens Energy AB is actively pursuing improvements in turbine efficiency while incorporating renewable and alternative fuels.

Over the past decade, the performance of Industrial Gas Turbines (IGTs) has significantly advanced, narrowing the gap with cutting-edge aerospace turbine technology. These improvements are largely driven by the development of high-temperature materials, advanced coatings, and innovative cooling designs, which together enable higher pressure ratios and turbine inlet temperatures (TITs) [33]. Modern gas turbines can now achieve TITs exceeding 2000 K, therefore they require efficient internal blade cooling systems. The advent of Additive Manufacturing (AM), particularly Laser Powder Bed Fusion (L-PBF), has further enabled the design and fabrication of complex internal cooling geometries to meet these stringent thermal requirements.

Despite the advantages of AM, the L-PBF process inherently produces rough and irregular surface finishes [82]. While external surfaces can often be post-processed through machining, internal features, such as narrow cooling channels, are generally inaccessible for such treatments [84]. These rough surfaces can trigger early boundary layer transition, increase momentum losses, and induce flow separation, all of which can contribute to elevated pressure losses [86, 88]. However, the same surface roughness may enhance convective heat transfer within cooling channels, potentially improving overall turbine thermal performance. While extensive research has been conducted on friction factors and momentum transfer in rough AM channels, the specific effects on convective heat transfer are less comprehensively understood. Addressing this knowledge gap is the primary objective of this study.

1.2 Literature Review

Extensive research has been devoted to investigating the relationship between surface roughness, flow properties, and heat transfer. Foundational studies by Hagen [1] and Darcy [2] revealed that surface roughness increases pressure losses due to elevated drag forces and blockage effects [7]. Building on these observations, Darcy introduced a relationship between head loss and friction in pipe flow, which was later refined into the well-known Darcy–Weisbach equation. This equation incorporates the Darcy friction factor f_D, whose behavior depends on both the Reynolds number and the roughness level of the pipe surface.

To better understand this relationship, Nikuradse [12] conducted systematic exper-

iments by lining pipe walls with uniform sand grains, glued as closely as possible onto smooth surfaces, creating the so-called sand grain roughness (k_s). He measured the pressure losses for various Re and k_s/D_h values. Subsequently, Schlichting [7] expanded on this by testing a variety of roughness elements (e.g., cones, rivets, spherical segments), introducing the concept of "equivalent sand grain roughness", defined as the height of uniform sand grains yielding the same friction loss as the actual rough surface. These studies, along with contributions from von Kármán [6] and Colebrook-White [9], culminated in the development of the Moody diagram [11]. This diagram relates f_D, Re, and relative roughness k_s/D_h, showing that friction factor decreases with increasing Re until it reaches a constant value in the fully turbulent regime. Higher relative roughness also causes earlier transition to turbulence, resulting in greater friction losses. However, although k_s/D_h remains a useful descriptor, it inadequately captures the complexity of real, irregular surfaces. Later reviews by Bons [48] and Kadivar et al. [88] highlight these limitations, especially in the context of artificial external roughness.

While these early works focused mainly on flow resistance, heat transfer was addressed later due to the increased difficulty in high-precision thermal measurements [17]. One of the first heat transfer studies in hydraulically rough pipes was conducted by Cope [10], who investigated pyramid-structured rough surfaces. Using water as the working fluid, he found that rough pipes exhibited higher heat transfer rates than smooth ones under equivalent pressure drops. Later, Dipprey & Sabersky [17] extended these findings by exploring heat and momentum transfer in pipes with sand grain roughness over a wide range of Re and Pr values. They reported heat transfer coefficient (HTC) enhancements of up to 270%, albeit generally accompanied by even larger increases in friction. With their experimental data, Dipprey & Sabersky made a first approach to correlate surface roughness with the heat transfer performance, using a similar methodology that Nikuradse used with the friction factor. This publication inspired Dalle Donne & Meyer [23] to build on their methodology by correlating friction and HTC using the Stanton number for pipes with two-dimensional rectangular rib roughness. Much of the research from the 1950s to 1980s was linked to nuclear reactor cooling applications, where artificial roughness was favored for its controllability.

Despite the importance of friction factor and flow features, the present work aims at exploring heat transfer enhancement over additively manufactured (AM) surfaces, particularly focusing on local effects induced by roughness features. Ventola et al. [57] found HTC enhancements up to 73% (average 63%) on external L-PBF-fabricated surfaces. However, their study was limited to external flows. More comprehensive internal flow investigations were carried out by Snyder, Stimpson, and Thole at Pennsylvania State University. In one of their early studies [63], they found that build orientation significantly affected pressure losses, while heat transfer remained largely unchanged. Stimpson et al. [64] later demonstrated that AM roughness increased both pressure drop and HTC in rectangular channels, though not proportionally. Subsequently, they developed an empirical correlation relating the arithmetic mean rough-

ness to Nikuradse's k_s, along with a Nusselt number prediction model for AM channels [69]. Other studies questioned the reliability of arithmetic mean roughness (R_a); for instance, Townsend et al. [65] and Han et al. [79] highlighted the superior predictive capability of mean roughness depth R_z in describing AM surfaces.

Beyond experimental research, Computational Fluid Dynamics (CFD) has been widely used to analyze AM surface effects. Hanson et al. [75] reconstructed surface topographies of scaled AM cooling channels using X-ray computed tomography (CT) and laser displacement scanning (LDS). Their results emphasized the difficulty of generating statistically representative analog surfaces and highlighted limitations of RANS models in predicting flow separation and friction.

With increasing computational power, Direct Numerical Simulation (DNS) has become more prevalent for smooth-wall turbulence studies at high Re. However, DNS of rough surfaces remains limited due to the need for extremely fine meshes [52]. To address this, Garg et al. [108, 109] employed wall-resolved Large-Eddy Simulations (LES) to study AM roughness in pipes. Their findings revealed that temperature profiles are more sensitive to roughness than velocity profiles. Specifically, the inner-scaled temperature roughness function $\Delta\theta^+$ exhibited greater deviations than the velocity counterpart ΔU^+, underscoring the different behaviors of momentum and thermal boundary layers.

Although significant progress has been made, the relationship between surface roughness and convective heat transfer remains only partially understood. Peak heat transfer generally occurs where thermal boundary layers are thinnest, typically in windward impingement regions [76], whereas separation zones lead to thicker boundary layers and diminished HTC. Numerous empirical correlations have been proposed to link Nu, Re, f_D, and Pr, but their effectiveness depends on the specific flow regime. Furthermore, there is still no consensus on the most effective metric for characterizing AM roughness or translating it into equivalent sand grain roughness.

1.3   Research Objectives

The fluid dynamic investigation presented in this thesis focuses on understanding the heat transfer enhancement mechanisms that influence rough surfaces, such as those found in additively manufactured (AM) micro-channels. The main objective is to expand the current understanding of how AM-induced roughness influences convective heat transfer and to address the following research questions:

- *How does the surface roughness produced by AM affect the overall flow behavior and mean flow properties in the channel?*

- *How does the altered flow behavior enhance the heat transfer performance, and how are they correlated?*

- *What are the dominant flow mechanisms or structures that significantly influence heat transfer?*

These aspects are critically important and must be carefully evaluated during the design phase of various thermofluidic components. To improve the accuracy of predictions for key quantities such as pressure loss and heat transfer, extensive research has been carried out at the *Fluid Dynamics Laboratory* of *Siemens Energy AB* in Finspång, Sweden.

A *Quasi-Steady State Heat Transfer (QSSHT)* rig was developed to investigate real-size AM cooling channels and to evaluate how key parameters, such as the Darcy friction factor f_D and the Nusselt number Nu, vary with Reynolds number Re and Prandtl number Pr. The experimental campaign covered various channel lengths and diameters, different materials (including *Aluminium*, *Inconel 939*, and *Stainless Steel*), and multiple printing orientations. Both water and air were used as working fluids to span a wider range of Prandtl numbers. Results from this rig are reported in Pagani [99], Venturi [104], Lehmann [103] and Brugnera [107]. Although the QSSHT rig provides reliable bulk data, it lacks the spatial resolution necessary for detailed analysis of local heat transfer phenomena.

To address this limitation, a *Surface Roughness Heat Transfer (SRHT)* rig was designed to provide spatially resolved measurements of the convective heat transfer coefficient and Nusselt number. The rig focuses on specific features such as surface peaks, valleys, and flow separation regions. The aim is not only to identify how AM-induced roughness enhances local heat transfer, but also to determine which roughness parameters most strongly influence this behavior.

Initial work by Lehmann [103] validated the SRHT rig using smooth channels, followed by testing a coarse analogue surface reconstructed from Scanning Electron Microscope (SEM) data of an *Inconel 939* micro-channel produced via L-PBF with a 90° build orientation. His results showed increased heat transfer in rough regions, particularly on upstream-facing elements, with effects extending downstream. Wen [105] later refined the analogue surface by correcting statistical deviations and geometric fidelity to better match the original SEM profile, leading to improved agreement with QSSHT data. Additional analogue surfaces were developed and tested by Brogliato [106] and Tamagnini & Agostino [114], using Aluminum samples.

Despite these advancements, an important gap remained in understanding how roughness affects the flow field itself. To address this, a dedicated Particle Image Velocimetry (PIV) facility was built in 2024 [111, 114]. This setup allows for direct visualization of boundary layer interactions with the same upscaled models used in the SRHT-rig. Preliminary tests by Pedreño Marin [111] and Brogliato [106] suggested that heat transfer may be reduced in the areas downstream of roughness elements due to the presence of vortices or recirculation zones. However, these studies were limited by insufficient channel length, raising concerns about whether fully developed flow conditions were achieved.

The present work addresses these limitations by upgrading the experimental setup and focusing on the development of the thermal boundary layer over AM roughness. Special attention is given to characterizing the influence of roughness-induced turbu-

lence and identifying which roughness set of parameters best correlate with friction factor f_D and the Nusselt number Nu under fully developed flow conditions.

1.4 Thesis Outline

Chapter 2 will introduce the theoretical background necessary for this study, including fundamental notions about gas turbines, additive manufacturing, heat transfer, boundary layers, and channel flow. Chapter 3 will focus on describing the experimental methodology. It will cover the SRHT rig setup, the infrared thermography system for convective heat transfer measurements, and the data processing techniques.

Chapter 4 will present the experimental results, including validation procedures and key findings related to flow behavior and heat transfer. Finally, Chapter 5 will conclude the thesis by summarizing the main outcomes and proposing potential directions for future research.

Chapter 2

Theoretical Background

This chapter provides an overview of the fundamental physical principles necessary to support the experimental investigation conducted in this thesis.

The discussion begins with a review of gas turbine operation and the state-of-the-art in cooling channel technologies, establishing the rationale for employing Additive Manufacturing (AM) in the production of turbine blades. A concise introduction to AM techniques is then presented, including a discussion of the surface roughness (SR) typically induced by such processes. Understanding this roughness is essential for reconstructing analogue surfaces based on roughness measurements.

The chapter then addresses the governing mechanisms of heat transfer (HT), providing the background required to explain the heat transfer enhancement observed on AM surfaces. Emphasis is placed on the use of Infrared Thermography as a diagnostic tool for non-intrusive wall temperature measurement in the test facility.

Subsequent sections examine boundary layer theory, with particular attention to internal channel flow and the impact of rough surfaces on hydrodynamic and thermal development. Finally, fundamental concepts related to flow and temperature measurement techniques, specifically Hot-Wire Anemometry and thermocouple instrumentation, are introduced to support later discussion of experimental procedures.

This theoretical framework is intended to establish a robust foundation for analyzing convective heat transfer over upscaled AM rough surfaces reconstructed from surface data obtained via Scanning Electron Microscope (SEM) measurements.

2.1 Gas Turbine

Industrial gas turbines belong to the category of thermal turbomachinery and are widely used for electricity production, with power outputs ranging from a few kilowatts up to 600 megawatts [92].

Among various power generation technologies, gas turbines stand out for their reliability, availability, and operational versatility across a broad range of applications. Although these machines are complex and require significant engineering effort during development, their structure and working principles remain relatively straightforward.

Gas turbines generate power by converting the chemical energy stored in fuel into mechanical energy through a combustion process. This energy conversion is governed by a thermodynamic cycle.

In a typical internal combustion gas turbine, which is an air-breathing thermal engine, ambient air enters the intake and is compressed by the axial or centrifugal compressor. This compression increases both pressure and temperature. The compressed air then enters the combustion chamber, where fuel is injected and combusted, leading to a substantial rise in temperature and internal energy. The high-energy gas mixture subsequently expands through the turbine stages, driving the rotor and producing mechanical work. The working fluid is then discharged through the exhaust system [32].

In Combined Cycle Power Plants (CCPPs), the hot exhaust gases exiting the gas turbine are further utilized for steam generation in a Heat Recovery Steam Generator (HRSG) or to provide thermal energy for heating applications, such as district heating systems.
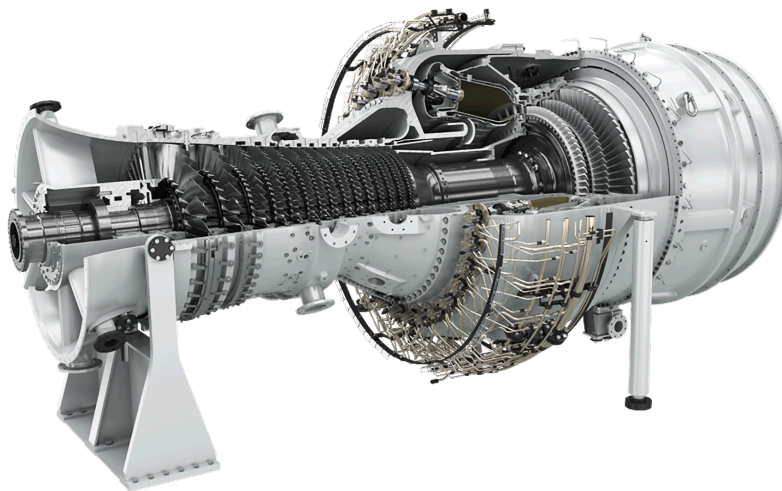
Figure 2.1: A modern land-based gas turbine used for electric power production. This is Siemens Energy's SGT-800 gas turbine, employed in industrial power generation and oil and gas applications. It can produce 62.5 MW with a gross efficiency of 41.1% and a NO_X emissions level of $15 \div 25$ ppmvd [91].

2.1.1 Gas Power Cycles

Most power-producing devices operate based on thermodynamic cycles, making the study of such cycles a fundamental aspect of thermodynamics. The analysis of real cycles is often complicated by factors such as friction, heat losses, and the limited time available for reaching thermodynamic equilibrium. To facilitate analysis, these real cycles are often idealized by removing internal irreversibilities and complexities. The resulting simplified model, made entirely up by internally reversible processes, is known as an *ideal cycle*.

Several thermodynamic cycles are relevant to engineering applications. These include:

- the *Carnot* cycle, composed of four entirely reversible processes;

- the *Otto* cycle, representing the ideal cycle for spark-ignition internal combustion engines;

- the *Diesel* cycle, which models compression-ignition engines;

- and the *Brayton* cycle, which is the ideal cycle for gas turbine engines.

The *Otto* and *Diesel* cycles are typically found in reciprocating engines, referred to as *intermittent* or *alternative* engines because they deliver power in cycles. In contrast, the *Brayton* cycle operates in a continuous manner and is suited for open-cycle power generation systems, such as gas turbines.

A comparison of these cycles on a pressure-volume ($p-v$) diagram is shown in Fig. 2.2. It is evident from the diagrams that combustion in the *Brayton* cycle occurs at constant pressure, whereas in the *Otto* cycle, it occurs at constant volume.

(a) *Otto* cycle   (b) *Brayton* cycle
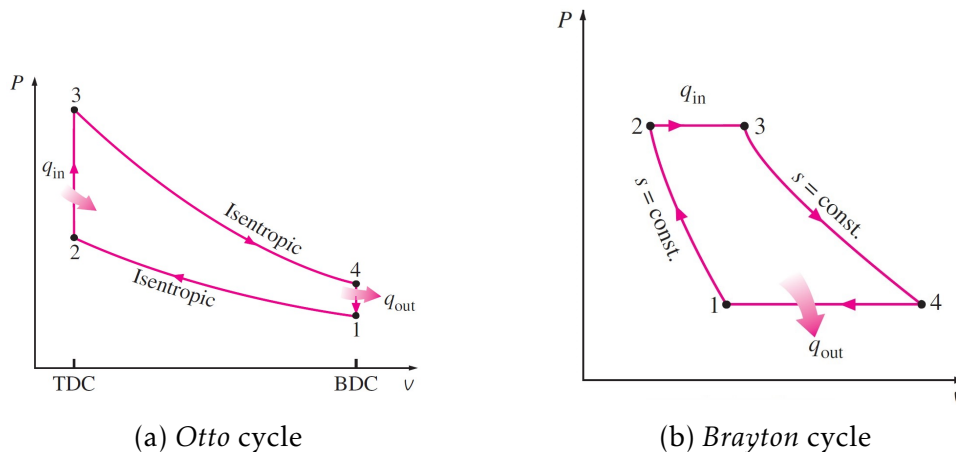
Figure 2.2: $p - v$ diagrams of the intermittent *Otto* cycle and continuous *Brayton* cycle [42]

As these diagrams represent idealized cycles, several simplifying assumptions are made:

1. The air mass flow is significantly greater than the fuel mass flow: $\dot{m}_a \gg \dot{m}_f$.

2. The flow is homogeneous and frozen, meaning that its composition does not change during the cycle.

3. The compressor and turbine have equal pressure ratios: $\frac{p_2}{p_1} = \frac{p_3}{p_4}$.

4. The working fluid is assumed to behave as a calorically and thermally perfect gas, implying constant specific heats:

$$c_p \neq f(T), \qquad \gamma \neq f(T), \qquad \text{with } \gamma = \frac{c_p}{c_v}$$

5. There are no pressure losses, and all adiabatic processes are considered isentropic, i.e., all components operate at 100% efficiency.

2.1.1.1 Brayton Cycle: The Ideal Cycle for Gas-Turbine Engines

The Brayton cycle was first proposed by George Brayton for use in a reciprocating oil-burning engine developed around 1870 [39]. Today, it is applied exclusively to gas turbines, where both compression and expansion are carried out using rotating machinery. Gas turbines typically operate on an open cycle, as shown in Fig. 2.3(a). Fresh air at ambient conditions is drawn into the compressor, where its pressure and temperature are increased. The high-pressure air is then directed into the combustion chamber, where fuel is burned at constant pressure. The resulting high-temperature gases enter the turbine, expand to atmospheric pressure, and produce mechanical work. The exhaust gases are expelled rather than recirculated, which characterizes the system as an open cycle.

(a) Open cycle   (b) Closed cycle
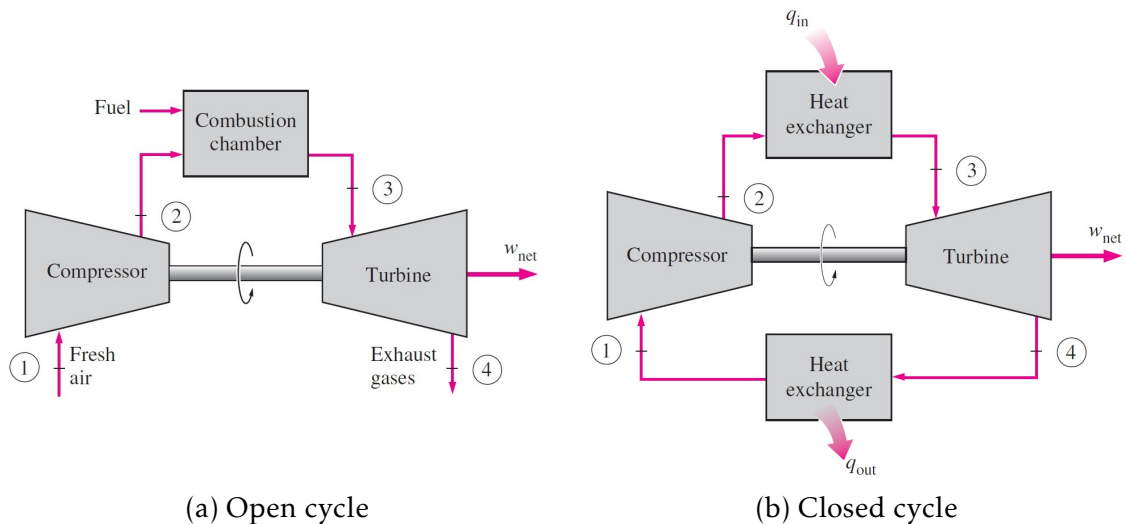
Figure 2.3: Schematic representation of gas turbine cycles [39]

The open gas-turbine cycle can be modeled as a closed cycle, as shown in Fig. 2.3(b),

by applying air-standard assumptions. In this model, the combustion process is replaced by a constant-pressure heat addition from an external source, and the exhaust process is replaced by a constant-pressure heat rejection to the surrounding environment.

The ideal Brayton cycle consists of four internally reversible processes:

1-2: Isentropic compression (in a compressor)

$$w_{\text{in}} = h_2 - h_1 = c_p(T_2 - T_1) > 0$$

2-3: Constant-pressure heat addition

$$q_{\text{in}} = h_3 - h_2 = c_p(T_3 - T_2) > 0$$

3-4: Isentropic expansion (in a turbine)

$$w_{\text{out}} = h_4 - h_3 = c_p(T_4 - T_3) < 0$$

4-1: Constant-pressure heat rejection

$$q_{\text{out}} = h_1 - h_4 = c_p(T_1 - T_4) < 0$$

As seen in Fig. 2.4(a), the isobaric lines $p_1 = p_4$ and $p_2 = p_3$ diverge, indicating that the work output from expansion exceeds the work input required for compression. This results in a net work output:

$$w_{\text{net}} = w_{\text{out}} - w_{\text{in}}$$

or equivalently:

$$w_{\text{out}} = w_{\text{in}} + w_{\text{net}}$$

Components such as compressors, turbines, and heat exchangers in a gas turbine typically operate continuously for extended periods, often several months, before scheduled maintenance. Thus, they are appropriately modeled as *steady-flow devices*.

(a) $T - s$ diagram   (b) $p - v$ diagram
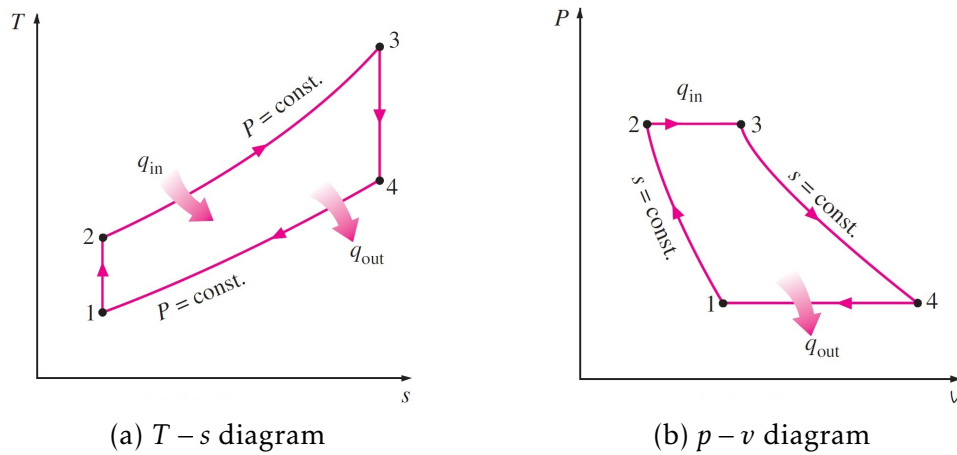
Figure 2.4: $T - s$ and $p - v$ diagrams of the ideal Brayton cycle [39]

Neglecting changes in kinetic and potential energies, the energy balance for a steady-flow process becomes:

$$(q_{in} - q_{out}) + (w_{in} - w_{out}) = h_{exit} - h_{inlet}$$

From this, the heat transfers are:

$$q_{in} = h_3 - h_2 = c_p(T_3 - T_2)$$
$$q_{out} = h_4 - h_1 = c_p(T_4 - T_1)$$

Under cold-air-standard assumptions, the thermal efficiency becomes:

$$\eta_{th,Brayton} = \frac{w_{net}}{q_{in}} = 1 - \frac{q_{out}}{q_{in}} = 1 - \frac{c_p\,(T_4 - T_1)}{c_p\,(T_3 - T_2)} = 1 - \frac{T_1(T_4/T_1 - 1)}{T_2(T_3/T_2 - 1)}$$

Given that processes *1-2* and *3-4* are isentropic, and assuming $p_2 = p_3$ and $p_4 = p_1$, the following equation is derived:

$$\frac{T_2}{T_1} = \left(\frac{p_2}{p_1}\right)^{(\gamma-1)/\gamma} = \frac{T_3}{T_4}$$

Substituting into the efficiency relation gives:

$$\eta_{th,Brayton} = 1 - \left(\frac{T_4}{T_3}\right) = 1 - \frac{1}{r_p^{(\gamma-1)/\gamma}} \tag{2.1}$$

where $r_p = p_2/p_1$ is the *pressure ratio* and $\gamma = c_p/c_v$ is the *specific heat ratio*.

Equation (2.1) shows that the thermal efficiency of the ideal Brayton cycle increases with both the pressure ratio and the specific heat ratio of the working fluid. This trend is consistent with the behavior of actual gas turbines. A plot of thermal efficiency versus pressure ratio is shown in Fig. 2.5, assuming $\gamma = 1.4$, typical of air at room temperature.

The working fluid (air) in gas turbines serves two purposes: it provides oxygen for combustion and it acts as a coolant to maintain component temperatures within operational limits. Air-to-fuel mass ratios of 50:1 or higher are not uncommon, and modeling combustion gases as air introduces negligible error.

Gas turbines are widely used in two main applications: aircraft propulsion and electric power generation. In aviation, the turbine produces just enough power to operate the compressor and auxiliary equipment, while thrust is generated by high-velocity exhaust gases. In power generation, gas turbines operate in simple or combined cycle configurations. In combined cycles, exhaust gases heat water in a Heat Recovery Steam Generator (HRSG) to power a steam turbine. Closed-cycle Brayton systems are also

used in nuclear power plants, where helium or other ideal gases may replace air as the working fluid [39, 53].

The thermal efficiency of a gas turbine is strongly influenced by the Turbine Inlet Temperature (TIT), which is enhanced by improvements in heat transfer mechanisms. Additive Manufacturing (AM) enables the creation of intricate internal geometries that enhance cooling, facilitating higher TIT values and improving overall cycle performance.
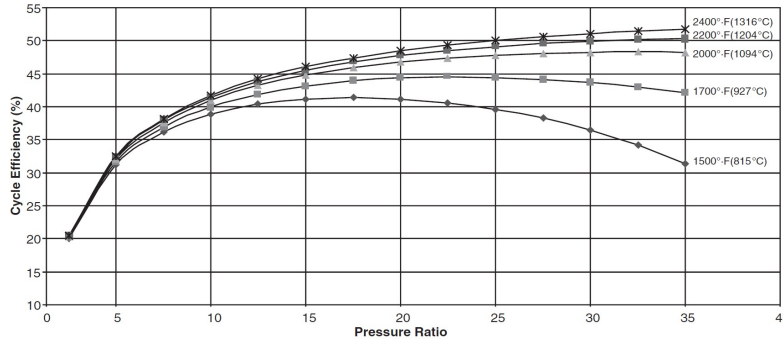
Figure 2.5: Cycle efficiency as a function of compressor pressure ratio and TIT [33]

2.1.2 Turbine Blade Cooling Methods

Current state-of-the-art gas turbine development is primarily focused on increasing the Turbine Inlet Temperature (TIT), as this significantly enhances thermal efficiency. According to Eq. (2.1), the efficiency of a gas turbine is strongly influenced by both TIT and the pressure ratio r_p across the compressor. While increasing r_p contributes to improved efficiency, the effect is modest (approximately proportional to $r_p^{0.3}$). In contrast, increasing TIT has a more substantial impact.

Over recent decades, TIT has steadily risen from approximately $540°C$ in the 1940s to over $1450°C$ in modern turbines [40, 101]. These increases exceed the melting point of conventional materials and have been made possible through advanced material development and innovative cooling techniques. Examples include ceramic thermal barrier coatings and the use of compressor discharge air to cool turbine blades. As TIT rises, combustion temperature must increase to offset the diluting effect of the cooling air, making efficient cooling air usage crucial to achieving net cycle performance gains.

Consequently, two critical aspects in modern turbine blade cooling are augmented internal cooling and external film cooling [39, 102]. These are essential for both aviation and stationary power generation applications.

It is worth noting that the temperature across a turbine blade is non-uniform, it varies from the leading to the trailing edge and from root to tip. The highest temperatures typically occur at the stagnation point. Therefore, cooling strategies must be tailored to specific regions of the blade.
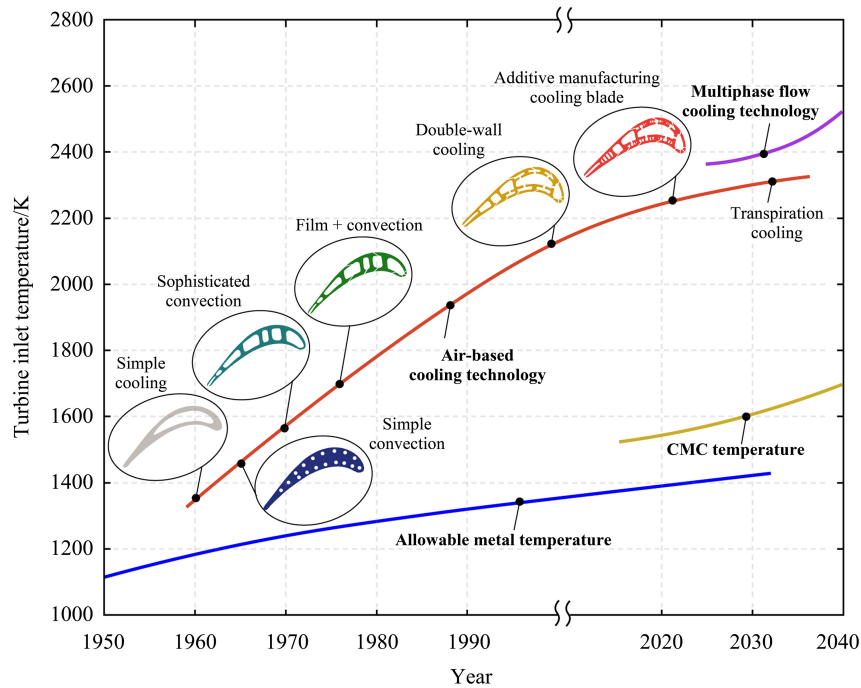
Figure 2.6: Evolution of gas turbine temperatures with cooling techniques over time [100]
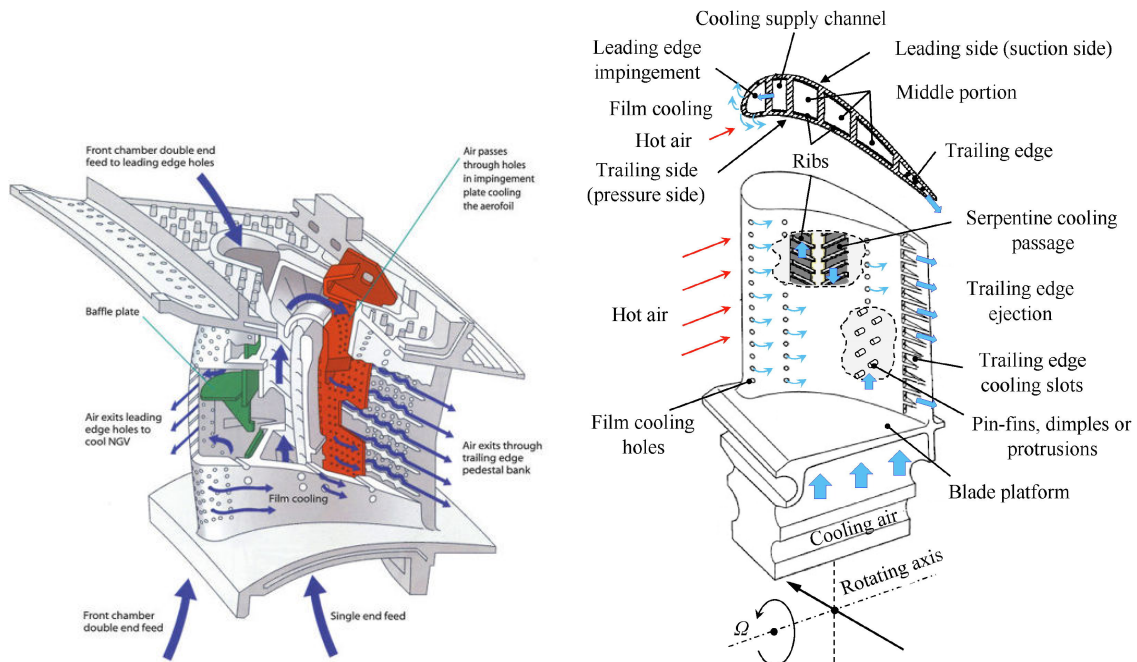
(a) Path of the flow inside the blade [120]

(b) Typical techniques for turbine blade cooling [95]

Figure 2.7: Schematic representation of cooling techniques in gas turbines

Turbine blade cooling combines internal and external mechanisms. Internal cooling channels embedded within the blade extract heat via convection. Techniques include ribbed serpentine channels, impingement jets, and pin-fin arrays. External cooling, commonly known as film cooling, discharges air through holes on the blade surface to form a protective film that insulates against hot combustion gases. These methods must minimize the consumption of compressor discharge air, as diverting this air reduces overall thermal efficiency and power output [40, 68, 73].

2.1.2.1 Internal Cooling

Internal cooling strategies involve the circulation of air or liquid through complex internal geometries. The use of Additive Manufacturing (AM) enables the creation of intricate channel designs that enhance surface area and heat transfer rates [73, 101].

In **convection cooling**, the coolant flows through internal passages. Heat is transferred first via conduction from the blade material to the internal surface and then via convection to the coolant. Early implementations utilized single-pass cooling (hub-to-tip flow), whereas modern blades feature multi-pass serpentine geometries for improved effectiveness.

Impingement cooling is a high-intensity variant of convection cooling. Coolant is discharged perpendicularly onto the internal walls of the airfoil via discrete orifices. After impact, the coolant continues downstream toward the trailing edge, aiding in internal heat extraction. This method is particularly suited for localized high-temperature regions, such as the leading edge.

2.1.2.2 External Cooling

External cooling is critical for increasing the lifespan of components in the hot section. This approach generally involves creating a thin film of coolant on the blade's surface, providing a thermal barrier between the hot gases and the metal surface. However, this benefit comes at the cost of extracting air from the compressor, which negatively impacts cycle efficiency [85].

In **film cooling**, coolant air is ejected from internal passages through surface holes or slots to create a cooling film over the blade. In **full blade film cooling**, the entire surface is covered with closely-spaced holes to ensure uniform coolant distribution and better mixing with the boundary layer.

Transpiration cooling shares the same principle as film cooling, forming a cooling layer, but uses a porous material instead of discrete holes. This allows a more uniform distribution of coolant across the surface. While this technique offers significant thermal protection, it has not yet been implemented in commercial turbine applications [110].

Thermal Barrier Coatings (TBCs) involve applying insulating ceramic layers to tur-

bine components. These coatings have very low thermal conductivity and can support steep thermal gradients, reducing the metal surface temperature by up to $100°C$. The white layer visible in Fig. 2.8(b) represents such a coating.

(a) Turbine blade with discrete film cooling holes [45]

(b) Turbine blade with full-surface film cooling [119]
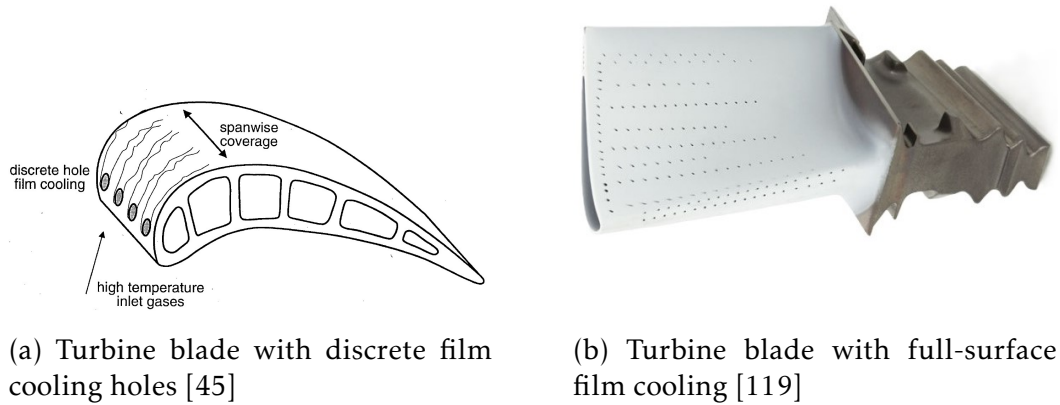
Figure 2.8: Comparison of discrete vs full blade film cooling

2.2 Additive Manufacturing

Traditional manufacturing processes for turbine blades include casting or milling. In these subtractive methods, the complexity of cooling channels that can be integrated into blade geometry is limited. Additive Manufacturing (AM), however, allows for more intricate cooling designs since the component is built layer by layer. This section introduces the AM process.

AM has evolved rapidly over the last decade and gained significant traction in various industries, including automotive, aerospace, medicine, sports, and construction [74]. As mentioned, AM facilitates complex designs for internal turbine blade cooling, thereby enhancing cycle efficiency, reducing fuel consumption, and increasing power output. Understanding the core principles of AM is thus fundamental to this thesis. Studying upscaled analogue surfaces of AM cooling channels requires insight into both surface roughness (SR) measurements and the AM techniques used in turbine blade production.

The following sections introduce key AM methods and explain the concept and quantification of AM-induced roughness.

2.2.1 Additive Manufacturing Fundamentals

Additive Manufacturing, or 3D printing, was developed in the early 1980s by Charles Hull, initially called stereolithography. During the 1990s, AM gained industry recognition for rapid prototyping in fields such as automotive, aerospace, and healthcare [54].

Unlike conventional CNC milling and turning, which are subtractive, AM builds components by depositing and fusing material. Functionally, 3D printing resembles inkjet printing but uses metal or polymer to build a digital model layer by layer into a physical object.

Every AM process starts with a 3D CAD model, converted into an STL (Standard Triangle Language) file. Unlike CAD, STL contains only triangulated surface geometry. The model is then sliced into thin layers ($20\,\mu m$ to $1\,mm$) and sent to the printer. Each layer is formed by selectively melting or sintering material using a heat source, typically a laser. After fabrication, surface treatments are often needed [60].
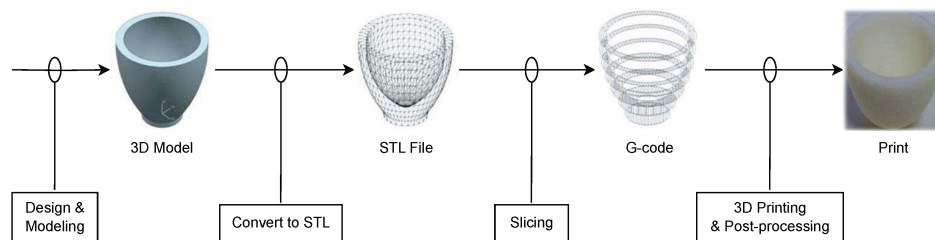
Figure 2.9: Basic steps in the additive manufacturing process [115]

2.2.2 Additive Manufacturing Technologies

Originally limited to polymers, AM now includes metals thanks to advances in CAM and laser technologies. This has expanded AM from prototyping to full-scale production.
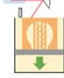
Process	Acronyms	Feedstock	Material	Bonding and join
Extrusion (or fused filament fabrication or fused deposition modeling)	FFF, FDM	Filament, rod, pellets	Polymer	Fused with heat
Photopolymerization (or stereolithography)	SLA	Liquid	Photopolymer, metal, ceramics, composite	Cured with laser, projector, UV light
Material Jetting (or Binder Jetting)	MJ (BJ)	Powder, liquid	Ceramic, wax, polymer, metal, sand	Cured with UV light, heat
Laminated Object Manufacturing (or Sheet Lamination)	LOM	Sheet	Paper, metal, polymer	Joined with agent, heat and pressure
Selective Laser Melting	SLM	Powder	Metal	Fused with laser and electron beam
Directed Energy Deposition	DED, EBM	Wire, powder	Metal	Fused with laser and electron beam

Figure 2.10: Overview of AM processes [80]

A summary of current AM methods is shown in Fig. 2.10, with key technologies described below [115]:

- *Fused Deposition Modeling (FDM)*: Common in consumer printers. A heated extruder melts a polymer filament, layering 2D patterns to build a 3D object. Strength is lower than other techniques, but reinforced filaments (e.g., carbon or metal-filled) offer improvements.

- *Stereolithography (SLA)*: Uses a UV laser to cure photoreactive resin in a vat. Offers high precision but limited mechanical strength and component size.

- *Powder Bed Fusion (PBF)*: Preferred in industry for its superior mechanical properties and material flexibility. A laser melts or sinters powder layers (e.g., in *Selective Laser Melting* or *Selective Laser Sintering*).
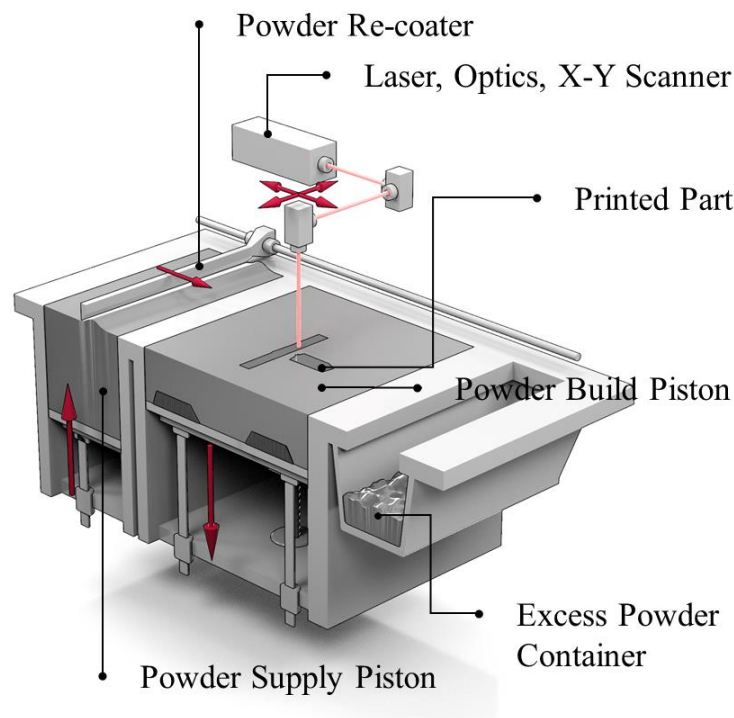
Figure 2.11: Schematic of a typical Selective Laser Sintering 3D printer [83]

2.2.2.1   Laser Powder Bed Fusion (L-PBF)

Powder Bed Fusion (PBF) is a type of Additive Manufacturing (AM) 3D-printing technique that enables the production of parts directly from their digital design files. It involves selectively melting a metallic powder layer by layer using a focused energy source, such as a laser or an electron beam, depending on the specific process (e.g., SLM method). After each layer is melted and solidified, a new layer of powder is spread over the surface, and the energy source resumes melting according to the desired geometry. This sequence is repeated until the entire component is built. The powder

that remains unfused can be collected and recycled for future use. Common technologies in this category include *Selective Laser Sintering* (SLS), *Selective Laser Melting* (SLM), and *Electron Beam Melting* (EBM). These methods are well known for producing near-net-shape components using a wide selection of materials and enabling the fabrication of complex geometries such as lattice structures, which can reduce the overall weight of the part while preserving structural performance. Due to these advantages, there is a strong demand for PBF processes in the aerospace sector and other industries where geometrical complexity provides a significant performance benefit. As an example, Siemens received the *Emerging Technology Award* from the American Society of Mechanical Engineers (ASME) for its innovative use of additive manufacturing in the production of gas turbine blades.
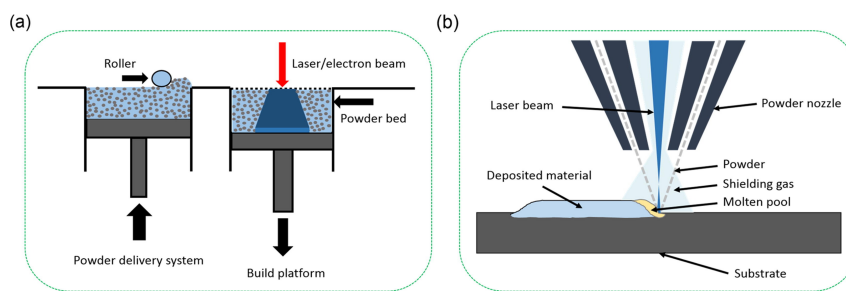
Figure 2.12: Powder bed fusion [94]: (a) side view; (b) magnified view on the single solder point

Despite its advantages, PBF presents some limitations related to surface roughness and fatigue resistance when compared to traditionally machined parts. Several process-related parameters affect the final surface quality, especially due to localized heat accumulation, which can cause unwanted powder particles to adhere to the surface. In particular:

- *Part location on the build plate*:
  If two parts are placed too close to each other, heat may be conducted through the powder between them, possibly causing unintended powder melting and clogging of small internal features, such as cooling channels.

- *Angle between the feature and the build plate*:
  The inclination angle influences the overlap between successive layers, and this can affect the resulting surface roughness.

- *Upskin/Downskin orientation*:
  Downskin surfaces tend to have a more pronounced roughness due to the upward heat transfer into previously deposited layers, which are thinner and therefore more easily overheated. This leads to powder particles adhering more readily to the component's underside.

- *Wiper performance*:
  The ability of the recoater or wiper to evenly spread the powder layer can in-

fluence the uniformity of the surface finish. Inconsistent spreading results in localized surface roughness variations.

- *Argon stream direction*:
  The entire process is carried out in an inert atmosphere to prevent oxidation. Argon flows from one side of the build plate to the other, dragging along spatter and oxide debris. This results in a rougher surface on the outflow side of the plate.

With more than 150 interdependent parameters involved in L-PBF processes [98], checking the final quality of the component remains a complex challenge. A deep understanding of the interplay between process settings, part orientation, thermal history, and inert gas flow is essential to mitigate surface defects and ensure the desired performance of the printed parts.

2.2.3   AM-induced Surface Roughness

A characteristic feature of components produced via Laser Powder Bed Fusion (L-PBF) is their relatively high surface roughness (SR), which can significantly affect both pressure losses and heat transfer performance. While SR on external surfaces can often be mitigated through post-processing techniques, this becomes much more challenging, or even infeasible, in internal features with small cross-sectional areas, such as cooling channels in turbine blades.

A representative example of the SR observed on L-PBF-manufactured components is shown in Fig. 2.13. The surface is populated by powder particles of various sizes, some of which are fused together (A), while others only weakly adhere to the surface (B, C), resulting in an entirely stochastic distribution. This phenomenon arises because some particles undergo partial melting or sintering, leading to irregular bonding and surface textures. Such behavior can be attributed to several process parameters, including laser power, scan speed, layer thickness, part placement on the build platform, and printing direction [93].

Heat transfer enhancement is primarily associated with the increased surface area resulting from SR, which facilitates greater thermal exchange. Additionally, the manner in which particles interact with the surface further influences heat transfer behavior. For instance, particle C in Fig. 2.13 is more deeply embedded in the surface than particle B, establishing a superior thermal conduction path. This effect is particularly advantageous in cooling channel applications. However, due to the random nature of particle deposition and fusion, the local HT distribution becomes highly non-uniform and difficult to predict accurately [69].

The qualification of AM components using non-destructive testing (NDT) techniques requires a comprehensive set of measurements to verify material and manufacturing integrity. Surface roughness is one of the key indicators in this context. While traditionally defined as a quality requirement, SR now serves a dual role as both a functional specification and a measure of AM process efficiency, particularly in metal AM
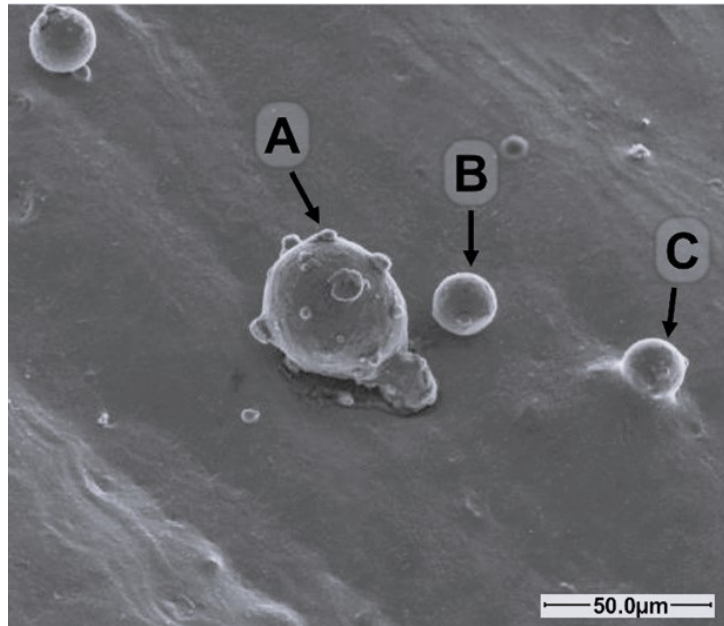
Figure 2.13: Microscope image of powder particles attached to the surface [69]

techniques like L-PBF [77].

The actual geometry of additively manufactured surfaces is so complex that no finite set of parameters can fully capture its characteristics [34]. The `ASME B46.1` [78] and `ISO 21920-2:2021` [97] standards provide widely accepted frameworks for defining surface texture in terms of roughness, waviness, and lay. As more parameters are introduced, the surface description becomes increasingly accurate, which has motivated the development of new metrics for SR evaluation. Surface roughness parameters are generally classified into three main categories based on their analytical focus: *amplitude parameters*, *spacing parameters*, and *hybrid parameters* [34].

2.3 Topological Parameters of Roughness

At the microscopic level, no surface is perfectly smooth; all exhibit geometrical irregularities, either random or uniform, comprising peaks and valleys that arise from the manufacturing process. The frequency of these irregularities defines the type of surface texture: *roughness* for high-frequency features, *waviness* for medium-frequency features, and *surface form* for low-frequency geometry changes, which indicate the overall shape of the object surface [88].

Due to the wide variation in surface types, shapes, and morphologies, the first step in characterizing roughness is to adopt clearly defined and measurable surface parameters.

Comprehensive discussions of roughness parameters and their effects on turbulent flow are provided in [34, 86, 117]. This section presents a concise overview of the key
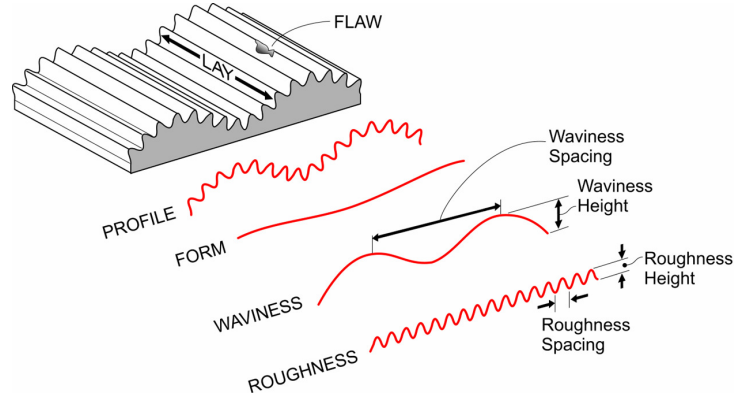
Figure 2.14: Difference between roughness, waviness and form [116]

topological parameters, also referred to as surface properties or roughness statistics. Commonly used parameters are summarized in Table 2.1.

To identify the most influential parameters affecting heat transfer, this thesis adopts a detailed classification of roughness parameters. Using only a limited set of descriptors may result in misinterpretations; surfaces with similar values for select parameters may exhibit fundamentally different thermo-fluid dynamic behaviors.
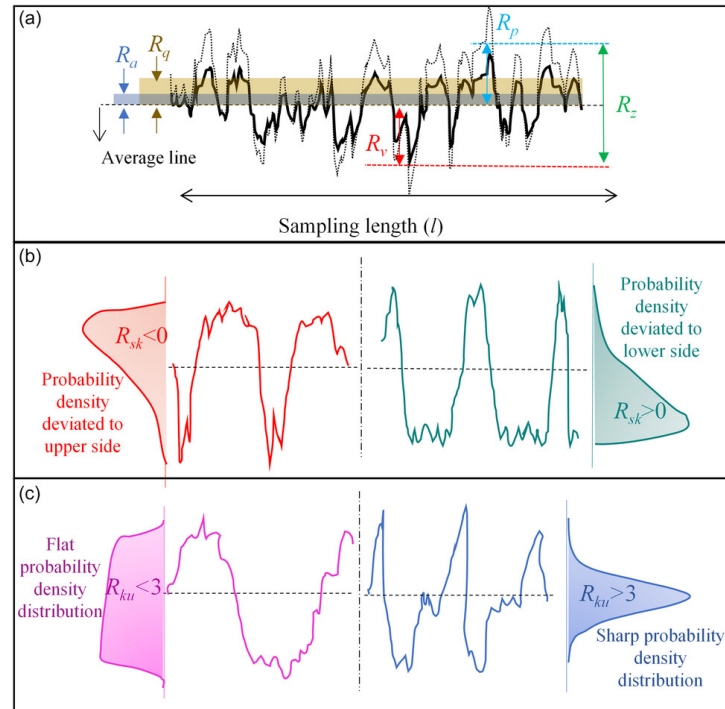
Figure 2.15: Schematic of the profile texture parameters [113]: (a) R_a, R_q, R_p, R_v, R_z, (b) R_{sk} and the height probability distribution, (c) R_{ku} and the height probability distribution.

To ensure a robust and reliable surface description, roughness parameters are categorized into three groups: *roughness height parameters*, *roughness spatial (density) parameters*, and *roughness spectral parameters* [117].

2.3.1 Roughness Height Parameters

Roughness parameters can be computed either along a profile line of length l (Fig. 2.15) or over a sampling area A. The profile-based parameters are denoted as R parameters, while area-based parameters are referred to as S parameters. Although R parameters are more widely adopted, S parameters provide a more representative and statistically robust description of surface features.

Amplitude parameters (R or S) are derived from height maps and quantify surface texture based on vertical deviations from a reference mean plane. Let $h(x, y)$ represent the surface elevation relative to a reference level $z = 0$. The height map can be decomposed into its mean and fluctuating components: $h(x, y) = \bar{h} + h'(x, y)$, where $\bar{h}$ is the mean height, and $h'(x, y)$ is the local deviation from the mean. The domain dimensions are l_x and l_y in the x and y directions, respectively.

2.3.1.1 Arithmetic Mean Roughness

The *arithmetic mean roughness S_a*, also known as the centre line average (CLA), is the most widely used parameter for general surface quality control. It quantifies the average of the absolute values of the surface height deviations from the mean plane across a given area:

$$S_a = \frac{1}{l_x l_y} \int_0^{l_x} \int_0^{l_y} \left| h'(x, y) \right| dx \, dy$$

2.3.1.2 Root Mean Square Roughness

The *root mean square roughness S_q* (RMS roughness) represents the standard deviation of the surface height distribution. It provides a statistical measure of surface irregularities and is more sensitive to large deviations than S_a. The RMS mean line is the line that divides the profile so that the sum of the squares of the deviations of the profile height from it is equal to zero.

$$S_q = \sqrt{\frac{1}{l_x l_y} \int_0^{l_x} \int_0^{l_y} (h'(x, y))^2 \, dx \, dy}$$

2.3.1.3 Five-Point Height

The *five-point height S_z* is defined based on either the ISO or DIN standard. In this work, the ISO definition is adopted. It defines S_z as the mean vertical distance between the average of the five highest peaks and the five lowest valleys within the sampling

area. This metric is particularly sensitive to occasional high or low features, unlike S_a:

$$S_z = \frac{1}{N} \sum_{i=1}^{N} S_{t_i} = \frac{1}{N} \sum_{i=1}^{N} \left(S_{p_i} + S_{v_i} \right)$$

where $N = 5$ under ISO conventions, or $N = 10$ in the DIN standard.

2.3.1.4 Maximum Profile Peak Height

The *maximum profile peak height* S_p is the largest deviation above the mean surface:

$$S_p = \max \left(h'(x, y) \right)$$

2.3.1.5 Maximum Profile Valley Depth

The *maximum profile valley depth* S_v is the greatest deviation below the mean surface level:

$$S_v = \left| \min \left(h'(x, y) \right) \right|$$

2.3.2 Roughness Spatial (Density) Parameters

Beyond primary amplitude-based roughness metrics, additional topographical descriptors are necessary to capture secondary surface characteristics that influence flow behavior. These include the shape of the height distribution, the spatial arrangement of roughness elements (e.g. clustering, anisotropy, and periodicity) and the orientation of the surface relative to the main flow direction.

The spatial organization of roughness can be quantified using the frontal solidity parameter (λ_f), the effective slope (ES), and the roughness density (Λ). These parameters characterize the portion of the surface exposed to pressure (form) drag and they are, thus, frequently interpreted as proxies for roughness element density.

2.3.2.1 Effective Slope

The *effective slope ES* quantifies the mean absolute gradient of the surface in the streamwise or spanwise direction. While both directions may be considered, the streamwise gradient is of particular relevance in wall-bounded turbulent flows.

Low values of ES typically indicate widely spaced or gently undulating surfaces (i.e., long-wavelength roughness), while high ES corresponds to densely packed or steeply varying features. These behaviors correspond respectively to **k-type roughness** and **d-type roughness** [88].

$$ES_x = \frac{1}{l_x l_y} \int_0^{l_x} \int_0^{l_y} \left| \frac{\partial h'(x, y)}{\partial x} \right| dx\, dy$$

$$ES_y = \frac{1}{l_x l_y} \int_0^{l_x} \int_0^{l_y} \left| \frac{\partial h'(x, y)}{\partial y} \right| dx\, dy$$

2.3.2.2 Frontal Solidity

The *frontal solidity* λ_f is defined as the ratio of the projected frontal area of the roughness elements, A_f, to the total plan area, A_t. This parameter reflects the area available for pressure drag and can serve as a surrogate for surface roughness density. For $\lambda_f \to 0$, such as in the case of isolated or sparse features, the surface behaves similarly to a hydraulically smooth wall. At the other extreme, in highly dense configurations, elements shield one another and drag is again diminished. Maximum drag and heat transfer typically occur in the intermediate regime, where $0.1 \lesssim \lambda_f \lesssim 0.3$ [86, 117].

The sparse regime is generally defined by $\lambda_f \leq 0.15$ ($ES \leq 0.35$), while values above this threshold indicate a dense regime. However, recent studies show that this classification is sensitive to additional parameters such as skewness [59, 72].

$$\lambda_f = \frac{A_f}{A_t}$$

Despite its usefulness, λ_f alone cannot distinguish between different roughness configurations. For example, the two surfaces depicted in Fig. 2.16(b,c) have equal λ_f and roughness height, but differ significantly in element aspect ratio and spatial packing. To capture such differences, the plan solidity λ_p (see Section 2.3.3.3) is required.
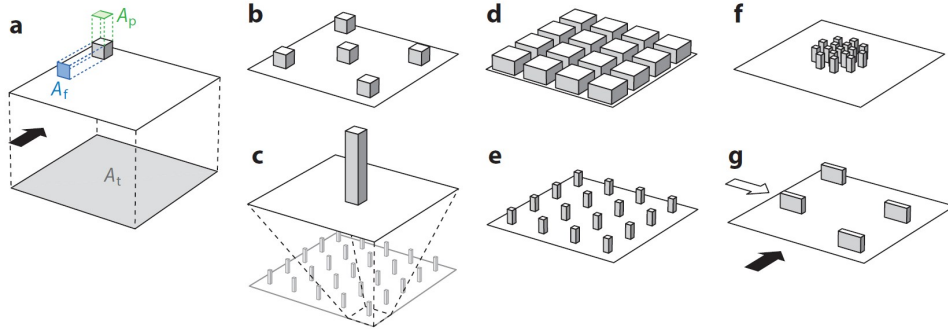
Figure 2.16: Surface sketches to illustrate frontal solidity $\left(\lambda_f\right)$ and plan solidity $\left(\lambda_p\right)$, as well as clustering and directionality. Open and filled arrows in panel *g* indicate different possible flow orientations [86].

2.3.2.3 Roughness Density

The *roughness density* parameter Λ has also been proposed as a spatial descriptor of surface roughness. It is defined in terms of the local surface angle $\alpha_h = \arctan\left(\frac{\partial h'(x,y)}{\partial x}\right)$ and relates the frontal and windward wetted areas:

$$\Lambda = \frac{1}{\lambda_f}\left(\frac{A_f}{A_w}\right)$$

where A_w denotes the total wetted surface area exposed to the flow in the windward direction.

2.3.3 Roughness Spectral Parameters

2.3.3.1 Skewness

Skewness characterizes the asymmetry of the surface height distribution. It quantifies the degree to which the distribution deviates from a Gaussian (normal) shape, for which the skewness is zero. A surface exhibiting large valleys with fewer high peaks, as might occur due to deposition phenomena in laser sintering, results in a positive skewness ($S_{sk} > 0$). Conversely, surfaces featuring dominant peaks with occasional deep valleys, such as those caused by pitting or corrosion, tend to exhibit negative skewness ($S_{sk} < 0$). This concept is illustrated in Fig. 2.17.

$$S_{sk} = \frac{1}{S_q^3} \int_0^{l_x} \int_0^{l_y} (h'(x,y))^3 \, dx \, dy$$
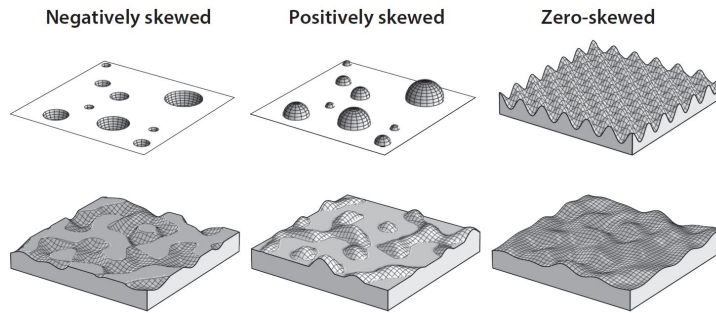
Figure 2.17: Irregular surfaces with different skewness levels, adapted from [86]

2.3.3.2 Kurtosis

Kurtosis is a measure of the "peakedness" or sharpness of the surface height distribution. A value of $S_{ku} = 3$ indicates a Gaussian distribution. Surfaces with $S_{ku} < 3$ exhibit a platykurtic distribution, where the profile is relatively flat with fewer extreme deviations (low peaks and shallow valleys). Conversely, surfaces with $S_{ku} > 3$ are leptokurtic, meaning they have many sharp peaks and deep valleys. These differences in topographical structure are depicted in Fig 2.15.

$$S_{ku} = \frac{1}{S_q^4} \int_0^{l_x} \int_0^{l_y} (h'(x,y))^4 \, dx \, dy$$

2.3.3.3 Plan Solidity

The *plan solidity* λ_p is defined as the ratio between the projected plan area of the roughness elements, A_p, and the total reference area, A_t:

$$\lambda_p = \frac{A_p}{A_t}$$

A high plan solidity $\left(\lambda_p \rightarrow 1\right)$ indicates a densely packed configuration of roughness elements and is generally associated with negative skewness. In contrast, a low plan solidity $\left(\lambda_p \rightarrow 0\right)$ corresponds to sparsely distributed elements, typically correlated with positive skewness.

The ratio λ_f / λ_p provides insight into the geometric aspect ratio of roughness elements. Cube-like elements have $\lambda_f / \lambda_p = 1$, while $\lambda_f / \lambda_p < 1$ implies squat or flat elements, and $\lambda_f / \lambda_p > 1$ indicates tall, slender structures. However, this interpretation may be distorted in cases of clustering or non-uniform distribution.

Combining spectral and spatial parameters provides a more comprehensive assessment of roughness characteristics. Recent studies demonstrate that jointly considering plan solidity λ_p and frontal solidity λ_f leads to an improvement in drag prediction [117].

2.4 Fundamentals of Heat Transfer

This section presents the principles underlying the fundamental mechanisms of heat exchange. In [42], the authors provide detailed explanations in response to core questions that often arise when studying heat transfer:

What is heat transfer? How is heat transferred? Why is it important?

The objective of this thesis is not to pursue such an extensive discourse, but rather to cover the foundational concepts of heat transfer, offering a general framework to support the understanding of this research project.

2.4.1 Definition and Governing Laws

The investigation of heat transfer involves two primary objectives: (1) to evaluate the rate of energy transfer as heat across a system's boundary in both steady and unsteady conditions; and (2) to determine the temperature distribution within the system over time and space. This investigation provides essential insight into temperature gradients and how they evolve at various locations and times.

A concise definition of heat transfer is provided by Incropera et al. [42]:

Heat transfer (or heat) is the thermal energy in transit due to a spatial temperature difference.

Parameter	Definition	Description
Roughness Height Parameters		
S_a	$\dfrac{1}{l_x l_y} \displaystyle\int_0^{l_x} \int_0^{l_y} \left| h'(x,y) \right| \, dx \, dy$	Arithmetic mean height deviation from the mean surface plane
S_q	$\sqrt{\dfrac{1}{l_x l_y} \displaystyle\int_0^{l_x} \int_0^{l_y} \left(h'(x,y) \right)^2 \, dx \, dy}$	Root-mean-square roughness
S_v	$\left| \min\left(h'(x,y) \right) \right|$	Maximum valley depth below the mean line within the sampling area
S_p	$\max\left(h'(x,y) \right)$	Maximum peak height above the mean line within the sampling area
S_z	$\dfrac{1}{N} \displaystyle\sum_{i=1}^{N} S_{t_i} = \dfrac{1}{N} \sum_{i=5}^{N} \left(S_{p_i} + S_{v_i} \right)$	Average of five highest peaks and five deepest valleys (ISO standard)
Roughness Spatial Parameters		
ES	$\dfrac{1}{l_x l_y} \displaystyle\int_0^{l_x} \int_0^{l_y} \left| \dfrac{\partial h'}{\partial x} \right| \, dx \, dy$	Effective slope
λ_f	$\dfrac{A_f}{A_t}$	Frontal solidity
Λ	$\dfrac{1}{\lambda_f} \left(\dfrac{A_f}{A_w} \right)$	Roughness density
Roughness Spectral Parameters		
S_{sk}	$\dfrac{1}{S_q^3} \displaystyle\int_0^{l_x} \int_0^{l_y} \left(h'(x,y) \right)^3 \, dx \, dy$	Skewness
S_{ku}	$\dfrac{1}{S_q^4} \displaystyle\int_0^{l_x} \int_0^{l_y} \left(h'(x,y) \right)^4 \, dx \, dy$	Kurtosis
λ_p	$\dfrac{A_p}{A_t}$	Plan solidity

Table 2.1: Summary of surface roughness parameters

This definition implies that whenever a temperature difference exists within a medium or between different media, heat transfer will occur. Specifically, thermal energy always flows from the region of higher temperature to that of lower temperature.

In the study of heat transfer, the goal is to describe the mechanisms by which this energy exchange occurs between different equilibrium states. Three primary heat transfer mechanisms, or modes, are recognized: **conduction**, **convection**, and **thermal radiation**, as illustrated in Fig. 2.18.
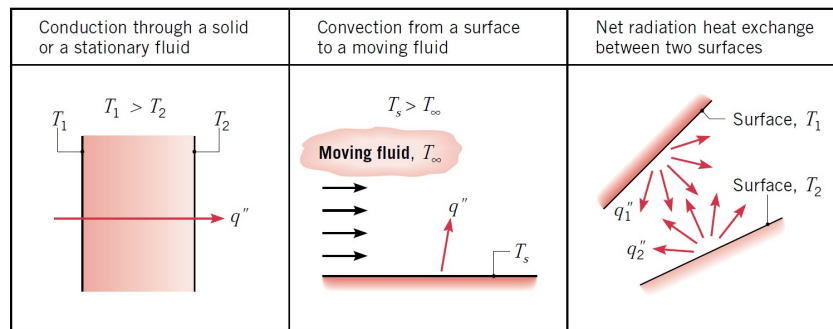
Figure 2.18: Conduction, convection, and radiation heat transfer modes [42]

When a temperature gradient exists within a stationary medium (solid or fluid), the resulting energy transfer is referred to as *conduction*. In contrast, *convection* describes the energy exchange between a surface and an adjacent moving fluid at a different temperature. A third mode, known as *thermal radiation*, involves the emission of electromagnetic energy from all surfaces at a temperature above absolute zero. Thus, even in the absence of a material medium, heat can be transferred by radiation between two surfaces at different temperatures.

The fundamental laws that govern heat transfer and their application are summarized below [43]:

1. **First Law of Thermodynamics**: This law expresses the principle of energy conservation, relating heat flow to the change in a system's internal energy. For a closed system:

   "Net heat flow across the system boundary + internal heat generation = change in internal energy"

   This principle also holds for open systems with appropriate modifications.

2. **Second Law of Thermodynamics**: This law dictates the direction of heat flow, stating that thermal energy will always flow in the direction of decreasing temperature, i.e., along the negative temperature gradient.

3. **Newton's Laws of Motion**: These are used to determine fluid flow behavior, which in turn affects convective heat transfer.

4. **Law of Conservation of Mass**: Applied in analyzing fluid flow properties, this law is essential for formulating the continuity equation in convective heat transfer studies.

5. **Rate Equations**: Each heat transfer mode has an associated rate equation; for example, Fourier's law for conduction, Newton's law of cooling for convection, and the Stefan-Boltzmann law for radiation.

2.4.2 Conduction

The *conduction* mechanism describes energy transfer due to the microscopic motion of electrons or molecules, such as lattice vibrations in solids or molecular collisions in fluids. A key characteristic of conduction is the absence of macroscopic mass motion, in fact energy is transferred without the net movement of matter.

The physical mechanism of conduction can be intuitively explained by considering a gas subject to a temperature gradient, as illustrated in Fig. 2.19. Let us assume that no bulk fluid motion exists, and that the gas is confined between two surfaces at different temperatures. In this context, temperature corresponds to the average molecular energy, including translational, rotational, and vibrational contributions.

(a)   (b)
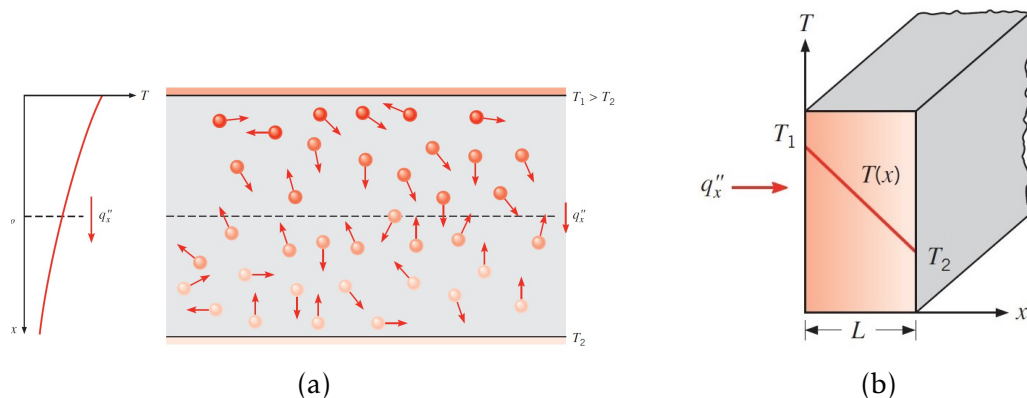
Figure 2.19: Conduction processes [42]: (a) Association of conduction heat transfer with energy diffusion due to molecular activity; (b) One-dimensional heat transfer by conduction

At higher temperatures, molecules possess greater kinetic energy. When these energetic molecules collide with neighboring, less energetic ones, energy is transferred from hot to cold regions. Even in the absence of direct collisions, random molecular motion across an imaginary plane results in a net energy transfer. Molecules from the high-temperature region will, on average, carry more energy than those from the colder side, resulting in a unidirectional energy flux. This phenomenon is referred to as *diffusion of energy*.

To quantify this process, the appropriate rate law is *Fourier's law of heat conduction*,

which relates the local heat flux to the temperature gradient. For a one-dimensional conduction scenario, such as the plane wall shown in Fig. 2.19(b), the heat flux $\dot{q}_x$ is given by:

$$\dot{q}_x = -k_{tc}\frac{dT}{dx} \tag{2.2}$$

The negative sign indicates that heat flows in the direction of decreasing temperature, in agreement with the second law of thermodynamics.

In three-dimensional systems, the generalized form of Fourier's law is:

$$\dot{q} = -k_{tc}\nabla T = -k_{tc}\left(\vec{i}\frac{\partial T}{\partial x} + \vec{j}\frac{\partial T}{\partial y} + \vec{k}\frac{\partial T}{\partial z}\right)$$

Heat conduction occurs in all directions where a temperature gradient exists. Here, the temperature is a spatial function, $T(x,y,z)$, and k_{tc} (or simply k) is the *thermal conductivity* of the material, expressed in $W/(m \cdot K)$.

Thermal conductivity is a transport property that varies with material type and may also depend on temperature and pressure, especially in gases. While it is often assumed to be constant and isotropic in analytical models, this assumption does not hold in all cases. In particular, objects fabricated via additive manufacturing frequently exhibit anisotropic thermal conductivity, with differing values along and across the build direction.

2.4.3 Convection

In the *convection* heat transfer mode, thermal energy is transferred between a surface and a moving fluid, depending on the temperature difference between the fluid bulk temperature, T_∞, and the wall surface temperature, T_w. Convection involves a dual mechanism: the transfer of energy via random molecular motion (diffusion), and the macroscopic transport of the fluid (advection). Within a fluid subjected to a temperature gradient, the collective, organized motion of molecules due to bulk fluid movement significantly influences the rate of heat transfer.

Convection is particularly relevant when studying the interaction between a fluid in motion and a solid surface at a different temperature. The temperature difference between the two gives rise to a *thermal boundary layer*, a region in which the temperature transitions from the wall value to that of the fluid bulk, as depicted in Fig. 2.28. The thickness of this layer can vary depending on the flow and thermal conditions and may be smaller, greater, or comparable to the momentum boundary layer.

Within the thermal boundary layer, heat is transferred by both *molecular diffusion* and *bulk advection*. In the near-wall region, where the fluid velocity is low, diffusion dominates. At the very surface ($y = 0$), the no-slip condition implies zero fluid velocity, and consequently, heat is transferred exclusively by conduction (i.e., diffusion).

The classification of convection depends on the mechanism driving the fluid motion:
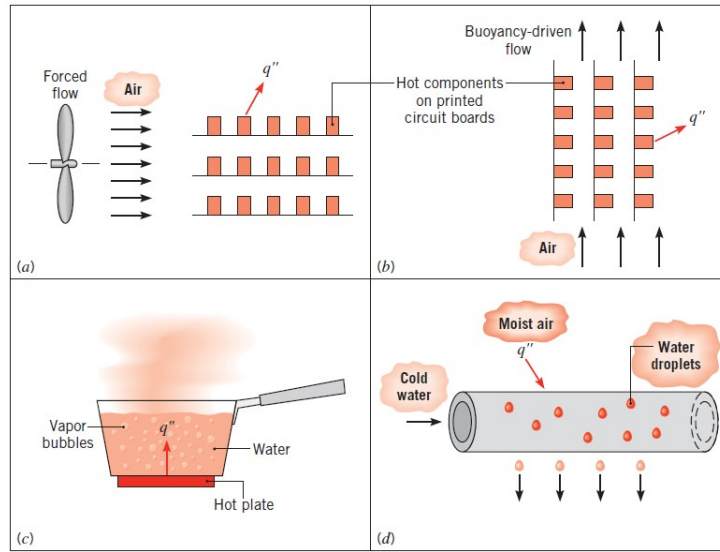
Figure 2.20: Convection heat transfer processes [42]: (a) Forced convection, (b) Natural convection, (c) Boiling, (d) Condensation

- *Forced convection* occurs when the fluid flow is driven by external means, such as pumps, fans, or ambient wind.

- *Free* or *natural convection* occurs when the fluid motion arises due to buoyancy forces caused by density differences resulting from temperature gradients.

Natural convection typically occurs in low-speed or stagnant flows where temperature differences alone induce fluid motion.

To quantify the convective heat exchange, a proportional constant called the *heat transfer coefficient h* (in $W/m^2 \cdot K$) is introduced to relate the heat flux to the temperature difference between the wall and the fluid. This is expressed in the form of *Newton's law of cooling* [30]:

$$\dot{q}_{\text{conv}} = h\left(T_w - T_\infty\right) \tag{2.3}$$

Here, $\dot{q}_{\text{conv}}$ is the convective heat flux. A positive value indicates heat transfer from the surface to the fluid ($T_w > T_\infty$), while a negative value indicates heat flow from the fluid to the surface ($T_w < T_\infty$).

2.4.4 Radiation

Thermal radiation is energy emitted by matter at any temperature above absolute zero. Radiative heat transfer is a phenomenon related to electromagnetic fields, arising from the motion of charged particles within matter. Analogous to an antenna that generates electromagnetic waves via oscillating charges, atoms and molecules in a material emit radiation due to the thermal motion of electrons and protons. The wavelength distribution of the emitted energy depends on the internal energy of the body, i.e., its

temperature, and this emission corresponds to a reduction of the body's internal energy. Thermal radiation propagates as electromagnetic waves or photons and, unlike conduction and convection, requires no material medium to transfer energy, enabling energy exchange even through a vacuum.
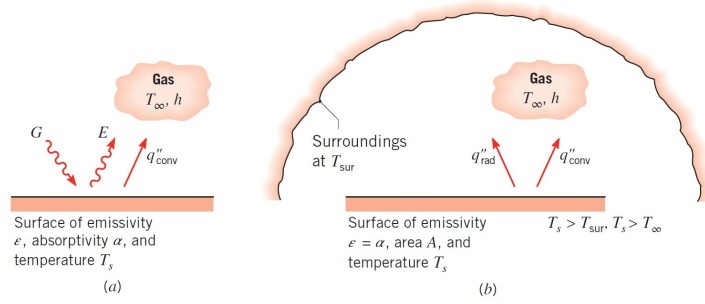
Figure 2.21: Radiation exchange [42]: (a) at a surface, and (b) between a surface and large surroundings

The four fundamental radiative quantities are:

- *Global emission E*: the total emitted power from a surface across all wavelengths and directions,

$$E = \frac{dq}{dA}$$

  where dq is the emitted heat energy from area dA.

- *Monochromatic emission e_λ*: the emitted power from a surface within a specific wavelength range, integrated over all directions,

$$e_\lambda = \frac{dq}{dA\,d\lambda}$$

- *Global irradiation intensity i_δ*: the power incident on a surface per unit area, per solid angle $d\omega$, integrated over all wavelengths, at an angle θ,

$$i_\delta = \frac{dq}{dA\,d\omega\cos\theta}$$

- *Monochromatic irradiation intensity $i_{\delta,\lambda}$*: the power incident per unit area, per solid angle, and per wavelength,

$$i_{\delta,\lambda} = \frac{dq}{dA\,d\lambda\,d\omega\cos\theta}$$

Considering all wavelengths and directions, the radiative heat flux dq incident on a surface can be partitioned into absorbed, reflected, and transmitted components, denoted as dq_a, dq_r, and dq_τ, respectively. The corresponding surface properties are the

absorptivity α_a, reflectivity ρ, and transmissivity τ:

$$\alpha_a = \frac{dq_a}{dq} \quad ; \quad \rho = \frac{dq_r}{dq} \quad ; \quad \tau = \frac{dq_\tau}{dq}$$

These coefficients satisfy the relation:

$$\alpha_a + \rho + \tau = 1 \tag{2.4}$$

The net thermal radiation heat flux $\dot{q}_{\text{rad}}$ is determined by the balance of emitted, absorbed, and transmitted radiation.

The *emissive power E* of a surface (rate of energy emitted per unit area, W/m^2) is governed by the *Stefan-Boltzmann law* for an idealized *blackbody* surface:

$$E_b = \sigma_{SB} T_s^4$$

where T_s is the absolute temperature (K) of the surface and $\sigma_{SB} = 5.67 \times 10^{-8}\ W/m^2 \cdot K^4$ is the Stefan-Boltzmann constant. A blackbody emits the maximum possible radiation at a given temperature.

Real surfaces emit less radiation than a blackbody and are characterized by an *emissivity ε* ($0 \leq \varepsilon \leq 1$), such that:

$$E = \varepsilon \sigma_{SB} T_s^4$$

Emissivity depends strongly on surface material, texture, and finish.

In typical scenarios, radiative heat exchange occurs between a small surface at temperature T_s and a much larger, surrounding surface at temperature T_{surf} (see Fig. 2.21b). For a *gray* surface, where emissivity equals absorptivity ($\varepsilon = \alpha_a$), the net radiative heat flux per unit area is expressed as:

$$\dot{q}_{\text{rad}} = \varepsilon \sigma_{SB} \left(T_s^4 - T_{\text{surf}}^4 \right)$$

Here, the net radiative heat transfer is proportional to the difference of the fourth powers of the absolute temperatures of the surfaces involved.

2.4.4.1 The Blackbody Hypothesis

A *blackbody* (BB) is an idealized surface that absorbs all incident radiation, regardless of wavelength or direction. Accordingly, its global absorptivity is defined as:

$$\alpha_a = 1$$

From the energy balance expressed in Eq. (2.4), it follows that for a blackbody:

$$\rho = 0, \qquad \tau = 0$$

This implies that no radiation is reflected or transmitted; all incident energy is absorbed. According to Kirchhoff's law of thermal radiation, for a body in thermal equilibrium, the emissivity equals the absorptivity:

$$\varepsilon = \alpha_a$$

Hence, a blackbody also emits radiation at the maximum possible rate for a given temperature, i.e., it has $\varepsilon = 1$.

An analytical expression for the spectral distribution of blackbody radiation is provided by Planck's law, which describes the monochromatic irradiation intensity of a blackbody:

$$i_{\delta,\lambda} = \frac{b_1}{n^2 \lambda^5 \left(e^{\frac{b_2}{\lambda T}} - 1 \right)}$$

where T is the absolute temperature $[K]$, n is the refractive index of the surrounding medium (e.g., $n = 1$ in vacuum), $b_1 = 1.19096 \times 10^{-16}$ $W/m^2 \cdot sr$, $b_2 = 1.43879 \times 10^{-2}$ $m \cdot K$. This expression shows that the monochromatic irradiation depends solely on wavelength for a given T and n. The resulting distribution exhibits a characteristic shape, as illustrated in Fig. 2.22.
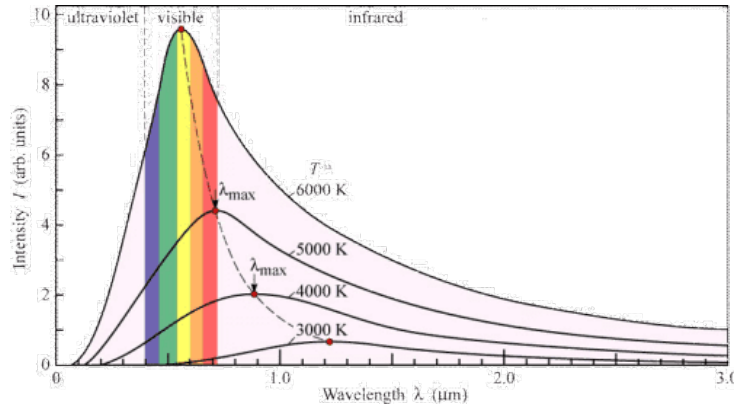
Figure 2.22: Monochromatic irradiation intensity of a blackbody according to Planck's law

As the temperature increases, the intensity of radiation increases, and the peak shifts towards shorter wavelengths. For a blackbody, the monochromatic emission e_λ is related to the irradiation intensity by:

$$e_\lambda = \pi i_{\delta,\lambda}$$

indicating that the surface emits uniformly over all directions. The peak of monochromatic emission occurs at a specific wavelength λ^*, which is inversely proportional to the temperature, as described by Wien's displacement law:

$$\lambda^* = \frac{b_3}{nT}$$

where $b_3 = 2897.8 \ \mu m \cdot K$ is Wien's constant. This allows the determination of the wavelength at which emission is maximum for a given temperature.

The total emissive power of a blackbody over all wavelengths is obtained by integrating the spectral emissive power:

$$E = \int_0^\infty e_\lambda \, d\lambda = n^2 \sigma_{SB} T^4$$

This is the Stefan-Boltzmann law for a blackbody, indicating that the total emitted radiation increases with the fourth power of the absolute temperature. Every blackbody is thus characterized by an emission that depends solely on its temperature and the medium's refractive index.

2.4.5 Boundary and Initial Conditions

To determine the temperature distribution within a medium, it is necessary to solve the appropriate form of the heat conduction equation. However, the solution depends not only on the equation itself but also on the physical conditions prescribed at the *boundaries* of the domain and, in the case of transient problems, on the *initial conditions* at the start of the process.

There are three classical types of boundary conditions which are commonly encountered in heat transfer problems and they are schematically illustrated in Fig. 2.23:

- *Dirichlet condition* (First kind): A fixed surface temperature T_s is specified.

- *Neumann condition* (Second kind): A constant or prescribed heat flux $\dot{q}$ is imposed at the surface. This condition applies to cases with insulated boundaries ($\dot{q} = 0$) or controlled thermal fluxes.

- *Robin condition* (Third kind): This condition models convective heat transfer at the surface and results from applying the energy balance. It combines both conduction and convection

2.4.6 Nusselt Number

In convective heat transfer analysis, a common approach involves non-dimensionalizing the governing equations and combining variables into dimensionless groups. This technique simplifies the physical system and reduces the number of independent parameters [30, 42, 43, 58] (see Appendix A). One such dimensionless quantity, used to characterize convection, is the **Nusselt number**.

The Nusselt number is defined as the ratio of convective to conductive heat transfer across a boundary:

$$Nu = \frac{hL_c}{k}$$

1. Constant surface temperature

$$T(0, t) = T_s$$

2. Constant surface heat flux
    (a) Finite heat flux

$$-k\frac{\partial T}{\partial x}\Big|_{x=0} = q_s''$$

    (b) Adiabatic or insulated surface

$$\frac{\partial T}{\partial x}\Big|_{x=0} = 0$$

3. Convection surface condition

$$-k\frac{\partial T}{\partial x}\Big|_{x=0} = h[T_\infty - T(0, t)]$$
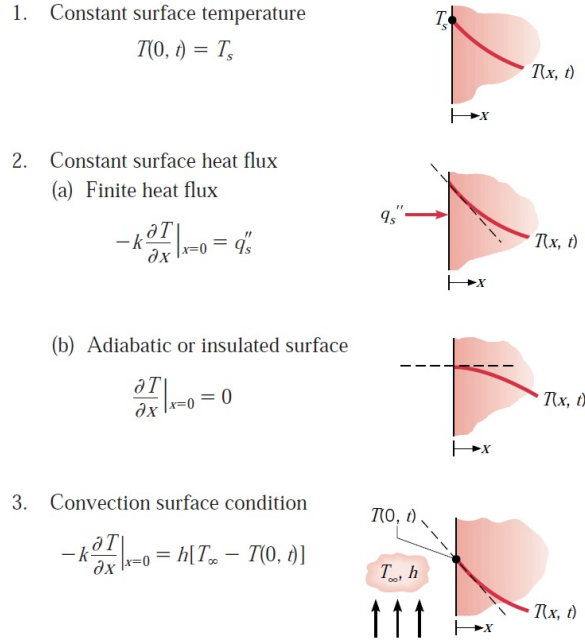
Figure 2.23: Common boundary conditions for the one-dimensional heat diffusion equation at $x = 0$ [42]

where h is the convective heat transfer coefficient, L_c is the characteristic length $[m]$ and k is the thermal conductivity of the fluid.

Alternatively, in the context of boundary layer analysis, the Nusselt number can be related to the dimensionless temperature gradient at the surface:

$$Nu = \frac{\partial T^*}{\partial y^*}\Big|_{y^*=0}$$

with the following dimensionless variables:

$$T^* = \frac{T - T_w}{T_\infty - T_w} \qquad ; \qquad y^* = \frac{y}{L}$$

Here, T_w is the wall temperature, and T_∞ is the free-stream fluid temperature.

In thermal analysis, the Nusselt number plays a role analogous to that of the friction coefficient in momentum transfer, serving as a key indicator of thermal boundary layer behavior.

2.5 Infrared Thermography

In many heat transfer applications, the surface temperature distribution is of critical importance for assessing thermal behavior. This is especially true in convective HT experiments, such as those conducted in this work, where direct surface temperature

measurements are often problematic due to flow enclosure or the intrusive nature of contact sensors. *Infrared Thermography* (IR), also known as thermal imaging, is a suitable technique in these contexts, as it enables non-contact, two-dimensional temperature measurements. This is achieved through an IR scanning radiometer within an IR camera, which detects the electromagnetic (EM) radiation emitted by the object in the infrared spectrum. The detected EM energy is then converted into an electronic video signal, which can be calibrated and correlated to temperature values [31].

To understand this process, a brief overview of EM radiation and its relationship with thermal emission is necessary.

As discussed in the previous section, any object above absolute zero emits thermal radiation. The maximum radiative emission from a body at a given temperature is defined by that of a blackbody (BB), often referred to as a perfect emitter [50].

The electromagnetic spectrum spans a wide range of wavelengths, of which only a small portion consists of visible light. The infrared (IR) spectrum ranges approximately from $0.78\,\mu m$ to $1\,mm$ and is typically divided into three sub-regions relevant to IR imaging: short-wave IR (SWIR): $0.9 - 1.7\,\mu m$, mid-wave IR (MWIR): $3 - 5\,\mu m$, long-wave IR (LWIR): $7 - 14\,\mu m$. These regions are illustrated in Fig. 2.24 [50].
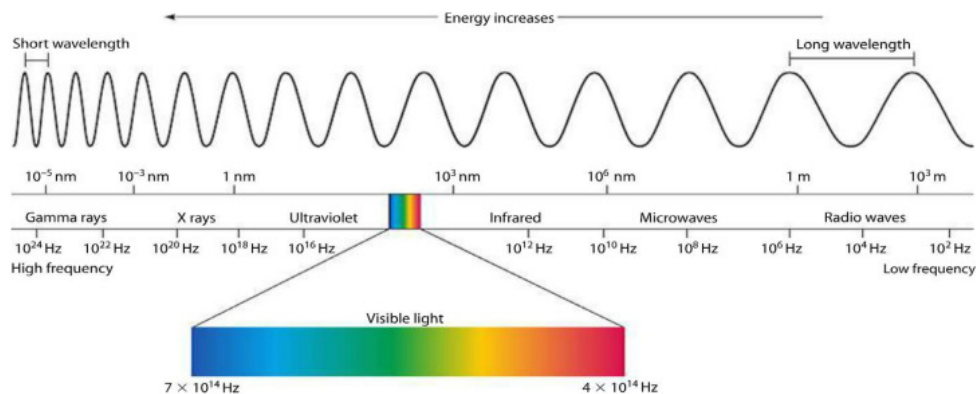
Figure 2.24: Components of the Electromagnetic Spectrum

However, IR cameras do not capture radiation across the full spectrum. Instead, they are limited to specific spectral ranges determined by the detector and optical components. Consequently, radiometric IR measurements are not based on the full Stefan-Boltzmann law but rather on Planck's law, integrated numerically over the relevant wavelength interval [50], since no analytical solution exists for arbitrary spectral bounds.

The IR detector is the core component of the thermographic system. It acts as a transducer that absorbs the thermal radiation emitted by the target surface and converts it into an electrical signal, such as voltage or current. This conversion is possible due to the material properties of the detector, which enable photon-induced electron excitation [31]. Most modern IR cameras make use of detectors made from Indium Antimonide (InSb).

Accurate surface temperature measurements therefore require a reliable determination of the object's surface emissivity. Emissivity is one of the most critical factors influencing IR thermographic accuracy.

Another significant source of error arises from environmental contributions. As illustrated in Fig. 2.25, the IR detector may receive radiation not only from the object of interest but also from surrounding warm bodies, measurement equipment, or the atmosphere. Transmission losses, such as from windows placed between the object and the camera, can also degrade the measurement. In addition, radiation reflected from nearby surfaces may affect the total detected signal [50].
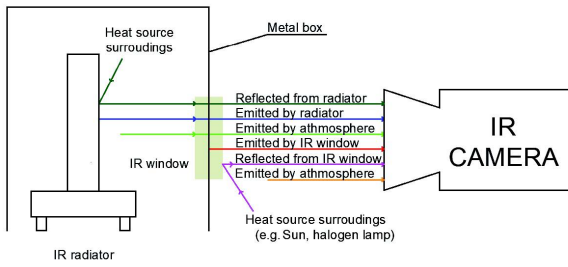
Figure 2.25: IR radiation contributions reaching the camera lens [87]
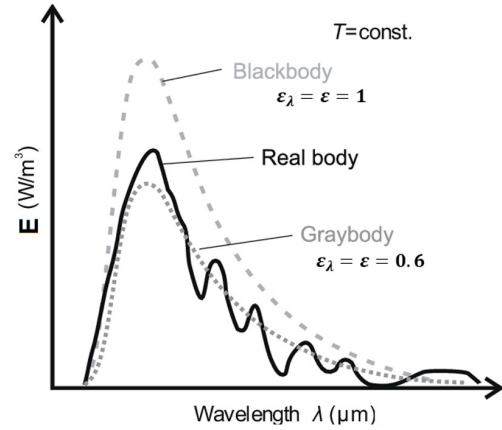
Figure 2.26: Comparison of blackbody and real surface emissions [96]

As outlined above, numerous factors affect IR thermography, and these can vary significantly depending on the specific application. The strategies adopted in this thesis to account for these influences are explained in Chapter 3.

2.6 Boundary Layer Theories

Local shear stress becomes relevant only in regions where velocity gradients are significant. These gradients are generally small in the bulk of the flow field, far from the solid boundary, where frictional effects are negligible unless the velocities are extremely high. However, adjacent to the surface, velocity gradients become steep, and viscous effects become prominent. This thin region of intense shear is known as the *fluid dynamic boundary layer* [37, 51].

Similarly, thermal energy exchange between the fluid and the wall occurs predominantly within a narrow region near the surface, named *thermal boundary layer*. Since both frictional and heat transfer phenomena are largely confined to these boundary layers, and given that the present study focuses on the influence of surface roughness on pressure losses and heat transfer, an in-depth understanding of boundary layer (BL) theory is essential.

In fluid dynamic or convective heat transfer analyses, determining the nature of the boundary layer (whether laminar, transitional, or turbulent) is of critical importance, as it significantly influences surface friction and convective heat transfer rates.
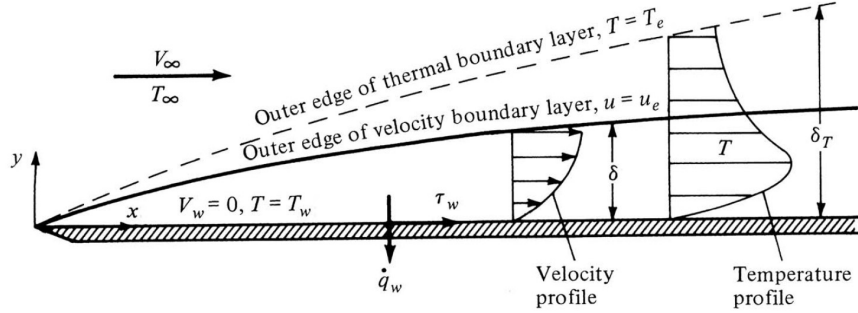
Figure 2.27: Boundary layer properties [51]

2.6.1 Laminar and Turbulent Flows

Fluid motion can generally be categorized as either *laminar* or *turbulent*. The development of the boundary layer over a flat plate under both conditions is illustrated in Fig. 2.27.

The velocity profiles in laminar and turbulent boundary layers, particularly in the streamwise (x) direction, exhibit distinct differences [42]. In turbulent flow, enhanced mixing in both the buffer and core turbulent regions leads to a more uniform velocity profile across a large part of the boundary layer. This results in a steeper velocity gradient near the wall, especially in the viscous sublayer, as clearly depicted in Fig. 2.28.
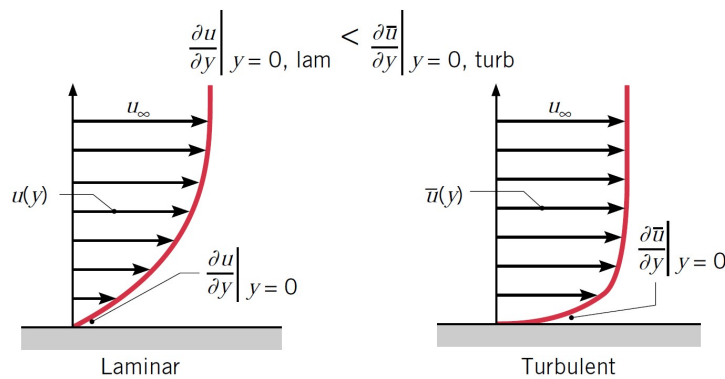
Figure 2.28: Comparison of laminar and turbulent velocity boundary layer profiles for the same free stream velocity [42]

The transition from laminar to turbulent flow depends on several factors. Through a series of pioneering experiments in the 1880s, Osborne Reynolds demonstrated that

the flow regime is primarily governed by the ratio of inertial to viscous forces in the fluid [3]. This ratio is expressed as the dimensionless *Reynolds number*, defined for external flows as:

$$Re = \frac{\text{inertial forces}}{\text{viscous forces}} = \frac{u_\infty L_c}{\nu} = \frac{u_\infty L_c \rho}{\mu}$$

where u_∞ is the free-stream velocity, L_c is the characteristic length based on the geometry, ν is the kinematic viscosity, ρ is the fluid density, and μ is the dynamic viscosity.

The Reynolds number at which the flow transitions from laminar to turbulent is referred to as the *critical Reynolds number*. This threshold varies depending on the object's shape and the prevailing flow conditions.

2.6.2 Fundamentals of Turbulent Flows

Most flows encountered in real-world engineering applications are turbulent. The term *turbulence* refers to a flow regime characterized by chaotic, three-dimensional, and time-dependent fluctuations. These irregular eddying motions are superimposed on the primary mean flow direction and provide an additional mechanism for the transport of momentum, energy, and scalar quantities such as temperature or species concentration.

2.6.2.1 Mean Motion and Fluctuations

A fundamental feature of turbulent flow is that any property X (e.g., a velocity component, pressure, or temperature) exhibits random and rapid temporal variations at any fixed spatial location. Rather than remaining steady, these quantities fluctuate with high frequency and irregular amplitude.

To analyze turbulent flows, it is common to decompose such quantities into two components: a time-averaged (or mean) part $\overline{X}$ and a fluctuating component X', as expressed by Reynolds decomposition. The time average is typically computed over a time interval that is much longer than the characteristic period of the fluctuations. If the mean component $\overline{X}$ does not vary with time, the flow is considered *statistically steady*.

The decomposition is formally written as:

$$u = \overline{u} + u'$$
$$v = \overline{v} + v' \qquad p = \overline{p} + p' \qquad \theta = \overline{\theta} + \theta'$$
$$w = \overline{w} + w'$$

Here, u, v, and w are the velocity components in the streamwise, transverse, and spanwise directions, respectively; p is pressure; and θ may represent temperature or another scalar quantity.

This decomposition forms the basis of the Reynolds-Averaged Navier-Stokes (RANS) equations, which are commonly used to model turbulent flows in both analytical and numerical approaches.

2.6.3 Momentum Boundary Layer

The description of boundary layer development is often illustrated using the flat plate case; however, the same physical principles apply to internal flows, where the fluid is confined within solid surfaces. For simplicity, the term "boundary layer" (BL) will be used here to refer to internal flows as well.

All real fluids possess viscosity, which generates shear stresses between adjacent fluid layers moving at different velocities. Near a solid surface, the no-slip condition enforces that the fluid velocity matches that of the wall, typically zero. As a result, there exists a region where the fluid velocity transitions from zero to the free stream velocity u_∞, known as the *momentum boundary layer* or *velocity boundary layer*. Its thickness, δ, is conventionally defined as the distance from the wall to the point where the velocity reaches 99% of u_∞ [51].

The velocity boundary layer arises due to viscous effects. At the wall, the velocity is zero (*no-slip condition*, $u_{\text{wall}} = 0$), and it increases with distance in the wall-normal (y) direction until reaching the free stream value. The structure and development of the BL are highly dependent on the flow velocity and geometry. At low speeds and gentle velocity gradients, the boundary layer remains laminar with parallel streamlines. As the velocity increases, the flow becomes susceptible to instabilities. Reverse flow and vortices may form near the wall, leading to a transition to turbulence. Figure 2.29 illustrates the development from laminar to turbulent boundary layers over a flat plate.
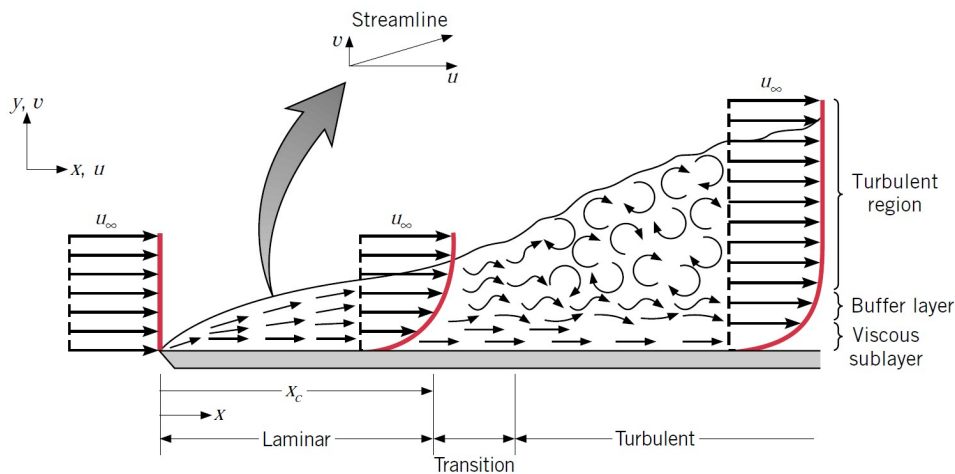
Figure 2.29: Velocity boundary layer development on a flat plate [42]

As the flow proceeds along the surface, the boundary layer thickness δ increases, re-

sulting in a decrease in the wall shear stress. Eventually, the laminar BL becomes unstable and transitions to a turbulent regime. This transition is influenced by multiple factors, including unsteady flow structures, ambient disturbances, and surface conditions. During the transition region, the flow may exhibit laminar, turbulent, or mixed behavior.

Parameters such as geometry, pressure gradients, surface temperature, and wall roughness affect the location of transition. For example, heating the wall lowers the critical Reynolds number for transition, while cooling tends to stabilize the laminar regime. Favorable pressure gradients delay transition, whereas adverse pressure gradients promote it. Surface roughness also plays a significant role by introducing disturbances and disrupting laminar flow, causing earlier transition [18].

The velocity variation $u(y)$ within the boundary layer, from the wall to δ, defines the velocity profile. Since both u and δ depend on the streamwise coordinate x, the wall shear stress also varies with x.

Viscous forces within the BL are expressed as shear stresses τ, and for Newtonian fluids, the shear stress is proportional to the velocity gradient [30]:

$$\tau = \mu \frac{\partial u}{\partial y} \qquad \Rightarrow \qquad \tau_w = \mu \left. \frac{\partial u}{\partial y} \right|_{y=0}$$

Here, τ_w denotes the wall shear stress. Since the boundary layer develops downstream, τ_w decreases with increasing x.

A key parameter in boundary layer analysis is the *friction velocity u_τ*, defined as:

$$u_\tau = \sqrt{\frac{\tau_w}{\rho}}$$

This quantity is used to normalize the velocity and distance from the wall:

$$u^+ = \frac{u}{u_\tau} \qquad \text{and} \qquad y^+ = \frac{y u_\tau}{\nu}$$

In fully turbulent flows, the BL exhibits a wide range of eddies of different sizes, and two distinct regions can be identified: the *inner region* and the *outer region*. The inner region typically encompasses about 10-20% of δ and is further subdivided into:

- *Viscous sublayer* ($0 \leq y^+ \leq 5$): A thin layer adjacent to the wall dominated by viscous shear stresses.

- *Buffer layer* ($5 < y^+ \leq 30$): A transitional zone where both viscous and turbulent shear stresses are significant.

- *Logarithmic layer* ($30 \leq y^+ \leq 500 - 1000$): A region where turbulence dominates and the velocity follows a logarithmic profile.

The outer region constitutes the remainder of the BL (~80-90% of δ) and spans up to the boundary layer edge. Figure 2.30 shows the normalized velocity profile across a turbulent boundary layer.

In the inner region, the mean velocity profile can be approximated as:

$$u^+ = \begin{cases} y^+ & , \quad 0 < y^+ \leq 5 \\ \dfrac{1}{\kappa}\ln(y^+) + C & , \quad 30 \leq y^+ \leq 500\text{-}1000 \end{cases}$$

where $\kappa = 0.41$ is the von Kármán constant and $C = 5.1$ is the Coles' constant, typically used for smooth walls.
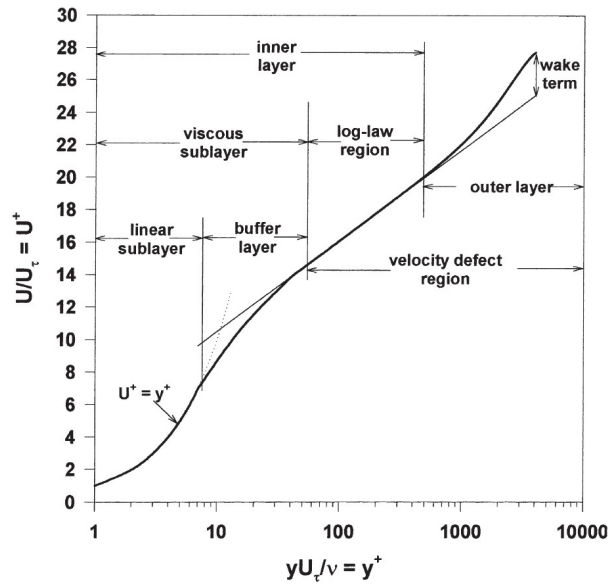
Figure 2.30: Normalized mean velocity profile in a turbulent boundary layer in semi-log coordinates [35]

2.6.4 Thermal Boundary Layer

Analogous to the momentum boundary layer, a *thermal boundary layer* develops at the interface between a solid surface and a fluid due to the presence of a temperature gradient. At the wall, the fluid temperature equals the wall temperature T_w, while in the free stream it asymptotically approaches the bulk fluid temperature T_∞. The thermal boundary layer thickness, δ_T, is defined as the distance y from the wall at which 99% of the temperature difference has been bridged:

$$\frac{T_w - T}{T_w - T_\infty} = 0.99$$

Considering the case of a flat plate with surface temperature T_w and fluid temperature T_∞, the fluid elements near the wall slow down to zero velocity and achieve thermal

equilibrium with the surface. These fluid layers then conduct heat to the adjacent layers, generating a temperature gradient and initiating convective heat transfer from the fluid to the wall. As a result, a thermal boundary layer is established, as also illustrated in Fig. 2.28 [43].

The relative thicknesses of the velocity and thermal boundary layers (typically $\delta_T \neq \delta$) are best understood through the *Prandtl number*, a dimensionless parameter representing the ratio between momentum diffusivity and thermal diffusivity [24]:

$$Pr = \frac{\text{momentum diffusivity}}{\text{thermal diffusivity}} = \frac{\nu}{\alpha} = \frac{\mu c_p}{k}$$

A higher momentum diffusivity (i.e., higher viscosity) results in a thicker velocity boundary layer, as the effects of wall friction penetrate deeper into the flow. The same principle applies to the thermal boundary layer: low thermal diffusivity leads to thinner thermal layers. Therefore, in forced convection, the Prandtl number is a direct indicator of the ratio δ_T/δ. In this study, the Prandtl number has been considered constant and equal to $Pr = 0.71$, as its variation is negligible over the investigated temperature range for air. For $Pr = 0.71$, the thermal boundary layer is thicker than the velocity boundary layer [51].

In turbulent boundary layers, in addition to molecular conduction $\left(\rho c_p \frac{\partial T}{\partial y}\right)$, the contribution of turbulent heat flux $\left(\rho c_p \overline{v'T'}\right)$ becomes significant. Here, v' and T' represent the fluctuating velocity and temperature components, respectively. To account for this, the *turbulent Prandtl number* Pr_t is introduced:

$$Pr_t = \frac{\varepsilon_M}{\varepsilon_H}$$

where ε_M is the eddy diffusivity of momentum and ε_H is the eddy diffusivity of heat. While the molecular Prandtl number Pr is a fluid property, Pr_t is specific to turbulent flows and quantifies resistance to turbulent heat transport [28, 117].

Multiple studies have investigated the influence of Pr on turbulent flows [15, 19, 22, 25, 56, 108, 112]. These works suggest that for $Pr \geq 0.2$, Pr_t is nearly independent of Pr, and is typically assumed to be in the range $Pr_t \approx 0.85 \div 0.9$.

The structure of the thermal boundary layer mirrors that of the velocity boundary layer, with the key difference being the presence of the Pr scaling factor. Using a similar Reynolds decomposition:

$$\theta = T(y) - T_w \quad ; \quad \theta_\tau = \frac{q_w}{\rho c_p u_\tau} \quad ; \quad \theta^+ = \frac{\theta}{\theta_\tau}$$

the non-dimensional temperature profile θ^+ can be expressed as:

$$\theta^+ = \begin{cases} Pr \cdot y^+ & , \quad 0 < y^+ \leq 5 \\ \dfrac{1}{\kappa_\theta} \ln\left(y^+\right) + \beta(Pr) & , \quad 30 \leq y^+ \leq 500 - 1000 \end{cases}$$

45

where $\kappa_\theta = \kappa/Pr_t \approx 0.459$ is the thermal von Kármán constant and $\beta(Pr)$ is a Pr-dependent function that influences the estimation of the heat transfer coefficient. The function $\beta(Pr)$ must be derived empirically or numerically. One definition is:

$$\beta(Pr) = \lim_{y^+ \to \infty} \left[\theta^+(y^+) - \frac{1}{\kappa_\theta} \ln(y^+) \right]$$

In this regards, the most robust framework established to date is the work of Kader and Yaglow [21]. They reviewed some of the proposed correlations for $\beta(Pr)$ and they derived the empirical correlation:

$$\beta(Pr) = 12.5 Pr^{2/3} + 2.12 \ln(Pr) - 5.3 \tag{2.5}$$

Later, Kader [25] revised it to:

$$\beta(Pr) = \left(3.85 Pr^{1/3} - 1.3 \right)^2 + 2.12 \ln(Pr) \tag{2.6}$$

A similar approach was performed by Gowen and Smith [19]. Based on experimental results they proposed a further correlation:

$$\beta(Pr) = 5 \ln \left(\frac{5Pr + 1}{30} + 5Pr + 8.55 \frac{1}{2.5\kappa_\theta} \right) \tag{2.7}$$

Using an integral solution based on the two-layer model and DNS simulations, Pirozzoli [112] derived

$$\beta(Pr) = \frac{1}{\kappa_\theta} \left[\frac{2\pi C_\theta^{2/3}}{3\sqrt{3}} Pr^{2/3} + \frac{1}{3} \log(Pr) - \left(\frac{1}{6} + \frac{1}{2\sqrt{3}} + \frac{2}{3} \log(C_\theta) - \log(\kappa_\theta) \right) \right] + O\left(Pr^{-2/3} \right) \tag{2.8}$$

With the assumed numerical values of constants ($C_\theta \approx 10$) becomes

$$\beta(Pr) = 12.5 Pr^{2/3} + 0.726 \log(Pr) - 6.03 \tag{2.9}$$

which shares the same structure to Eq. (2.6).

Finally, the local heat transfer coefficient h can be derived by combining Fourier's law at the wall (Eq. (2.2)) and Newton's law of cooling (Eq. (2.3)):

$$h = \frac{-k \left. \frac{\partial T}{\partial y} \right|_{y=0}}{T_w - T_\infty}$$

As the wall-to-bulk temperature difference ($T_w - T_\infty$) remains constant and the thermal boundary layer δ_T grows with x, the wall-normal temperature gradient $\left. \frac{\partial T}{\partial y} \right|_{y=0}$ decreases along the streamwise direction. Therefore, the local heat transfer coefficient h also decreases with increasing x.

2.7 Wall-Bounded Turbulent Flows

Unlike external flows, where the boundary layer develops freely over a surface, internal flows are constrained by solid walls, which significantly influence boundary layer development. Internal flows are prevalent in a wide range of engineering applications, such as heating and cooling ducts. In the context of this thesis, a comprehensive understanding of internal flows is crucial for accurately analyzing convective heat transfer phenomena.

The objective of this section is to provide a general overview of the fluid dynamic and thermal characteristics of wall-bounded turbulent flows. This theoretical framework is essential to appreciate the physical mechanisms of convection and to extract reliable heat transfer coefficients under different flow conditions.

Although the turbulent flow relations are typically derived for circular ducts, they can also be applied with reasonable accuracy to non-circular ducts by replacing the diameter D with the *hydraulic diameter*, defined as:

$$D_h = \frac{4A_c}{P}$$

where A_c is the cross-sectional area and P is the wetted perimeter of the duct [30, 58]. Accordingly, the theoretical analysis presented in this section adopts this generalization.

2.7.1 Quantitative Description of Flow Behavior

In internal flows (IF), the hydrodynamic boundary layer develops under confinement due to the duct geometry. At the inlet, the flow initially experiences boundary layer growth near the walls. Due to viscous effects, this layer expands until it spans the entire cross-section, eliminating the inviscid core. At this point, the velocity profile no longer evolves with the axial position, resulting in what is known as a *fully developed flow*. The axial distance from the inlet where this occurs is termed the *hydrodynamic entry length*, $x_{fd,h}$.
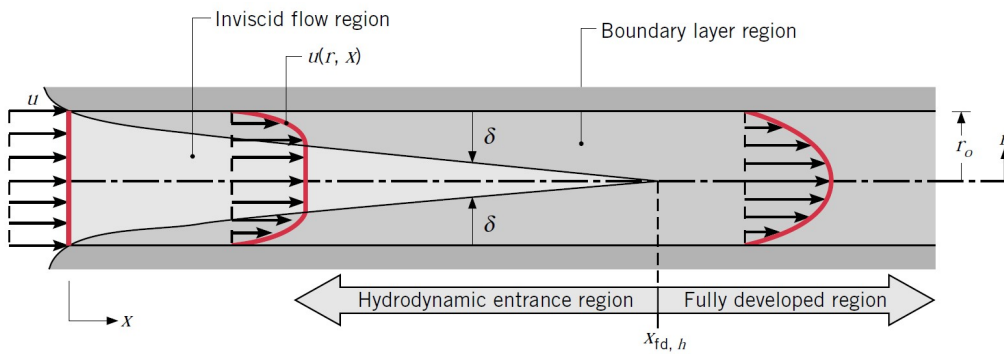
Figure 2.31: Hydrodynamic boundary layer development in a circular tube [42]

47

In fully developed conditions and for symmetric ducts, the velocity profile typically exhibits a maximum at the centerline and decreases towards the walls due to the no-slip condition. The extent of the entry length is mainly governed by the Reynolds number, defined using the bulk velocity $\overline{U}$, the hydraulic diameter D_h, and the kinematic viscosity ν:

$$Re = \frac{\overline{U} D_h}{\nu}$$

The Reynolds number dictates the flow regime within the duct. For a circular cross-section, the transition thresholds are typically:

- $Re < Re_{\mathrm{crit}} = 2300$: Laminar regime

- $2300 \lesssim Re \lesssim 4000$: Transitional regime

- $4000 \lesssim Re < 10^5$: Low turbulence regime

- $Re > 10^5$: Fully turbulent regime

For ducts with non-circular geometries, the critical Reynolds numbers are different, but the same classification applies.

The hydrodynamic entry length is influenced by multiple parameters. It is commonly defined as the axial distance at which the wall shear stress, and thus the friction factor, reaches within 2% of its fully developed value [58]. In laminar flow, both the hydrodynamic and thermal entry lengths depend on Reynolds and Prandtl numbers. However, in turbulent flow, intense mixing due to eddy motions dominates molecular diffusion. As a result, hydrodynamic and thermal entry lengths are approximately equal in magnitude and largely independent of the Prandtl number [58].

A widely used approximation for hydraulic entry length is:

$$\left(\frac{x_{fd,h}}{D_h} \right)_{\mathrm{turb}} = 1.359 \cdot Re_D^{0.25}$$

as proposed by Zhi-Qing et al. [26].

For practical engineering applications, and consistent with the methodology of Incropera et al. [42], fully developed turbulent flow is assumed when:

$$10 \lesssim \left(\frac{x_{fd,h}}{D_h} \right) \lesssim 60$$

2.7.2 Velocity Distribution

For laminar pipe flows, the velocity distribution is characterized by a well-defined analytical expression. The *Hagen-Poiseuille* equation describes the parabolic nature of the velocity profile across the pipe's radius:

$$\frac{U}{U_{max}} = 1 - \left(\frac{r}{R} \right)^2$$

where U is the fluid velocity at a radial position r, U_{max} is the maximum velocity occurring at the pipe centerline, and R is the pipe radius.

The maximum velocity U_{max} can be derived from the balance between the axial pressure gradient and the viscous resistance of the fluid [30]:

$$U_{max} = -\frac{1}{8\mu}\left(\frac{dp}{dx}\right)R^2$$

Here, μ is the dynamic viscosity of the fluid and $\frac{dp}{dx}$ represents the pressure gradient along the pipe's axis. Based on this formulation, the mean fluid velocity $\overline{U}$ can be determined as half the centerline velocity, i.e., $\overline{U} = U_{max}/2$.

For turbulent flows, an analytical solution analogous to the laminar case is not available due to the complexity introduced by turbulence. However, empirical models based on curve-fitting of experimental or numerical data have been proposed. One widely used approximation is the *power law model*, first introduced by Prandtl [47], which expresses the velocity profile as:

$$\frac{U}{U_{max}} = \left(\frac{y}{R}\right)^{\frac{1}{n}}$$

where $y = R - r$ is the distance from the wall, and n is an exponent that typically depends on the Reynolds number. For turbulent flow over smooth surfaces, a commonly used value is $n = 7$ [90].

Despite its practical usefulness, the power law model presents several limitations. First, it lacks a continuous first derivative at the pipe centerline, resulting in a discontinuity in $\frac{dU}{dr}$. Second, it fails to converge to the expected laminar flow profile in scenarios where the Reynolds number is relatively small. To overcome these issues, Salama [90] proposed a modified velocity profile:

$$\frac{U}{U_{max}} = \left[1 - \left(\frac{r}{R}\right)^m\right]^{\frac{1}{n}}$$

where m and n are fitting exponents calibrated to better align the theoretical velocity distribution with experimental and numerical data.

In the referenced study, Salama validated the model by comparing it to CFD simulations across a broad Reynolds number range ($10^4 \leq Re \leq 10^7$). The results indicated that a constant value of $m = 2$ was sufficient for the entire range. The optimal value of n was found to follow a logarithmic relation with respect to the Reynolds number:

$$n = 0.77\ln(Re) - 3.47$$

Although Salama suggested that the model could be generalized to non-circular cross-sections, such as square ducts, a fully developed theoretical formulation for such geometries has yet to be established in the literature.

2.7.3 Darcy Friction Factor and Moody Diagram

In internal flows, it is essential to quantify the pressure drop along a given pipe length caused by viscous stresses on the channel walls, as this directly impacts the energy required by a fan or pump to sustain the flow. This consideration is particularly critical in turbine cooling channels, in order to guarantee a reliable cooling performance.

A commonly used parameter to evaluate the pressure drop is the *Darcy-Weisbach friction factor*, f_D, defined in Eq. (2.10). It incorporates the pressure difference Δp along D, the fluid density ρ, and the mean flow velocity $\overline{U}$ [42]:

$$f_D = \frac{\Delta p}{L} \cdot \frac{D}{\frac{1}{2}\rho\overline{U}^2} \tag{2.10}$$

In this formulation, hydrostatic or gravitational effects are neglected, and the pressure drop is assumed to arise solely from wall shear stress τ_w:

$$\tau_w = \frac{\text{frictional force on fluid}}{\text{pipe surface area}} = \frac{\Delta p\left(\frac{\pi}{4}D_h^2\right)}{\pi D_h L} = \frac{\Delta p D_h}{4L}$$

Accordingly, the friction factor f_D can also be expressed as:

$$f_D = \frac{8\tau_w}{\rho\overline{U}^2}$$

The Darcy friction factor should not be confused with the friction coefficient, often referred to as the Fanning friction factor, which is defined as [42]:

$$C_f = \frac{2\tau_w}{\rho\overline{U}^2} = \frac{f_D}{4}$$

For fully developed laminar flow in a circular pipe, the friction factor is determined directly from Poiseuille's law:

$$f_{D,\text{laminar}} = \frac{64}{Re}$$

This relation indicates that, under laminar conditions, the friction factor depends solely on the Reynolds number and is independent of surface roughness.

For fully developed turbulent flows, various empirical correlations exist to compute the Darcy friction factor. The most well-known is the Colebrook-White equation [8], which must be solved iteratively due to its implicit form:

$$\frac{1}{\sqrt{f_D}} = -2 \cdot \log\left(\frac{k_s/D_h}{3.7} + \frac{2.51}{Re\sqrt{f_D}}\right) \tag{2.11}$$

For both laminar and turbulent regimes, the friction factor can also be determined graphically using the Moody diagram [11], provided the Reynolds number and relative roughness are known. The Moody diagram is presented in Fig. 2.32. It illustrates that in the fully rough regime, the friction factor becomes solely a function of relative roughness.
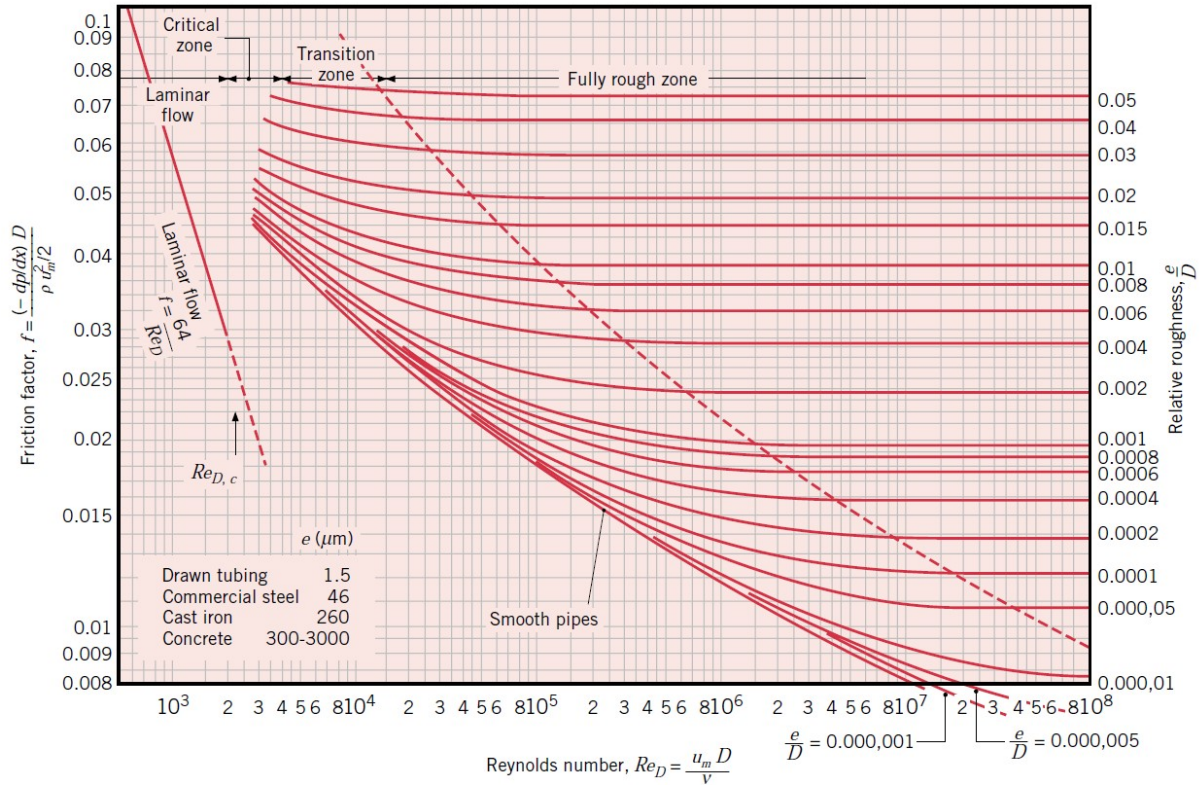
Figure 2.32: Friction factor for fully developed flow in a circular tube [42]

The Moody diagram expresses the friction factor as a function of the Reynolds number and the relative roughness:

$$f_D = f_D\left(Re, \frac{k_s}{D_h}\right)$$

From the diagram, it is evident that, for a given relative roughness, the flow is laminar at low Reynolds numbers, it transitions at a critical Reynolds number Re_{crit}, it enters the transitional regime, and it eventually reaches the fully turbulent regime. In the latter, the friction factor reaches a plateau. As the relative roughness increases, this turbulent plateau is reached at lower Reynolds numbers.

However, in cases where the surface roughness is non-uniform or randomly distributed, accurately characterizing the relative roughness becomes more challenging, as illustrated in Fig. 2.33.

The presence of surface roughness significantly affects the wall shear stress and, hence, the pressure loss. Roughness alters the near-wall behavior of the boundary layer, increasing the momentum transfer and thus the wall friction. From a flow mechanics standpoint, a surface is typically considered rough when the peak-to-valley roughness exceeds the thickness of the viscous sublayer.

2.7.4 Roughness Consideration and Characterization

To characterize the influence of surface texture on flow dynamics, a conventional roughness representation was proposed by Nikuradse [12]. In his experiments, the wall was uniformly coated with a layer of densely-packed spherical particles. This configuration, illustrated in Fig. 2.33(a), defines the particle diameter as the *sand-grain roughness height*, denoted by k.
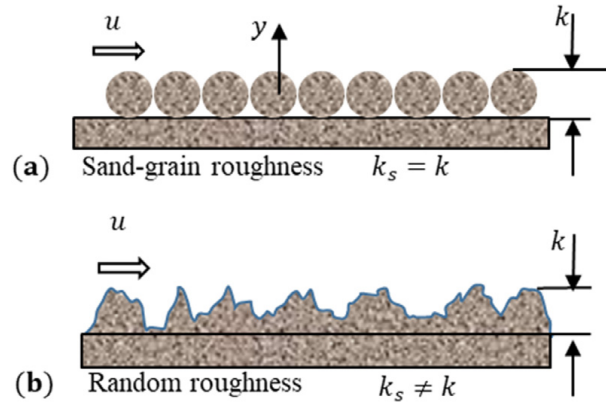
Figure 2.33: Equivalent sand-grain roughness [88]

Using the characteristic length of the near-wall region, a non-dimensional roughness parameter is derived to quantitatively express surface roughness. This is the *Roughness Reynolds number*, defined as:

$$k_s^+ = \frac{k_s u_\tau}{\nu}$$

Surface roughness modifies the classical law of the wall, particularly within the viscous sublayer. The interaction between the turbulent boundary layer and the rough surface is typically classified into three regimes, based on the roughness Reynolds number k_s^+. These regimes are delineated by two critical thresholds, k_{Smooth}^+ and k_{Rough}^+ [88]:

- *Hydraulically Smooth Regime $k_s^+ < k_{\text{Smooth}}^+$*:
  The roughness elements remain entirely submerged within the viscous sublayer; hence, skin friction and drag are unaffected.

- *Transitionally Rough Regime $k_{\text{Smooth}}^+ < k_s^+ < k_{\text{Rough}}^+$*:
  In this regime, both Reynolds number and relative roughness influence the drag.

Friction arises from both viscous and pressure forces, making the effect of roughness complex and non-linear.

- *Fully Rough Regime $k_s^+ > k_{Rough}^+$:*
  The roughness elements protrude through the viscous sublayer into the fully turbulent region, shifting the logarithmic velocity profile *downward*. Viscous effects are negligible (the viscous sublayer is entirely destroyed by the large turbulence mixing caused by roughness elements), and the pressure drag dominates.

Values for k_{Smooth}^+ and k_{Rough}^+ vary in literature [88].
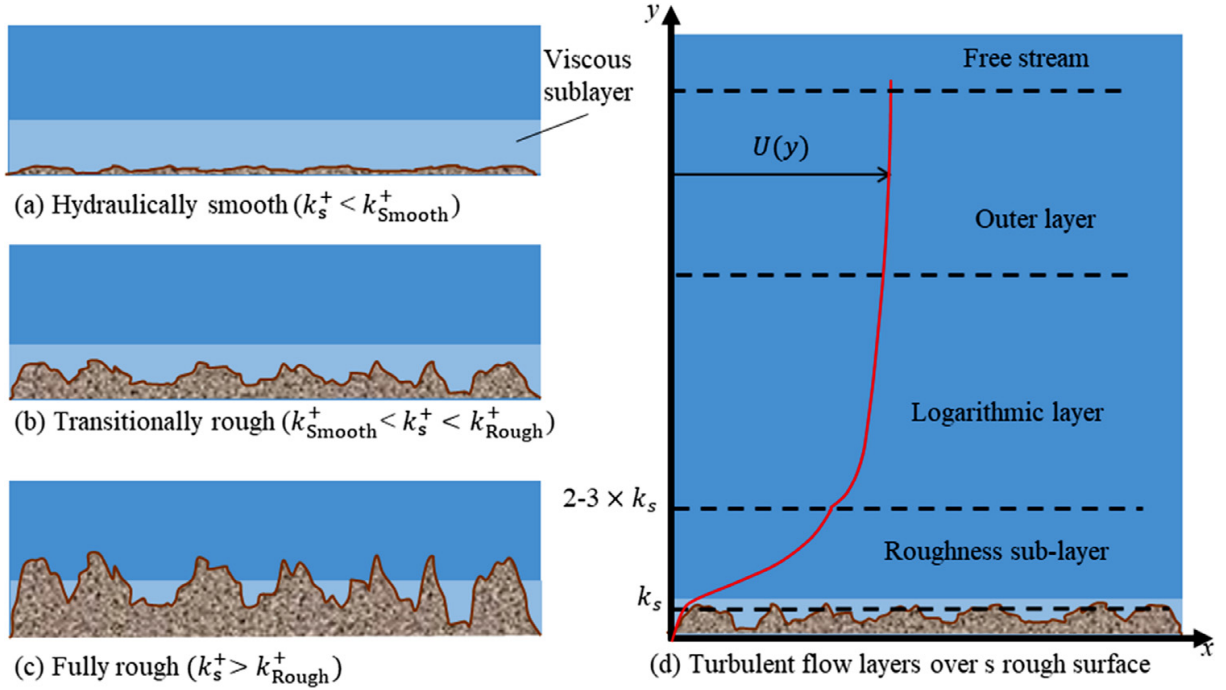
Figure 2.34: Turbulent flows over rough surfaces [88]: (a) hydraulically smooth, (b) transitionally rough, (c) fully rough, (d) schematic of velocity profile $U(y)$ over roughness with roughness sublayer, logarithmic layer, and outer layer.

The effect of surface roughness on velocity profiles is captured via the *roughness function*, ΔU^+, introduced independently by Clauser [13] and Hama [14]. This function quantifies the downward shift in the logarithmic velocity profile, representing a momentum deficit due to surface roughness. A positive ΔU^+ implies increased drag compared to a smooth wall, whereas negative values would indicate drag reduction. The logarithmic velocity profile over a rough wall is given by:

$$u^+ = \frac{1}{\kappa}\ln(y^+) + C - \Delta U^+ \tag{2.12}$$

for turbulent flow over rough walls, where κ represents the von Kármán constant and C is the smooth wall intercept. Alternatively, this can be expressed in relative rough-

ness form Eq. (2.13), where k is a measure of the roughness height:

$$u^+ = \frac{1}{\kappa} \ln\left(\frac{y^+}{k^+}\right) + C - \Delta U^+ + \frac{1}{\kappa} \ln(k^+) \tag{2.13}$$

A widely used scale for roughness is the equivalent sand-grain roughness height k_s. Nikuradse showed that ΔU^+ can be estimated from the size of mono-dispersed sand grains used in his experiments. For uniform sand-grain surfaces, a typical logarithmic intercept value is approximately 8.5 [12], allowing one to estimate k_s for a known roughness function:

$$C - \Delta U^+ + \frac{1}{\kappa} k_s^+ = 8.5$$

This relation is widely adopted, as shown in the work of Kadivar et al. [88].
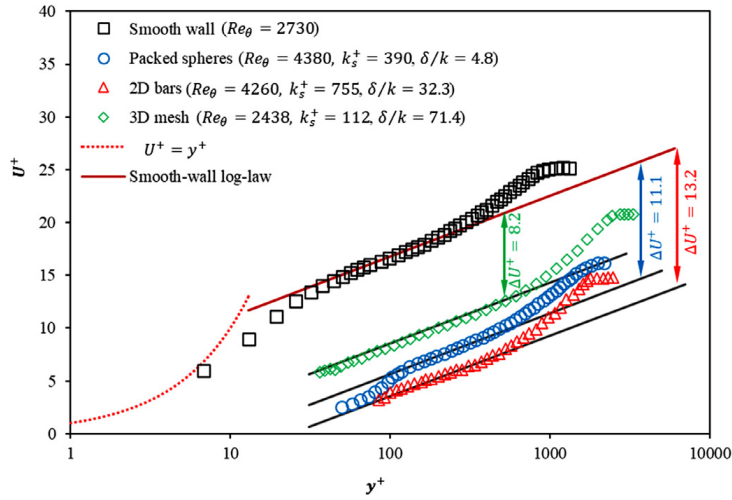
Figure 2.35: Downward shift of the mean velocity profile for different rough surfaces [88]

Unlike momentum transfer, no direct analogy exists for heat transfer over rough surfaces. In the fully rough regime, while wall shear stress τ_w scales with inertial flow properties, the wall heat flux q_w does not. Instead, it depends on both flow conditions and molecular properties such as the Prandtl number. This distinction underscores the separate impacts of roughness and molecular properties on convective heat transfer under fully rough conditions.

Analogous to the velocity profile, the logarithmic temperature profile experiences a downward shift over rough walls, resulting in enhanced heat transfer [21, 25] and in a downward shift of the logarithmic temperature profile. The temperature profile can be expressed as:

$$\theta_R^+ = \theta_S^+ - \Delta\theta^+(k_s^+, Pr)$$

where $\Delta\theta^+$ is the *temperature shift*, and θ_S^+ is the smooth-wall temperature profile. While ΔU^+ depends solely on k_s^+, $\Delta\theta^+$ depends on both k_s^+ and Pr. The smooth-wall log-law intercept $\beta(Pr)$ is determined such that $\Delta\theta^+ = 0$ for smooth walls. A positive $\Delta\theta^+$ denotes heat transfer enhancement. For $k_s^+ \ll 1$ and $Pr \cdot k_s^+ \ll 1$, the enhancement becomes negligible.

The trends reported in [117, Fig. 17(a)] indicate that increasing Pr results in higher $\Delta\theta^+$. Moreover, the dependence of $\Delta\theta^+$ on Pr is stronger than on k_s^+ or roughness topology. Figures [117, 17(b)] and [117, Fig. 17(c)] illustrate the sensitivity of $\Delta\theta^+$ to roughness skewness and density. Notably, positive skewness enhances heat transfer more than negative skewness, with minimal impact observed in the transitionally rough regime. Figure [117, 17(c)] shows that the influence of frontal solidity λ_f differs between regimes: in the transitionally rough regime, higher $\Delta\theta^+$ corresponds to lower λ_f, while in the fully rough regime, higher λ_f increases $\Delta\theta^+$.

2.7.4.1 *"d-type"* and *"k-type"* Roughness

The terms **k**-*type* and **d**-*type* roughness refer to classifications of two-dimensional roughness geometries, such as spanwise ribs and grooves. The distinction between them was originally introduced by Perry et al. [20]. In general, *d-type* roughness describes tightly packed configurations, while *k-type* refers to widely spaced arrangements. Notably, *k-type* two-dimensional roughness exhibits similar behavior to random three-dimensional roughness.

A key parameter for distinguishing these roughness types is the surface density, which Schlichting [7] quantified using the frontal solidity parameter λ_f. This distinction led to the identification of two primary regimes: a sparse regime with $\lambda_f < 0.15$, where roughness effects increase with increasing frontal solidity, and a dense regime, where mutual sheltering among roughness elements diminishes their impact. In the sparse regime, the additional drag introduced by roughness is expected to scale proportionally with the frontal area of the elements, as expressed through λ_f [36].

Building on these foundations, Coleman et al. [41] conducted experiments to investigate the flow structures within the cavities formed by ribs of uniform cross-section. They identified three roughness types based on the pitch-to-height ratio L/H: *d-type*, *intermediate*, and *k-type*. Here, L is the spacing between ribs and H is their height. For closely spaced (*d-type*) ribs, stable separated eddies form within the cavities with minimal influence on the outer flow. In contrast, widely spaced (*k-type*) ribs allow reattachment before the next element and promote eddies that interact with the boundary-layer edge. A transition from *d-type* to *k-type* behavior was observed at $W/h \approx 5$, where W is the rib spacing.

The mean flow over ribs generally comprises two counter-rotating vortices, and the velocity profile above the roughness is quasi-logarithmic. Below the roughness crests, the interfacial velocity profile transitions from exponential ($W/h < 10$), to linear ($W/h \geq 10$), and eventually to logarithmic ($W/h \gg 10$), depending on rib spacing. Surfaces
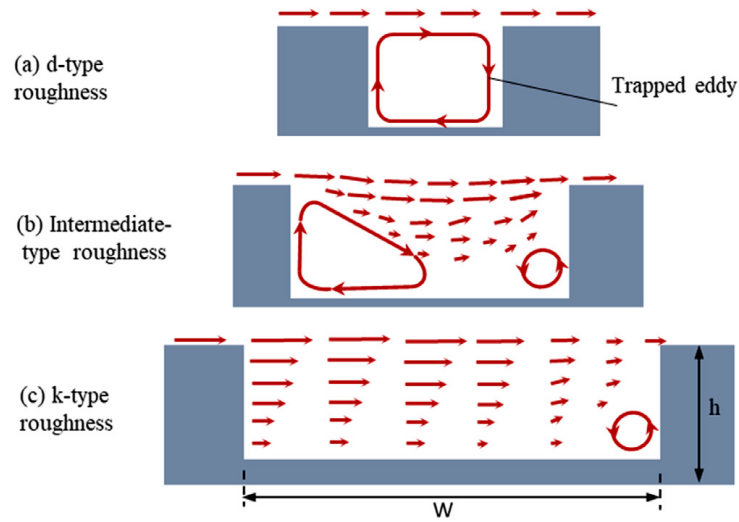
Figure 2.36: Schematics of (a) *d-type* with trapped eddy, (b) *intermediate-type* roughness with two eddies of different strength as well as separation and reattachment of flow between roughness elements, and (c) *k-type* roughness with boundary layer velocity structure and a small eddy on the windward side of a roughness element [88].

with groove widths exceeding approximately $(3 \div 4)k$ tend to behave like *k-type* surfaces and maintain recirculation bubbles that reattach before the subsequent roughness element, thereby exposing it to the external flow.

It is important to highlight that *d-type* roughness can contribute to drag reduction by trapping recirculating fluid within the cavities. This characteristic makes it particularly relevant in heat transfer applications, where controlled flow behavior within roughness cavities may influence local thermal performance.

2.7.4.2 Equivalency Model

When the shape of surface roughness deviates from that of sand grains, a single parameter such as the sand-grain roughness is no longer sufficient to describe it. In such cases, geometric parameters may be used to characterize the surface [49].

Inspired by the pioneering studies of Nikuradse [12], Schlichting [7] introduced the concept of equivalent sand-grain roughness k_s. This quantity represents the diameter of uniform (monodisperse), close-packed sand grains on a hypothetical surface, as shown in Fig. 2.33(b), that would induce the same drag as the surface of interest under the same flow conditions in the fully rough regime. Although k_s is a length scale, it does not measure a physical distance. Rather, it is a hydraulic parameter defined by drag, typically determined experimentally or via simulations for a given rough surface. This is the roughness height referenced in the Moody diagram [11], offering a common basis for comparing different rough surfaces in wall-bounded turbulence and serving as an input for predictive models such as RANS or rough flat-plate computations. However, the simplicity of this parameter may be misleading: k_s is often

misused either as a direct geometric measure or inferred solely from surface geometry, which may lead to incorrect estimations [86].

According to Chung et al. [86], an accurate estimation of k_s, and therefore of the associated drag and heat transfer coefficients, requires incorporating one parameter from each roughness category: height, spatial distribution, and spectral characteristics. Parameters such as skewness, effective slope, and RMS height (S_q) have previously been correlated with k_s. Compared to Gaussian surfaces, positive skewness tends to increase friction drag, while negative skewness reduces it. This is attributed to the dominance of form drag in the former and the so-called "skimming" effect in the latter, where the flow passes over deep valleys in the roughness [117].

In the context of friction factor estimation using the Colebrook-White equation (Eq. (2.11)), the relative roughness k_s/D_h is commonly approximated as R_z/D_h, where R_z represents the average of the five maximum peak-to-valley heights of the surface (see Sec. 2.3.1.3). However, for randomly rough surfaces, k_s is not directly applicable. In such cases, relative roughness is expressed using alternative roughness metrics or empirical correlations among several parameters. For example, Stimpson et al. [69] proposed the following correlation for additively manufactured surfaces:

$$\frac{k_s}{D_h} = 18\left(\frac{R_a}{D_h}\right) - 0.05$$

Nevertheless, this topic remains under active research, and no universally accepted correlation currently exists.

2.7.5 Heat Transfer of Internal Flows

After analyzing the hydrodynamic behavior of internal flows, the thermal aspects are addressed.
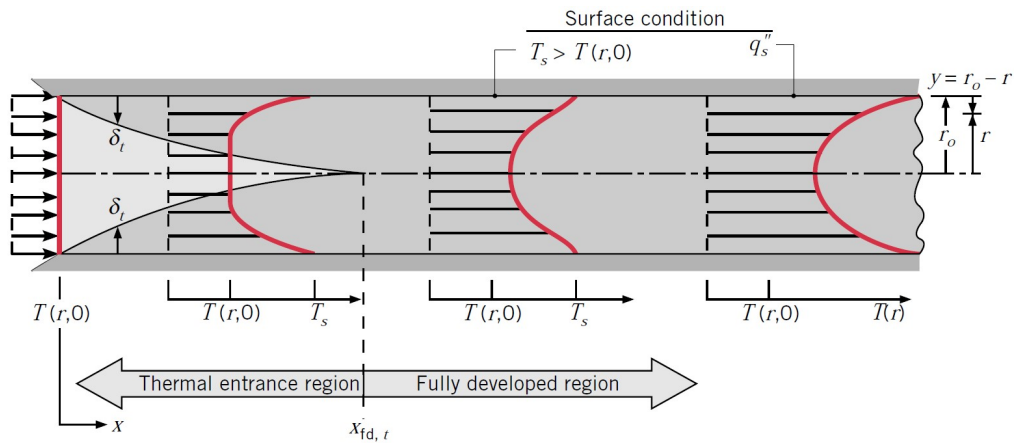
Figure 2.37: Thermal boundary layer development in a heated circular tube [42]

When a fluid enters a duct at uniform temperature T_0, convective heat transfer leads

to the development of a temperature profile. The wall boundary condition can be either a constant temperature T_w or a constant heat flux $\dot{q}_w$. Near the duct inlet, the temperature profile starts evolving due to thermal interaction with the wall. As the flow progresses downstream, the portion of the cross-section at $T(r) = T_0$ progressively diminishes until it disappears completely. The axial distance at which this occurs is referred to as the thermal entrance length $x_{fd,t}$. Beyond this point, the temperature profile depends on the applied boundary condition, as illustrated in Fig. 2.37, and the flow is said to be in the *thermally fully developed region*.

For laminar flow, the thermal entrance length can be approximated as [28]:

$$\left(\frac{x_{fd,t}}{D_h} \right)_{\text{lam}} = 0.05 \cdot Re_D \cdot Pr$$

For turbulent flow, a practical approximation is:

$$\left(\frac{x_{fd,t}}{D_h} \right)_{\text{turb}} = 10$$

In the thermally fully developed region, the bulk fluid temperature continues to rise with x, leading to the question: why is it termed "fully developed" if temperature gradients is still present? Unlike the hydrodynamic case, where the velocity gradient $\partial u / \partial x = 0$ in the fully developed region, there is no axial point at which $\partial T_\infty / \partial x = 0$ due to the continuous convective heat exchange. However, when working with dimensionless temperature such as $(T_w - T)/(T_w - T_\infty)$, a formal condition for thermally fully developed flow can be defined as:

$$\frac{\partial}{\partial x} \left[\frac{T_w(x) - T(r,x)}{T_w(x) - T_\infty(x)} \right]_{fd,t} = 0$$

Moreover, the radial temperature derivative also becomes independent of x:

$$\frac{\partial}{\partial r} \left(\frac{T_w - T}{T_w - T_\infty} \right)_{r=r_0} = \frac{- \frac{\partial T}{\partial r} \big|_{r=r_0}}{T_w - T_\infty}$$

Applying Fourier's law, $\dot{q}_w = -k \frac{\partial T}{\partial r} \big|_{r=r_0}$, this leads to:

$$\frac{h}{k} \neq f(x)$$

Thus, in thermally fully developed flow with constant fluid properties, the local convection coefficient h becomes constant and independent of axial location. In contrast, within the thermal entrance region, h varies with x: it starts at high values near the entrance and decays downstream as the thermal boundary layer develops, eventually

stabilizing at the value corresponding to the fully developed region, as depicted in Fig. 2.38.
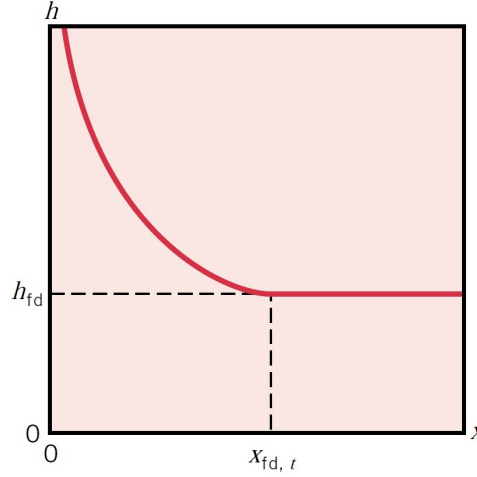
Figure 2.38: Axial variation of the convective heat transfer coefficient in a circular tube [42]

2.7.5.1   Heat Transfer Correlations

In many experimental setups, direct measurement of the convective heat transfer coefficient is a challenging task to perform. Consequently, empirical correlations are commonly employed to estimate the convective heat transfer rate via the Nusselt number.

Numerous correlations exist in the literature for fully developed turbulent flow in circular tubes, most of which are derived from experimental data. Among these, two of the most widely used are presented below.

The *Dittus-Boelter* equation applies to smooth circular tubes under conditions of small to moderate temperature differences between the fluid and the wall. It assumes constant fluid properties evaluated at the bulk mean temperature T_∞:

$$Nu = 0.023 \, Re^{4/5} \, Pr^n \qquad \text{for} \quad \begin{cases} 0.7 \leq Pr \leq 160 \\ Re_D \geq 10^4 \\ \dfrac{L}{D_h} \geq 10 \end{cases}$$

where $n = 0.4$ for heating ($T_w > T_\infty$) and $n = 0.3$ for cooling ($T_w < T_\infty$).

When compared with experimental results, the Dittus-Boelter equation may exhibit uncertainties as large as 25%.

To reduce this error, more accurate, but also more complex, correlations have been developed. One of the most reliable is the correlation proposed by Gnielinski, which is

applicable over a wide Reynolds number range and extends into the transition region. It also incorporates the Darcy friction factor f_D, which can be determined from the Moody diagram:

$$Nu = \frac{\left(\frac{f_D}{8}\right)(Re - 1000)\,Pr}{1 + 12.7\left(\frac{f_D}{8}\right)^{1/2}(Pr^{2/3} - 1)}\left[1 + \left(\frac{D_h}{L}\right)^{2/3}\right] \quad \text{for} \quad \begin{cases} 0.5 \le Pr \le 2000 \\ 3 \cdot 10^3 \le Re_D \le 5 \cdot 10^6 \end{cases}$$

This formulation accounts for the development of the turbulent boundary layer; thus, the minimum Reynolds number for its validity is not fixed but rather depends on flow entrance conditions.

When the length-to-diameter ratio $\frac{L}{D_h}$ is small, entrance effects become significant. These arise due to boundary layer growth and the *vena contracta* phenomenon near sharp inlet edges. To capture the resulting heat transfer enhancement in this region, Mills proposed a correction factor that adjusts the Nusselt number in the entrance region (Nu_x) relative to the fully developed value (Nu_∞) from the Gnielinski correlation [16]:

$$\frac{Nu_x}{Nu_\infty} = 1 + \frac{8.7}{\frac{L}{D_h} + 5}$$
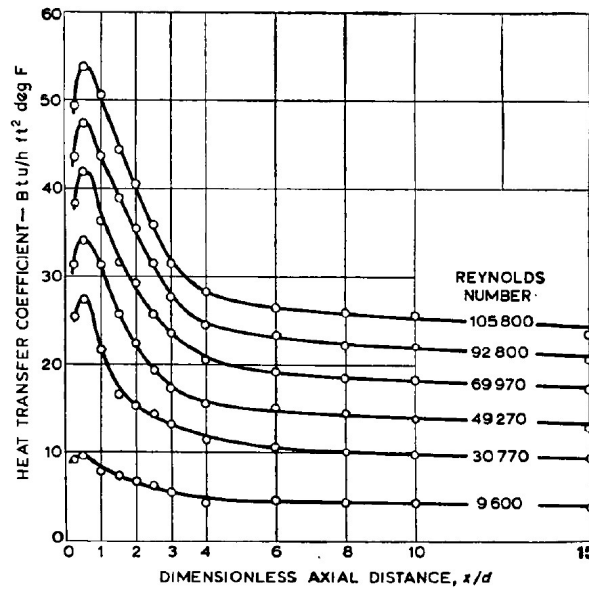
Figure 2.39: Local heat transfer coefficients for a sharp 90° edge entrance [16]

2.8   Hot-Wire Anemometry

Hot-Wire Anemometry (HWA) is a diagnostic technique widely used for measuring instantaneous flow velocity components, particularly in turbulent flows. It operates

on the principle of convective heat transfer from a heated wire to the surrounding fluid. A thin wire (typically made of platinum, tungsten, or nickel), with diameter on the order of microns, is electrically heated and placed in the flow. As fluid passes over the wire, heat is transferred away from the wire, leading to a change in its electrical resistance.

By maintaining the wire at a constant temperature (Constant Temperature Anemometry, CTA) or at a constant current (Constant Current Anemometry, CCA), the heat loss can be correlated to the local fluid velocity through empirical or theoretical calibrations. CTA systems are preferred for high-frequency turbulence measurements due to their superior temporal response.

The King's Law is typically used to relate the velocity to the electrical signal in CTA systems:

$$E^2 = A + B U^n$$

where E is the voltage across the wire, U is the flow velocity, and A, B, and n are calibration constants determined experimentally.

HWA is highly sensitive and capable of resolving small-scale turbulent fluctuations, but it requires careful calibration and is sensitive to temperature variations and probe contamination.

2.9   Thermocouple

The operating principle of thermocouples is based on the Seebeck effect, which states that when two dissimilar metals form a closed circuit with two junctions maintained at different temperatures, an electromotive force (e.m.f.) is generated in the circuit. The magnitude of this e.m.f. depends on the materials being used and it is approximately proportional to the temperature difference between the two junctions.

The thermoelectric voltage is given by:

$$\text{e.m.f.} = \alpha_S \, \Delta T$$

where α_S is the Seebeck coefficient and ΔT is the temperature difference between the hot and reference junctions.

Thermocouples are commonly used for temperature measurements in both steady and transient heat transfer experiments due to their robustness, small size, and fast response time. However, they require careful compensation for cold-junction (reference junction) temperature and often need signal conditioning due to the low voltage output.

Different thermocouple types (e.g., Type K, Type J) are available depending on the required temperature range, sensitivity, and environmental conditions.

Chapter 3

Research Methodology

This chapter outlines the methodology employed to achieve the research objectives of this thesis. It begins with a description of the functionality of the SRHT (Surface Roughness Heat Transfer) rig and the generation of the rough surface models. Subsequently, the experimental setup and calibration procedures are presented. The chapter then details the experimental procedure and the data processing methods applied to extract meaningful results. Finally, an uncertainty analysis is conducted to evaluate the reliability of the measurements and results.

3.1   Functionality of the SRHT Rig

The key descriptive parameter for forced convection is the heat transfer coefficient, h, which is defined as the ratio of the surface heat flux, $\dot{q}$, to the temperature difference between the wall surface temperature, T_w, and the free-stream temperature, T_∞. Since the heat transfer coefficient cannot be directly measured, it is typically estimated through inverse heat conduction techniques using transient surface temperature measurements [66]:

$$h = \frac{\dot{q}}{T_\infty - T_w}$$

The SRHT rig is based on this principle and is designed to investigate the local heat transfer characteristics on the bottom wall of a rectangular duct. A schematic overview of the rig's functionality is provided in Fig. 3.2.

The setup consists of a flow straightener, a bypass channel, and a test section. A hatch allows the redirection of the flow between the bypass and the test section. Initially, the hatch remains closed, directing the heated airflow through the bypass (Fig. 3.1(a)). Once the target flow temperature is reached, the hatch is quickly opened to flood the test section with the heated flow. The bottom plate (referred to as the "wall") is exposed to this incoming flow, which causes it to heat up. An Infrared Camera (IRC)

captures the transient surface temperature through optical windows positioned at various locations along the duct, as shown in Fig. 3.1(b).
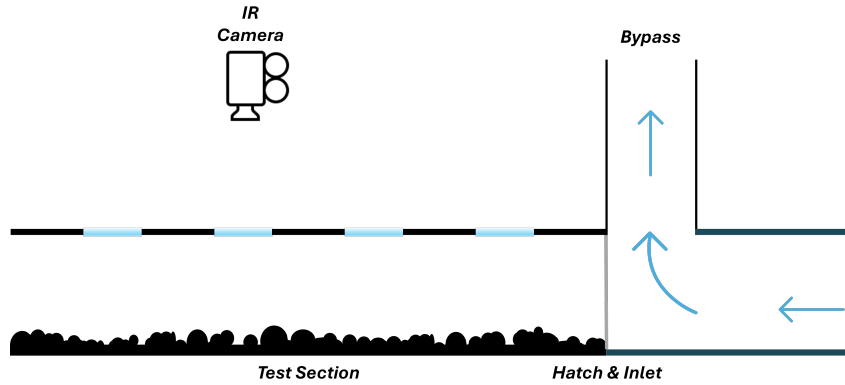
(a) Schematic configuration of the flow behavior when the bypass is open and the hatch is closed: heating of the flow in bypass mode.
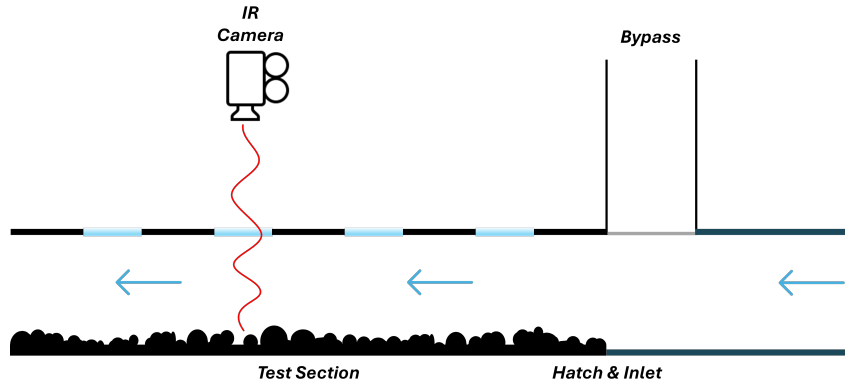
(b) Schematic configuration of the flow behavior when the bypass is closed and the hatch is opened: IR camera records the bottom plate heating.

Figure 3.1: Schematic representation of the SRHT rig's functionality

3.1.1 Dynamic Similarity

For meaningful experimental results using a scaled model in a channel, it is essential to ensure dynamic similarity. This implies that both the scaled model and the real system must satisfy the conditions for similarity in fluid dynamics:

- The model and prototype must be *geometrically similar*, with corresponding features placed at the same relative orientations, especially critical for inclined flow cases.

- All relevant dimensionless parameters (similarity parameters), such as Reynolds and Prandtl numbers, must match to ensure that the governing physical phenomena remain comparable.

A more comprehensive discussion on dimensionless numbers and their derivation is provided in Appendix A.

3.1.2 Working Principle
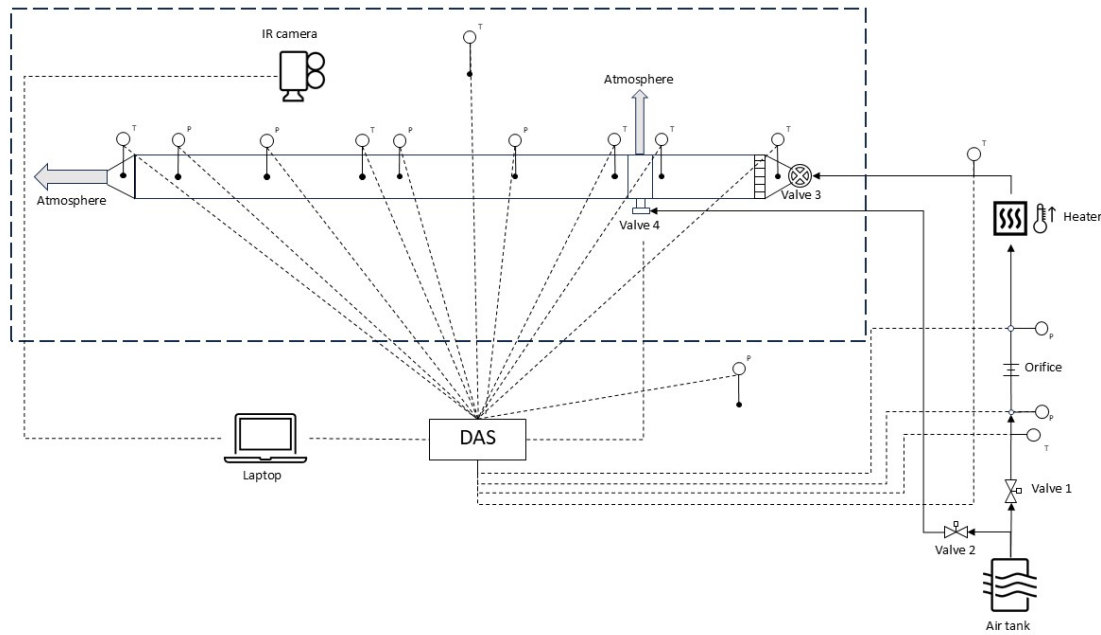
Figure 3.2: Process flow diagram for the SRHT test rig

The SRHT rig operates using a pressurized air system at $8\,bar$. As shown in the diagram, Valve 1 controls the main air supply to the test section, while Valve 2 is connected to the pneumatic actuator that opens the hatch. Downstream, the air passes through an orifice meter, where the pressure drop is used to calculate the mass flow rate. A heating unit raises the flow temperature, which is monitored immediately downstream using a thermoelement.

Before reaching the test section, the flow enters the laboratory chamber, indicated by the dashed outline in Fig. 3.2. Here, a pressure reducing valve (Valve 3) lowers the pressure to $1.5\,bar$, also functioning as a mass flow regulator. The flow continues to a three-way valve (Valve 4) that determines whether it enters the bypass or the test section. Just upstream of Valve 4, a PT100 sensor measures the temperature used to determine when the test should begin. An additional PT100 probe, used as a safety check, is positioned between the honeycomb of the flow straightener and Valve 3 to detect thermal anomalies.

Three thermocouples are located at the inlet, mid-section, and outlet of the test section, each placed at the duct centerline. These readings are linearly interpolated to

determine the streamwise bulk temperature T_∞. Pressure taps positioned at multiple axial locations provide relative pressure data for flow characterization.

To match the operating conditions found in real applications, the temperature and mass flow rate are adjusted to achieve a desired Reynolds number:

$$Re = \frac{\dot{m}D_h}{\mu_{\text{air}}A} \tag{3.1}$$

where $\dot{m} = \rho u_\infty A$ $[kg/s]$ is the mass flow rate, A is the cross-sectional area, ρ is the air density, μ_{air} is the dynamic viscosity (evaluated via Sutherland's law), and D_h is the hydraulic diameter of the duct.

Industrial-scale turbines typically operate at high Reynolds numbers, often spanning 10^4 to 10^6 [48]. This study employs scaled-up models of cooling duct geometries derived from Siemens Energy gas turbines (SGT600-700 and SGT800 series). Recent investigations by Siemens reveal that cooling flows in these turbines exhibit Reynolds numbers typically ranging from 10^4 to 10^5, depending on the geometry and operating conditions. As a result, the experiments in this work are conducted within the same Reynolds number range to maintain flow similarity.

It is important to note that results obtained under these conditions must be carefully interpreted when extrapolated to real turbine applications. Accurate empirical or semi-empirical correlations are needed for reliable prediction, rather than simple extrapolation.

In the following sections, the methodology used to collect and process experimental data will be presented in detail.

3.2 Analogue Rough Surfaces Modelling

The test objects used in this study are rough surface plates with dimensions of $90\,mm$ in width, $150\,mm$ in length, and $15\,mm$ in height. These objects were modelled by previous students [103, 105, 106] based on the surface roughness characteristics of materials commonly employed in turbine cooling channels at Siemens Energy. At the current stage of research, three different upscaled roughness configurations have been identified. These configurations are referred to as *analogue surfaces*, and they are inspired by the surface features induced in *Inconel 939* and *Aluminium* during the Laser Powder Bed Fusion (L-PBF) process. The upscaling factor s is calculated as the ratio between the hydraulic diameter of the SRHT duct and that of the real micro-channel:

$$s = \frac{D_{h,\text{SRHT-rig}}}{D_{h,\text{real channel}}}$$

The use of upscaled rough surfaces to mimic additive manufacturing (AM) surfaces was first introduced by Clemenson et al. [70] and further explored by Hanson et al.

[75]. The core concept is to randomly distribute spheres of various diameters on a smooth substrate, replicating the surface morphology of AM structures.

Micro-channels fabricated by L-PBF with a 90° printing angle and varying diameters were previously tested in the qSSHT-rig to assess their hydraulic and thermal behaviour, as described by Pagani [99]. Sections of these channels were cut open to allow for a more detailed roughness characterization.

A skidless contact stylus profilometer was employed to measure the surface topography. As illustrated in Fig. 3.3(a), one half of a cut-opened channel was placed under the stylus, which traversed the channel length and recorded surface height variations. An example of the resulting profile is shown in Fig. 3.3(b).
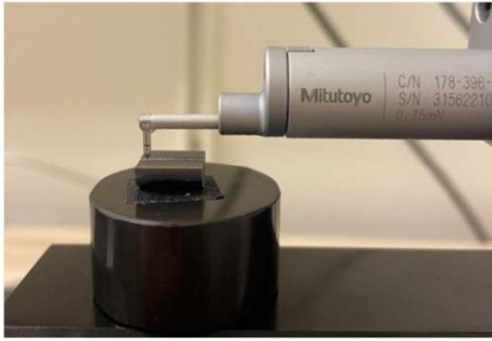
(a) Profilometer Mitutoyo Surftest SJ-410 during measurement
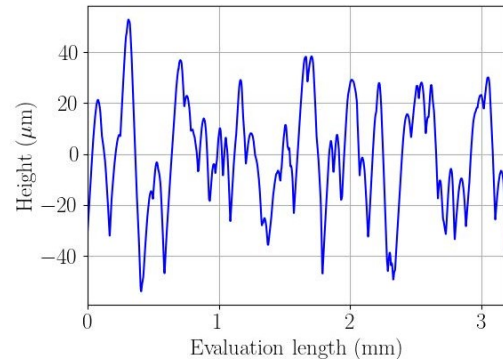
(b) Example of a recorded surface profile

Figure 3.3: Surface roughness measurement of the test objects [105]

High-resolution surface images were also obtained using a *Jeol JSM-IT500* Scanning Electron Microscope (SEM), as shown in Fig. 3.4. The micrographs revealed a stochastic distribution of spherical particles (residual powder) and larger topographical features such as ridges and valleys. In order to replicate these surfaces, a quantitative assessment of the spherical element distribution was necessary. Lehmann [103] and Brogliato [106] performed this analysis manually, by selecting visible spheres from SEM images and recording their diameters. Although this method introduces subjectivity and variability, it captures the overall diameter trend. Interestingly, different statistical models were found to fit different materials: Wen [105] reported that a Gamma distribution better captured the distribution for *Inconel 939*, whereas Brogliato [106] employed a Normal distribution for *Aluminium*.

To faithfully reproduce the real surface, the sphere density must also be preserved. This density ρ_s is calculated by dividing the number of manually selected spheres by the scaled area of the corresponding micrograph:

$$\rho_s = \frac{\text{number of spheres}}{A \cdot s^2}$$

(a) *Inconel 939*   (b) *Aluminium*
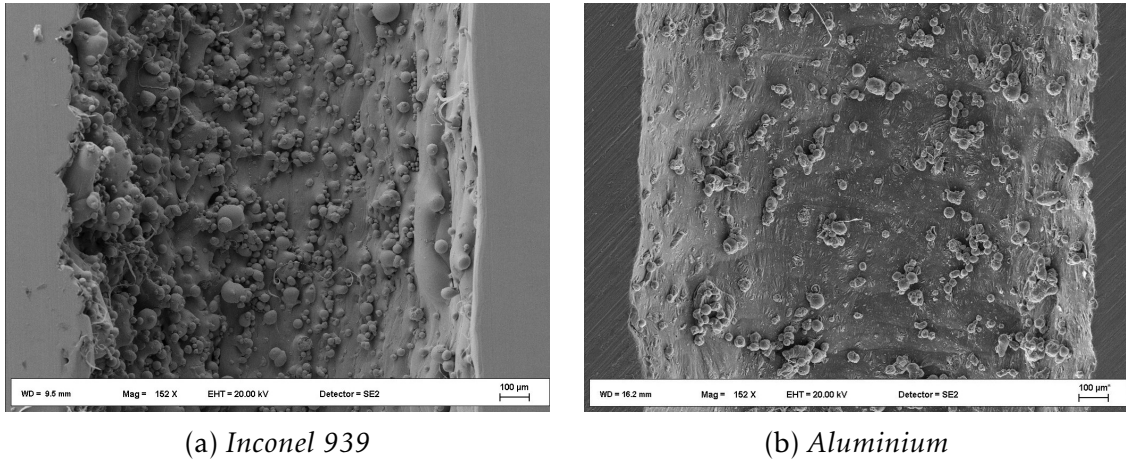
Figure 3.4: SEM images of AM micro-channel internal surfaces

where the area A is computed as:

$$A = \frac{\pi}{2} R \cdot L$$

with R denoting the channel radius and L the image length.

(a) *Inconel 939.*   (b) *Aluminium 1.*   (c) *Aluminium 2.*
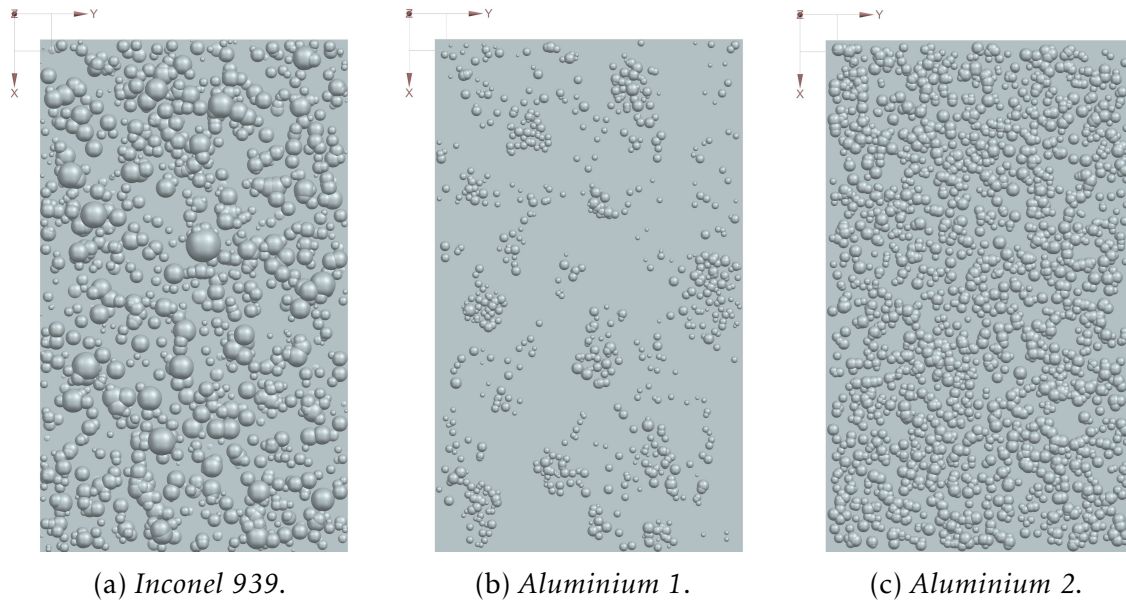
Figure 3.5: CAD design of the up-scaled prototype plates with AM-induced surface roughness.

The rough surface is generated using a custom macro implemented in *Siemens NX*. The script takes as input the calculated sphere density, the diameter distribution, and an offset distribution to place spherical roughness elements on the surface. While the first two distributions are derived from experimental data, the offset distribution requires further elaboration.

The offset is defined as the normalized vertical position of the sphere's center:

$$\text{off} = \frac{z}{D/2}$$

To recreate the height variability observed in real AM surfaces, the offset distribution is modeled as a normal probability density function (PDF). The x and y positions of each sphere are assigned based on a uniform random distribution.

A trial-and-error approach was adopted to tune the diameter and offset distributions until the resulting surface matched the desired surface roughness parameters. Initially, parameters such as S_a, S_q, and S_z were targeted. However, Brogliato [106] later proposed to match the skewness (S_{sk}) and kurtosis (S_{ku}) values. These higher-order parameters exhibited large deviations due to the limitations of the spherical modeling approach, which cannot replicate the more complex topographies of actual AM surfaces. Additionally, one significant feature of AM surfaces is the presence of *clusters*, i.e., groups of rough elements that create non-uniform distributions with large smooth areas between them. These clusters may have a strong influence on local heat transfer mechanisms.

Figure 3.5 shows the CAD renderings of the three analogue surfaces used in this study. These surfaces differ substantially in particle size, roughness amplitude and spatial density, particularly in the aluminium cases. The modelling approach aims not only to replicate the real surface morphology, but also to investigate how variations in surface roughness parameters affect local heat transfer.

Table 3.1 summarizes the surface roughness parameters of the real and analogue surfaces. Several limitations of the analogue modelling approach should be acknowledged:

- Stylus profilometry only provides 2D profiles along a single line, which may not capture the full 3D characteristics of the surface, despite multiple measurements.

- The model assumes all roughness elements are spherical, whereas real surfaces include a broader range of geometries such as ellipsoids and irregular particles.

- The AM surface roughness depends strongly on the printing parameters (e.g., orientation, speed), restricting the applicability of the analogue model to specific conditions.

To improve the fidelity of the analogue surface characterization, modifications were introduced to the surface roughness evaluation script, enabling the inclusion of additional statistical descriptors.

3.3 SRHT-rig Setup

The experiments conducted on the SRHT-rig aim at obtaining a spatially resolved distribution of the heat transfer coefficient (HTC). Achieving this requires a dedicated

	S_a [mm]	S_q [mm]	S_z [mm]	S_{sk}	S_{ku}	ES	λ_f	λ_p
Inconel 939	**d1.25 mm, 90° printing, $s = 77.4$**							
Real SR	1.077	1.325	5.689	0.46	2.79	-	-	-
Analogue SR	1.085	1.287	6.006	0.975	3.237	0.546	0.029	0.622
Percent Error	0.74%	2.87%	5.57%	112%	16%	-	-	-
Aluminium 1	**d1.5 mm, 90° printing, $s = 63.15$**							
Real SR	0.37	0.47	2.32	0.22	3.47	-	-	-
Analogue SR	0.321	0.467	2.692	2.345	7.378	0.193	0.013	0.165
Percent Error	31.2%	0.64%	16%	966%	113%	-	-	-
Aluminium 2	**d1.5 mm, 90° printing, $s = 63.15$**							
Real SR	0.37	0.47	2.32	0.22	3.47	-	-	-
Analogue SR	0.623	0.689	2.509	0.347	1.723	0.48	0.014	0.599
Percent Error	68.4%	46.6%	8.15%	57.7%	50.3%	-	-	-

Table 3.1: Comparison of surface roughness parameters between real and analogue surfaces

test rig configuration equipped with specific measurement devices, as outlined in this section.

3.3.1 Test Rig

Figure 3.6 presents a CAD rendering of the test rig, with the flow direction oriented from right to left.

The flow straightener is a $1\,m$-long rectangular duct made of aluminium, with a width of $150\,mm$ and a height of $97\,mm$. It is connected to an aluminium chamber with two outlets, one leading to a bypass and the other to the test section. A pneumatic actuator drives a shaft-mounted hatch that can selectively close off either the bypass or the test section inlet. The cross-section of the hatch is slightly larger than that of the test section, introducing a step of approximately $5\,mm$ at the transition. This step causes a disturbance in the boundary layer development.

The test section itself has a length of $1550\,mm$, a width of $100\,mm$, and a height of $90\,mm$, with a fillet radius of $5\,mm$ in the corners. It is composed of a top plate, two side plates, and a bottom plate.

The top plate contains several circular openings designed for infrared thermal imaging of the bottom plate during heating. For each test, one of these openings is covered with an IR-transparent window, while the others are sealed with lids. The window is manufactured from a high-transmissivity material optimized for IR measurements. The
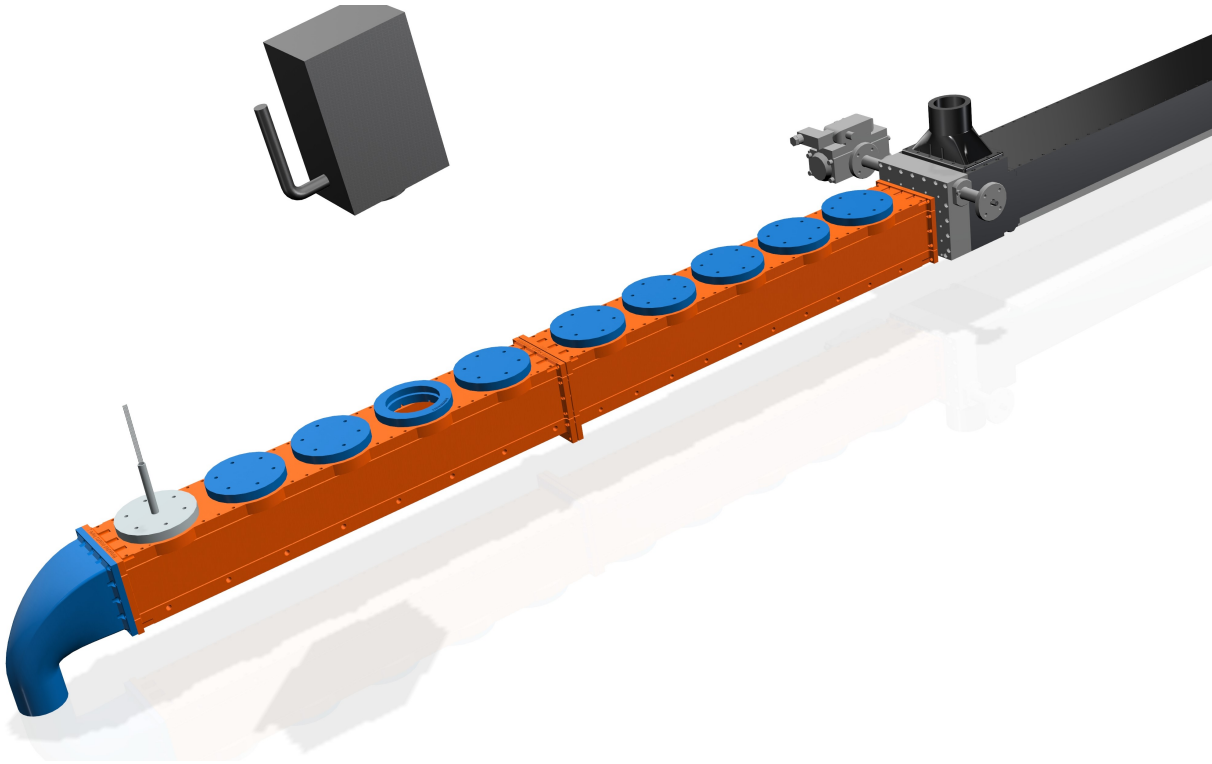
Figure 3.6: CAD model of the SRHT rig

infrared camera is mounted directly above the window to record surface temperature distributions.

The bottom plate serves as the mounting bed for the test samples, accommodating up to ten test plates.

Both the test section and the test plates are fabricated from *Accura Xtreme Grey* using stereolithography (SLA). The main thermal properties of this material are listed in Table 3.2. A key distinction is made between axial and radial properties: axial values refer to behavior through the layering direction, while radial values represent in-plane properties along the layers. A layer thickness of $0.1\,mm$ was selected to ensure a fine surface finish.

Sealing between the rig components is achieved using silicone gaskets or O-rings. To ensure high surface emissivity, all internal surfaces of the test channel are painted black.

$T\,[°C]$	$k_{\mathrm{ax}}\,[W/m\,K]$	$k_{\mathrm{rad}}\,[W/m\,K]$	$c_p\,[J/kg\,K]$
30	0.224	0.211	1442.4
50	0.227	0.237	1735.9

Table 3.2: *Accura Xtreme Grey* thermal properties in axial and radial directions

Property	Value
Flow straightener	
Length	$1000\,mm$
Width	$150\,mm$
Height	$97\,mm$
Test section	
Test bed length	$1550\,mm$
Test bed width	$100\,mm$
Test section height	$90\,mm$
Fillet radius	$5\,mm$
Test section cross-sectional area	$8980\,mm^2$
Test section hydraulic diameter	$96.7\,mm$
Number of test objects	10
Test object	
Length	$150\,mm$
Width	$90\,mm$
Height	$15\,mm$

Table 3.3: Geometric characteristics of the SRHT-rig

3.3.2 Heating System

To supply the thermal energy required for the experiments, an air heater is integrated into the rig. The system consists of a power supply connected to resistive elements that heat up the incoming air within the main duct. By adjusting the power input, it is possible to regulate and maintain a constant air temperature throughout the experiment.

All components needed for safe operation, including a thermal relay, power regulation system, and safety electronics, are housed within the dedicated heater controller unit.

3.3.3 IR Thermography

3.3.3.1 IR Camera

The transient surface temperature at the bottom of the test section, i.e., the wall temperature T_w, is recorded using an infrared (IR) camera. The model employed in this study is the *Titanium 560M* by *Cedip Infrared Systems*, which is specifically designed for academic and industrial R&D applications, offering high sensitivity, accuracy, spatial resolution, and acquisition speed at an affordable cost. The camera is operated using the *FLIR ResearchIR* software, which provides a user-friendly interface for data acquisition and parameter configuration. The technical specifications of the camera are listed in Table 3.4.

Property	Value
Titanium 560M	
Sensor Type	InSb
Waveband	$3 \div 5\,\mu m$ or $8 \div 12\,\mu m$
Pixel Resolution	640×512
Integration Time	$1200\,\mu s$
Frame Rate	$10\,Hz$
Calibration Temperature Range	$-15 \div 100\,°C$
Calibration Device	*DIAS CS110*

Table 3.4: Technical specifications of the IR camera

(a) *Titanium 560M*   (b) *DIAS CS110*
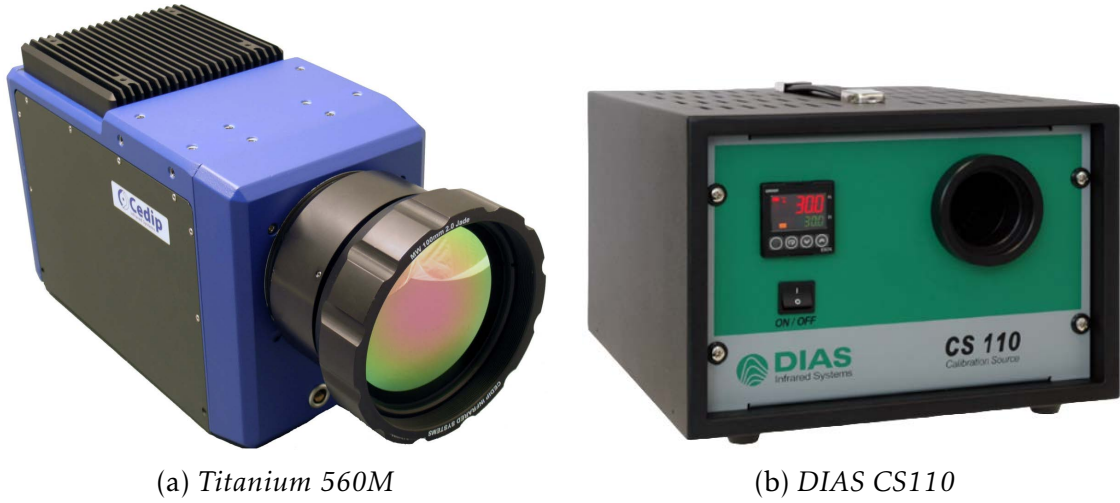
Figure 3.7: IR camera and calibration device

3.3.3.1.1   Calibration   The IR camera does not directly measure temperature but detects a radiometric signal that must be correlated to absolute temperature [61].

In the present work, an integration time of $1200\,\mu s$ was selected based on the expected surface temperature range of $23.3\,°C$ to $67.5\,°C$ ($296.45\,K$ to $340.65\,K$). A frame rate of $10\,Hz$ was conservatively chosen to adequately capture the transient thermal response.

To correlate the radiometric signal to actual temperatures, an IR calibration source (CS), also referred to as technical blackbody, was used. The calibration device employed was the *DIAS CS110* by *DIAS Infrared Systems*, shown in Fig. 3.7(b). This device features a known emissivity of $\varepsilon_{CS} = 0.98 \pm 0.01$ and a calibration temperature range of $-15\,°C$ to $110\,°C$ ($258.15\,K$ to $383.15\,K$), with an uncertainty of $\Delta T_{CS} = \pm 0.5\,K$ [46].

Calibration was performed over the range $5\,°C$ to $70\,°C$ ($278.15\,K$ to $343.15\,K$), in increments of $5\,K$. At each temperature step, the radiometric signal was recorded and

corrected for the calibrator's emissivity. The calibration points are plotted as blue circles in Fig. 3.7(b).

A curve-fitting approach is typically used in IR thermography to establish a continuous relationship between radiometric signals and absolute temperatures. In this work, the fitting function introduced by Liebmann [44] was applied, given in Eq. (3.2), where A, B, C, D, and T_0 are fitting parameters, S is the detected signal, and T is the corresponding blackbody temperature:

$$T = A \cdot S^{1/2} + B \cdot S^{3/2} + C \cdot S^2 + D \cdot \ln(S) + T_0 \tag{3.2}$$
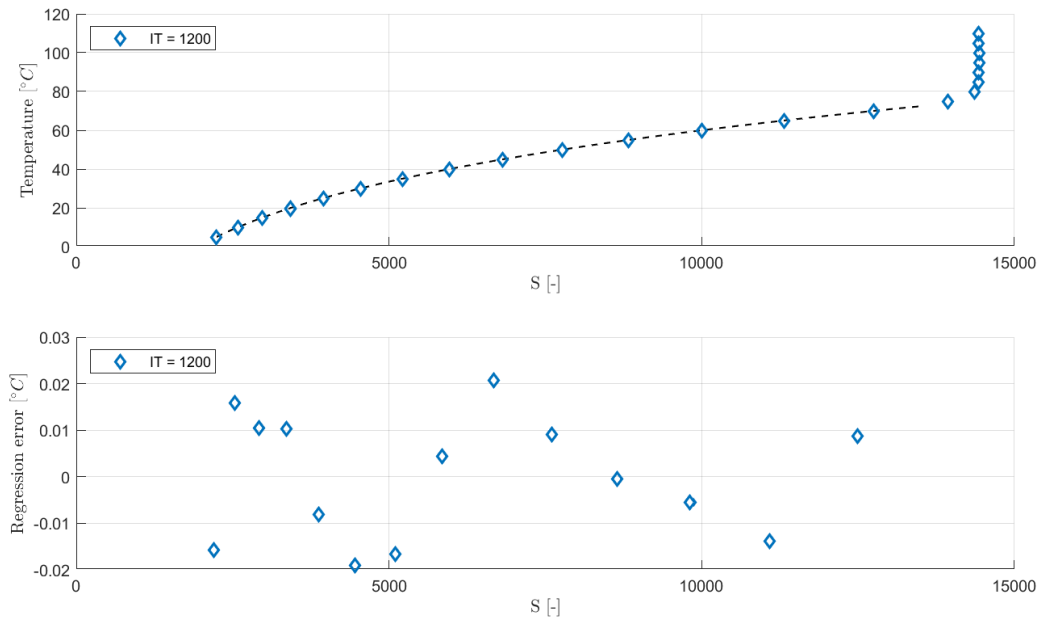
Figure 3.8: Camera calibration curve fitting for $IT = 1200\,\mu s$

Parameter	A	B	C	D	T_0
Value $[K]$	-0.2549	2.0853×10^{-5}	-8.3719×10^{-8}	38.578	-9.1824

Table 3.5: Curve-fitting parameters for IR camera calibration

The regression error remains within $0.03°C$ across the entire calibration range, which is well below the IR camera's intrinsic accuracy of $1°C$.

Hereafter, the transformation function from signal to temperature as defined by Eq. (3.2) is denoted as $F_{S \rightarrow T}$. For calibration routines and heat transfer experiments, it was also necessary to determine the inverse function, converting temperature T to signal S. Since Eq. (3.2) is not analytically invertible, a numerical interpolation was performed using `interp1` in *MATLAB*. This inverse function is referred to as $F_{T \rightarrow S}$.

3.3.3.2 IR Window

The IR window used in the SRHT-rig is the *IRW-4C* by *FLIR*, made of high-transmissivity calcium fluoride, which is suitable for short-, mid-, and long-wave IR imaging. The optical diameter of the window is $95\,mm$, with a thickness of $29.15\,mm$. The transmissivity τ_{IRW} and reflectivity ρ_{IRW} were not initially known and were experimentally determined by Lehmann [103]. The resulting values are reported in Table 3.6.

3.3.3.3 IR Paint

A critical factor influencing the accuracy of quantitative IR measurements is the surface emissivity of the target object. The closer this emissivity is to that of an ideal blackbody, the higher the measurement accuracy [55]. To ensure uniform and high-emissivity conditions, the bottom plate and the remaining inner surfaces of the test section were coated with a thin layer of high-emissivity black paint. The paint used was a commercially available product by *Senotherm*, whose emissivity properties were not known a priori. Lehmann [103] conducted a dedicated calibration to determine its characteristics. The calibrated values are provided in Table 3.6.

	Emissivity ε	Reflectivity ρ	Transmissivity τ
IR window	–	0.9489 ± 0.0334	0.0501 ± 0.0068
Paint	0.9072 ± 0.0274	0.0540 ± 0.0062	–

Table 3.6: Optical properties of IR window and paint [103]

3.3.4 Hot-Wire Anemometry

Hot-Wire Anemometry (HWA) was employed for the characterization of the velocity field in the SRHT-rig. This technique is well-suited for high-frequency, single-point velocity measurements in turbulent flows, offering excellent temporal resolution. The measurements were conducted using a single-wire probe by *Dantec Dynamics*, connected to a constant-temperature anemometer (CTA) system.

The working principle of HWA is based on the convective cooling of a thin, electrically heated wire exposed to the flow. As the flow velocity increases, the heat loss from the wire rises, requiring more electrical power to maintain its constant temperature. The electrical signal required to sustain this thermal equilibrium is then correlated to the local flow velocity.

3.3.4.1 Probe Calibration

Prior to measurements, the hot-wire probe was calibrated in a dedicated low-turbulence jet calibration unit. The velocity reference was obtained via a pitot-static tube coupled with a high-precision differential pressure transducer [38]. The calibration was performed at ambient temperature with the same flow medium (air) and under similar atmospheric conditions to those expected during the SRHT-rig validation.

The calibration process involved exposing the probe to a series of known free-stream velocities ranging from $u = 1.5$ to $u = 12\,m/s$ and recording the corresponding CTA bridge voltages. A second-order King's Law relationship was firstly used to fit the calibration data:

$$E^2 = A + B \cdot U^n \tag{3.3}$$

where E is the measured CTA voltage, U is the flow velocity, and A, B, and n are calibration coefficients obtained via nonlinear curve fitting.

The calibration curve fitting showed good agreement (with $R^2 > 0.92$). However, polynomial laws can be introduced to improve the fitting results. Despite not having a physical derivation, these laws show a better agreement during the calibration process. A third and fourth order polynomial laws were employed in the following form:

$$U = a + bE + cE^2 + dE^3$$
$$U = a + bE + cE^2 + dE^3 + eE^4$$

As shown in Fig. 3.9, the fourth order polynomial law appears to have a higher agreement (with $R^2 > 0.99$) compared to the third order one, thus confirming the reliability of the probe within the calibrated velocity range.
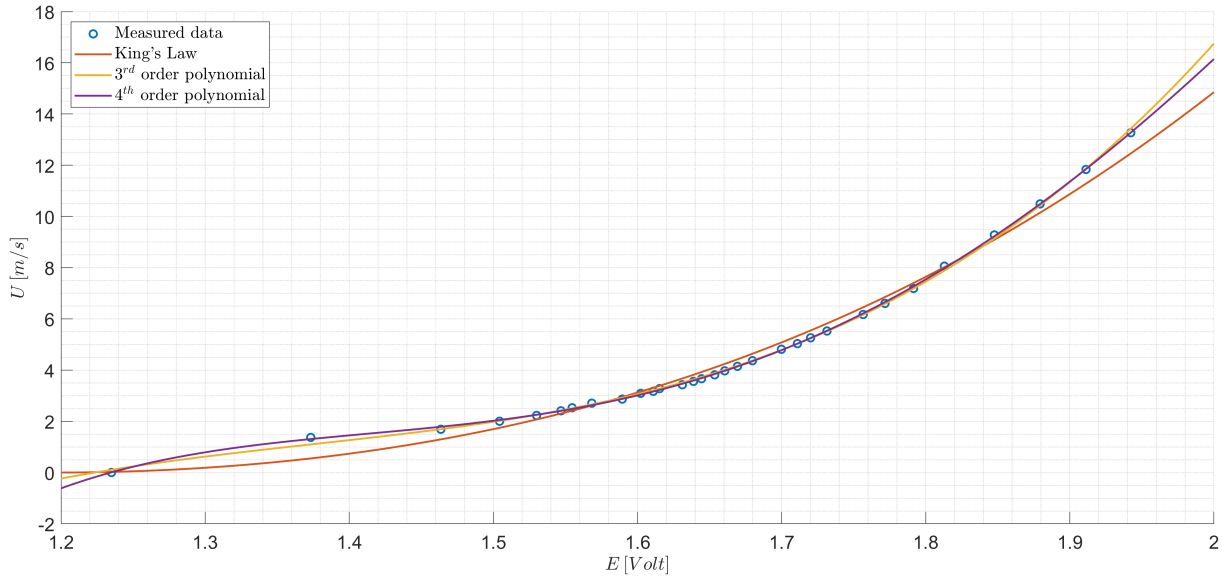
Figure 3.9: Hot-Wire calibration curves using thorough different fitting models

It is important to note that the accuracy of the hot-wire measurements depends not only on the calibration procedure but also on the correct alignment of the probe with the flow direction, thermal drift compensation, and signal filtering to minimize electronic noise. All these factors were carefully managed during the acquisition phase.

Parameter	a	b	c	d	e	R^2
	3rd order polynomial
Value [$Volt$]	-132.2	278.4	-198	48.02	-	0.9993
	4th order polynomial
	-516.4	1263	-1163	442.2	-61.64	0.9998

Table 3.7: Curve-fitting parameters for Hot-Wire polynomial laws calibration

3.3.5 Data Acquisition Systems

The Data Acquisition System (DAS) used in this study consists of sensors for measuring physical quantities, signal conditioning units for amplifying and filtering the signals, and analog-to-digital converters for digitizing the data. A laptop equipped with a custom-built software, *RigView*, developed in NI LabVIEW, is used to acquire, store, and visualize the data in real time.

Two primary devices are utilized for signal acquisition: the *Netscanner 9116* and the *Keysight Agilent 34972A*. The *Netscanner 9116* is a 16-channel piezoresistive pressure transducer featuring a full-scale accuracy of ±0.05% FS and a pressure measurement range from $-100\,psi$ to $100\,psi$. The *Keysight Agilent 34972A* data logger is employed to monitor various signals including temperature readings, mass flow rate, and absolute ambient pressure. The absolute pressure is measured using a *Rosemount 2088* absolute and gauge pressure transmitter.

Both the *Netscanner 9116* and the *Keysight Agilent 34972A* are connected to the host computer via the TCP/IP protocol, ensuring robust communication and high data throughput.

Each measurement device undergoes annual calibration to maintain measurement accuracy and verify proper operational performance.

3.3.5.1 Temperature Probes

Temperature measurement in the test rig is based on the principle that the electrical resistance of certain materials varies with temperature. By quantifying this resistance change relative to a known reference, accurate temperature measurements can be achieved. Two types of thermal sensors were used:

- *PT100:* This sensor is based on a platinum resistance element, with a nominal resistance of $100\,\Omega$ at $0°C$. PT100 sensors are known for their high accuracy, stability, and linearity over a wide temperature range.

- *Type-K Thermocouple:* Thermocouples are less expensive than PT100 sensors, respond faster to temperature changes, and can operate over a broader temperature range. In this setup, Type-K thermocouples were used to monitor the temperature of the copper bars due to their compact format, which allows easy integration. These thermocouples consist of two dissimilar metals: the positive

leg is made of a nickel-chromium (NiCr) alloy, while the negative leg is composed of a nickel-aluminium (NiAl) alloy. The junction of these metals forms the temperature-sensitive element. Calibration is required prior to use to ensure measurement accuracy.

3.4 Raw-Data Acquisition

To fully understand the methodology behind the experiments, it is essential to clarify both the nature of the acquired data and the procedure adopted for data acquisition. Although the post-processing differs between smooth and rough surface test cases, the types of data collected remain consistent across all experiments.

In this study, experiments were conducted at four distinct Reynolds numbers: $Re = 10000, 15000, 20000$, and 25000. As shown in Eq. (3.1), and given that both the hydraulic diameter D_h and the cross-sectional area A of the test section are constant (see Table 3.3), the Reynolds number is determined by the mass flow $\dot{m}$ and the air viscosity μ, which in turn depends on the air temperature T_∞. The viscosity is evaluated using Sutherland's law, based on the measured air temperature and the air mass flow rate $\dot{m}$. The latter is regulated via a control valve and measured using an orifice meter.

	$Re = 10000$	$Re = 15000$	$Re = 20000$	$Re = 25000$
$\dot{m}\ [g/s]$	19	28.5	38	47.5
$T_\infty\ [°C]/[K]$	70 / 343.15	70 / 343.15	70 / 343.15	70 / 343.15
Measurement duration t	$110\,s$	$110\,s$	$110\,s$	$110\,s$
Sampling frequency f_s	$10\,Hz$	$10\,Hz$	$10\,Hz$	$10\,Hz$

Table 3.8: Experimental flow conditions

To ensure the accuracy of the measurements, the hatch is only opened once thermal stabilization has been achieved in the flow straightener. Stabilization is defined as a temperature variation below $1°C/min$.

For the calculation of the local heat transfer coefficient (HTC), two main temperature data sets are required: the wall temperature distribution along the plate, and the bulk air temperature in the flow channel. The wall temperatures are indirectly measured using the IR camera, which records a video of the heated surface through the IR-transparent window. This video provides the temporal evolution of the radiometric signal at each pixel, which is then converted into surface temperature using the calibrated function in Eq. (3.2).

The bulk air temperature T_∞ is measured using three type-K thermocouples positioned at the center of the channel cross-section in the inlet, mid-section, and outlet. These three values are linearly interpolated along the streamwise direction, under the assumption of a quasi-linear thermal gradient along the duct.

(a) Captured frame　　　　　　　　(b) ROI mask
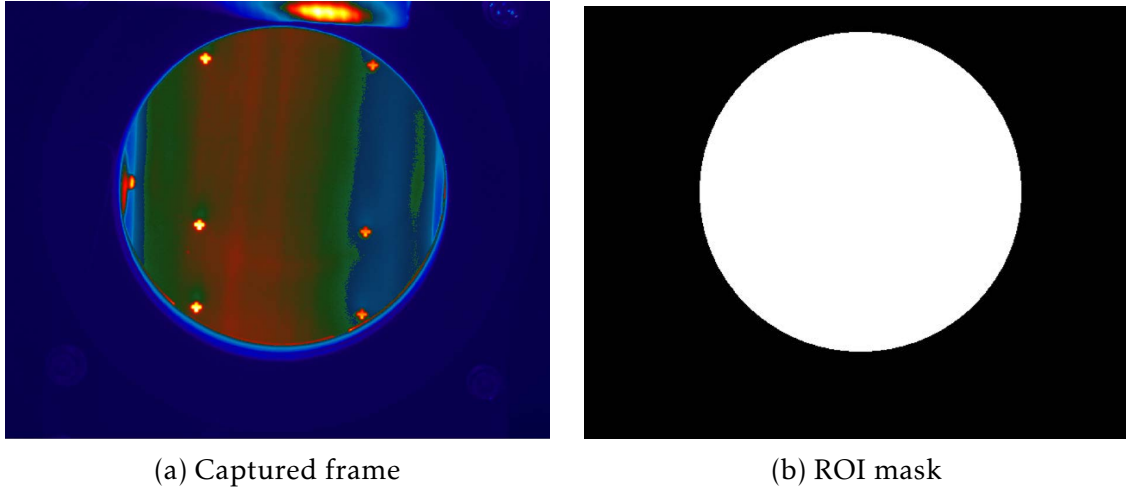
Figure 3.10: ROI selection example

3.5 Data Processing

A thorough post-processing methodology is required to accurately determine the convective heat transfer coefficient (HTC) from raw experimental data. This section outlines the approaches adopted for both smooth and rough test plates. While the specific solvers differ (1D for smooth plates and 3D for rough plates) the underlying principle remains consistent: the spatial distribution of the wall temperature T_w is obtained from transient experiments and used to extract the HTC. Since the Nusselt number Nu can only be indirectly calculated from wall conduction, the following relation is used:

$$Nu = \frac{hD_h}{k_{\mathrm{air}}}$$

where $k_{\mathrm{air}} = 0.029\,[W/(m \cdot K)]$ is the thermal conductivity of air.

3.5.1 IR-Video Processing

The infrared data acquired during the tests were recorded using *FLIR's ResearchIR* software, which stores video files in the .PTW format. The first step in post-processing involves identifying the experiment's starting frame. This is achieved by synchronizing the activation of a light source, placed adjacent to the infrared window, with the trigger signal of the pneumatic actuator. The illumination flash marks the exact initiation of the heating phase in the recorded IR video.

Subsequently, a Region of Interest (ROI) is defined. Each IR frame, with a resolution of 640×512 pixels, captures a large portion of the test section's lower plate. However, only a specific portion is relevant for accurate HTC analysis. An elliptical ROI is manually selected within each frame, as illustrated in Fig. 3.10(a), and exported as a binary mask (Fig. 3.10(b)). The radiometric signal within the ROI is then converted into wall temperature data using the camera-specific calibration function $F_{S \to T}$.

The raw IR signal S_{det} recorded by the camera is a superposition of signals originating from multiple sources [87]. A schematic representation is provided in Fig. 3.11, illustrating the various infrared contributions through the IR window (IRW) from the bottom plate and surrounding environment.
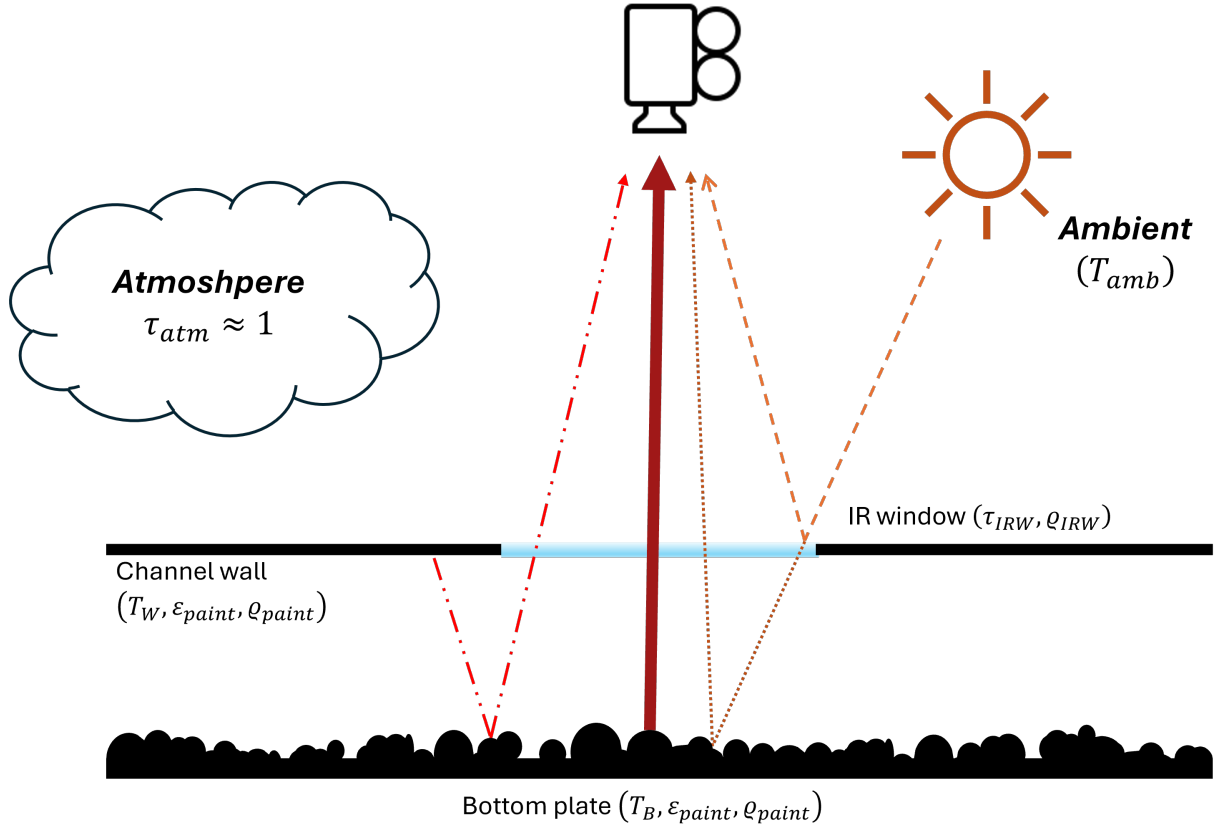
Figure 3.11: Components of the detected IR signal for this test cases

For this configuration, the detected signal can be expressed as:

$$S_{\text{det}} = \underbrace{\varepsilon_{\text{paint}} \tau_{\text{IRW}} S_B}_{\text{(a) Plate emission}} + \underbrace{\tau_{\text{IRW}}^2 \varrho_{\text{paint}} S_{\text{amb}}}_{\text{(b) Ambient reflected by plate}}$$

$$+ \underbrace{\varrho_{\text{IRW}} S_{\text{amb}}}_{\text{(c) Ambient reflected by window}} + \underbrace{\varepsilon_{\text{paint}} \varrho_{\text{paint}} \tau_{\text{IRW}} S_w}_{\text{(d) Wall emission reflected by plate}} \qquad (3.4)$$

Here S_B is the signal emitted by a blackbody at the same temperature as the bottom plate, S_w is the signal from the internal wall of the channel, S_{amb} is the signal from the ambient surroundings.

The first term corresponds to direct IR radiation from the painted bottom surface transmitted through the IR window. The second and third terms are ambient radiation components reflected either by the paint or the window (considering the ambient

with $\tau_{\mathrm{amb}} = 1$ since the distance is small [62]). The last term accounts for IR radiation emitted by the inner sidewalls and reflected by the painted surface before reaching the camera. The ambient temperature T_{amb} is measured directly within the test chamber. However, T_w, the channel wall temperature, cannot be directly measured due to camera occlusion and the impracticality of thermocouple integration. Therefore, a representative point on the IR image, which is typically a flat, undisturbed area, is used to approximate T_w.

From this representative flat region, assuming $S_B = S_w$, it is possible to rearrange Eq. (3.4) to extract S_w:

$$S_w = \frac{S_{\mathrm{det,flat}} - \left(\rho_{\mathrm{IRW}} + \rho_{\mathrm{paint}}\tau_{\mathrm{IRW}}^2\right)S_{\mathrm{amb}}}{\varepsilon_{\mathrm{paint}}\tau_{\mathrm{IRW}}\left(1 + \rho_{\mathrm{paint}}\right)}$$

Once S_w is known, the corrected blackbody signal S_B at each pixel in the ROI can be evaluated as:

$$S_B = \frac{S_{\mathrm{det}} - \left(\rho_{\mathrm{IRW}} + \rho_{\mathrm{paint}}\tau_{\mathrm{IRW}}^2\right)S_{\mathrm{amb}} - \varepsilon_{\mathrm{paint}}\rho_{\mathrm{paint}}\tau_{\mathrm{IRW}}S_w}{\varepsilon_{\mathrm{paint}}\tau_{\mathrm{IRW}}}$$

This final corrected signal S_B is then converted to surface temperature using the inverse calibration function $F_{S \to T}$. This processing ensures that the spatial distribution of T_w used for HTC calculations is physically consistent and accounts for all significant IR signal perturbations.

3.5.2   Mapping

As discussed in Section 3.5.1, the IR camera detects radiation from multiple sources. One potential artifact not explicitly addressed earlier is the reflection of the IR camera itself in the window. This is mitigated by slightly tilting the camera, thereby avoiding perpendicular alignment with the IR window and the bottom plate. However, this tilt introduces a geometric distortion in the captured images, making a mapping process necessary. Additionally, mapping is required to associate each pixel with a global coordinate system for quantitative analysis.

3.5.2.1   Smooth

For smooth plates, a set of four reference points is used to compute a Four-Points Transformation. To correlate the pixel coordinates to a natural coordinate system, as shown in Fig. 3.12(a), a coordinate transformation is performed based on the theory of isoparametric quadrilateral elements, a common approach in finite element analysis.

In the physical coordinate system (Fig. 3.12(b)), the χ' and ψ' axes denote the pixel column and row indices, respectively. The coordinates of the four reference points $\left(\chi_1', \psi_1'\right)$ to $\left(\chi_4', \psi_4'\right)$ are determined using *FLIR ResearchIR*.

(a) Natural coordinate system (b) Physical coordinate system
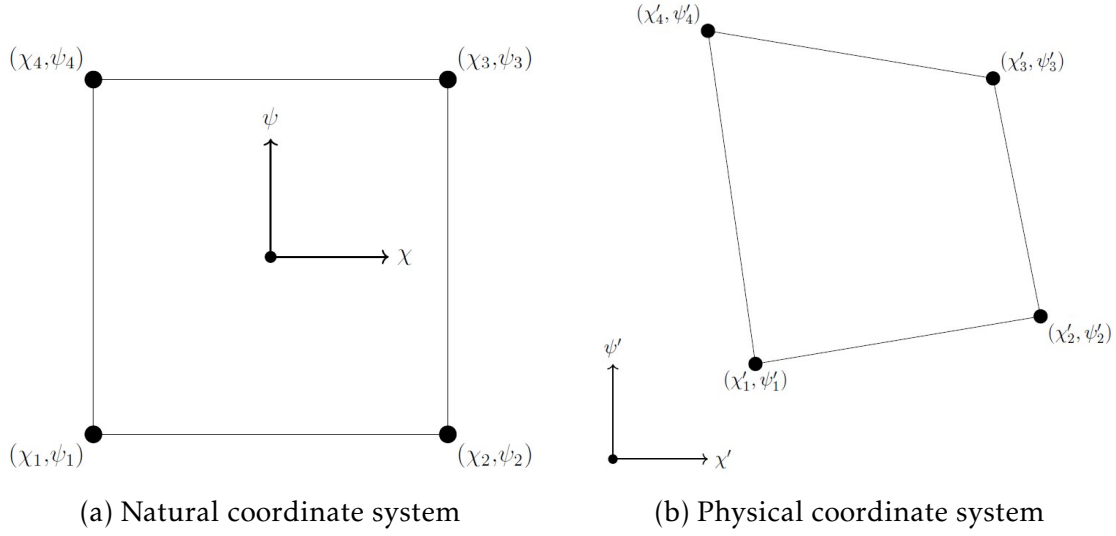
Figure 3.12: Four-Points-Transformation coordinate systems

A mesh is then created for the natural coordinate system shown in Fig. 3.12(a). For each reference point, a shape function (Eq. (3.5)) is defined. These functions N_1 to N_4 are constructed to return a value of 1 at the associated reference point and 0 at the others.

$$
\begin{aligned}
N_1 &= \frac{(\chi - \chi_2)(\psi - \psi_4)}{(\chi_1 - \chi_2)(\psi_1 - \psi_4)} & N_2 &= \frac{(\chi - \chi_1)(\psi - \psi_3)}{(\chi_2 - \chi_1)(\psi_2 - \psi_3)} \\
N_3 &= \frac{(\chi - \chi_4)(\psi - \psi_2)}{(\chi_3 - \chi_4)(\psi_3 - \psi_4)} & N_4 &= \frac{(\chi - \chi_3)(\psi - \psi_1)}{(\chi_4 - \chi_3)(\psi_4 - \psi_1)}
\end{aligned}
\tag{3.5}
$$

The coordinate transformation is carried out via the matrix relation in Eq. (3.6). By inserting an arbitrary point (χ, ψ) from the natural coordinate system into the shape function matrix, and multiplying it by the known physical coordinates of the reference points, the corresponding location in the physical (pixel) space is obtained. This allows the IR-detected temperature field to be projected into the desired coordinate system for analysis.

$$
\begin{bmatrix} \chi' \\ \psi' \end{bmatrix} = \begin{bmatrix} N_1 & 0 & N_2 & 0 & N_3 & 0 & N_4 & 0 \\ 0 & N_1 & 0 & N_2 & 0 & N_3 & 0 & N_4 \end{bmatrix} \begin{bmatrix} \chi'_1 \\ \psi'_1 \\ \chi'_2 \\ \psi'_2 \\ \chi'_3 \\ \psi'_3 \\ \chi'_4 \\ \psi'_4 \end{bmatrix}
\tag{3.6}
$$

3.5.2.2 Rough

For the rough surfaces, a tetrahedral mesh is generated from the CAD model described in Section 3.2, using *Siemens NX*. To ensure accurate geometric representation, the element size on the rough surface is constrained to be less than $1.5\,mm$, with smaller sizes (down to $0.04\,mm$) automatically applied in regions containing finer features, such as spherical protrusions.

The IR-to-mesh mapping process requires understanding how the IR camera projects 3D geometry onto a 2D image plane. A projection matrix P defines this transformation:

$$\begin{bmatrix} u \\ v \\ 1 \end{bmatrix} = \begin{bmatrix} p_{11} & p_{12} & p_{13} & p_{14} \\ p_{21} & p_{22} & p_{23} & p_{24} \\ p_{31} & p_{32} & p_{33} & p_{34} \end{bmatrix} \begin{bmatrix} X \\ Y \\ Z \\ 1 \end{bmatrix}$$

where (u, v) are the image coordinates and (X, Y, Z) are the 3D world coordinates. The matrix $P = K[R\,t]$ combines K, the intrinsic calibration matrix containing focal length and lens distortion, R is the rotation matrix (world-to-camera) and t is the translation vector.

To estimate P, the matrix is rewritten as a vector p:

$$p = \begin{bmatrix} p_{11} & p_{12} & p_{13} & p_{14} & p_{21} & p_{22} & p_{23} & p_{24} & p_{31} & p_{32} & p_{33} & p_{34} \end{bmatrix}^T$$

Each 3D-to-2D point correspondence provides two equations. At least six non-coplanar points are required to solve for the twelve unknowns in p, although additional points are used to improve accuracy. These points are selected manually from the CAD model and matched to identifiable features in the IR image.

$$\begin{bmatrix} X_1 & Y_1 & Z_1 & 1 & 0 & 0 & 0 & 0 & -u_1 X_1 & -u_1 Y_1 & -u_1 Z_1 & -u_1 \\ 0 & 0 & 0 & 0 & X_1 & Y_1 & Z_1 & 1 & -v_1 X_1 & -v_1 Y_1 & -v_1 Z_1 & -v_1 \end{bmatrix} p = \begin{bmatrix} 0 \\ 0 \end{bmatrix}$$

One of the mapping results is presented in Fig. 3.13. The blue dots represent mesh points within the IR camera's ROI; blue circles are original image coordinates from the IR view, while black asterisks are the calculated projections using the derived matrix P. The visual alignment confirms the accuracy of the transformation.

The final mapped temperature field is interpolated onto mesh nodes within the ROI. However, occlusions (e.g. overhanging features) can lead to erroneous temperature values due to IR signal shadowing. For this reason, regions near sphere-plate intersections, where mapping uncertainties are high, are excluded from further analysis.

Moreover, mesh refinement is critical. In regions with steep thermal gradients (e.g. upstream-facing surfaces of spheres) an insufficiently refined mesh may misrepresent temperature fields by mapping smooth-region values onto rough features. Such errors are particularly critical because the temperature on sphere surfaces is typically

(a) One IR camera image

(b) Temperature mapping results
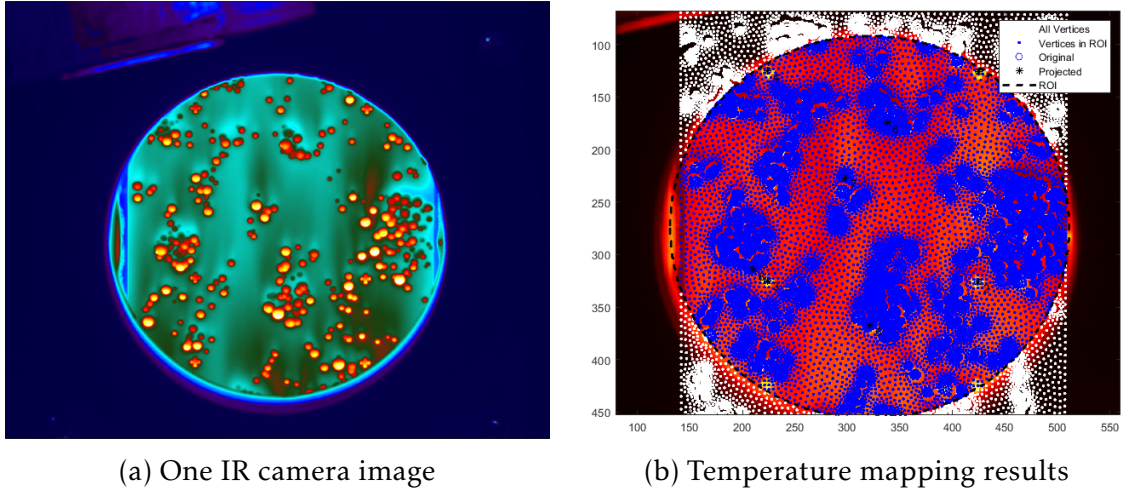
Figure 3.13: IR image and temperature mapping

higher due to direct hot airflow impingement. A denser mesh in these areas minimizes mapping errors and ensures accurate HTC reconstruction.

3.5.3 Underlying Equations

3.5.3.1 Smooth

The local heat transfer coefficient (HTC) on the smooth plates, positioned at the bottom of the channel, is evaluated as a classic case of transient conduction. The governing equation in three-dimensional Cartesian coordinates is:

$$\frac{\partial^2 T}{\partial x^2} + \frac{\partial^2 T}{\partial y^2} + \frac{\partial^2 T}{\partial z^2} + \frac{q}{k} = \frac{1}{\alpha}\frac{\partial T}{\partial t} \tag{3.7}$$

For one-dimensional heat conduction, in the absence of internal heat generation and under the assumption of constant thermal conductivity, Eq. (3.7) simplifies to:

$$\frac{\partial^2 T}{\partial z^2} = \frac{1}{\alpha}\frac{\partial T}{\partial t} \tag{3.8}$$

This formulation applies to the case of a semi-infinite solid, a geometry in which the body extends infinitely in all directions except one, and an instantaneous surface temperature change initiates one-dimensional transient conduction. Such an idealization provides a good approximation of the step response of finite solids, such as plates, when the temperature perturbation has not yet reached the back face of the material.

In this study, the z-axis is defined as the coordinate normal to the plate surface and orthogonal to the flow direction x. The air temperature in the main flow is denoted as

84

T_∞. Eq. (3.8) is a second-order partial differential equation in space and first-order in time, and requires an initial condition and two boundary conditions.

The initial temperature distribution is assumed uniform across the depth of the plate:

$$T(z, t = 0) = T_i$$

The first boundary condition at the surface ($z = 0$) is obtained by combining Fourier's law with Newton's law of cooling, for a step change in fluid temperature ($T_\infty \neq T_i$):

$$-k\frac{\partial T}{\partial z}\bigg|_{z=0} = h\left[T(0, t) - T_\infty\right]$$

The second boundary condition applies at an infinite depth, where the temperature remains at its initial value:

$$T(z \rightarrow \infty, t) = T_i$$

An analytical solution to this problem is given by:

$$\frac{T(z, t) - T_i}{T_\infty - T_i} = \text{erfc}\left(\frac{z}{2\sqrt{\alpha t}}\right) - \exp\left(\frac{hz}{k} + \frac{h^2 \alpha t}{k^2}\right) \cdot \text{erfc}\left(\frac{z}{2\sqrt{\alpha t}} + \frac{h\sqrt{\alpha t}}{k}\right) \qquad (3.9)$$

where $\alpha = \frac{k}{\rho c_p}$ is the thermal diffusivity, h is the heat transfer coefficient (HTC), the unknown to be determined, k is the thermal conductivity of the plate material, $T(z, t)$ is the wall temperature T_w measured by the IR camera, $\text{erfc}(W) = 1 - \text{erf}(W)$ is the complementary error function.

This expression allows the computation of the local HTC at each pixel by solving the equation iteratively using a non-linear solver. The spatial resolution of the temperature field is limited by the resolution of the IR camera.

It is important to highlight that the assumption of a semi-infinite domain is valid only while the thermal wave has not penetrated the entire thickness δ of the plate. The duration of the transient must satisfy:

$$t_{\max} < \frac{\delta^2}{16\alpha} \approx 120\,\text{s}$$

This is based on the plate thickness $\delta = 15\,\text{mm}$ and the worst-case thermal diffusivity of Xtreme Accura Grey material, $\alpha = 1.43 \times 10^{-7}\,\text{m}^2/\text{s}$.

Eq. (3.9) forms the core of the 1D conduction solver, applied within the selected ROI to extract the HTC field. This formulation assumes an ideal instantaneous step change in T_∞, which does not fully reflect physical reality. In practice, a delay is present

due to the finite time required for the heated air to fill the duct volume. This issue is corrected using an approach introduced by Metzger & Larson [27], based on Duhamel's superposition theorem.

In this method, the time-varying T_∞ is approximated as a series of discrete step changes $\Delta T_{\infty(j,j-1)}$, and the wall temperature is expressed as:

$$T_w - T_i = \sum_{j=1}^{N} U(t - \tau_j) \Delta T_{\infty(j,j-1)}$$

with the unit step response function $U(t - \tau_j)$ given by:

$$U(t - \tau_j) = 1 - \exp\left(\frac{h^2}{k^2}\alpha(t - \tau_j)\right) \cdot \mathrm{erfc}\left(\frac{h}{k}\sqrt{\alpha(t - \tau_j)}\right)$$

Combining the above expressions yields the final form used to compute the HTC, accounting for the actual time evolution of T_∞:

$$T_w - T_i = \sum_{j=1}^{N} \left[1 - \exp\left(\frac{h^2}{k^2}\alpha(t - \tau_j)\right) \cdot \mathrm{erfc}\left(\frac{h}{k}\sqrt{\alpha(t - \tau_j)}\right)\right] \Delta T_{\infty(j,j-1)}$$

The main flow temperature curve $T_\infty(t)$ is thus approximated by a finite number of discrete steps. These are defined by two criteria:

1. A new step is defined whenever the temperature changes by more than 8% of the total range, ensuring high resolution during the steep initial ramp.

2. A step is also enforced every 25 s to capture slow changes later in the test.

An overdetermined system results for each pixel, since multiple T_w measurements are available over time. The HTC is then extracted via curve-fitting using the `fsolve` function in *MATLAB*, which numerically solves nonlinear systems of the form:

$$\mathbf{F}(\mathbf{x}) = 0$$

This non-linear fitting procedure is executed independently for each pixel in the ROI, yielding a full-field map of the local HTC over the smooth plate.

(a) Typical main flow temperature response during a transient test

(b) Time evolution of the wall temperature at one pixel. The fitted curve achieves $R^2 = 0.99$
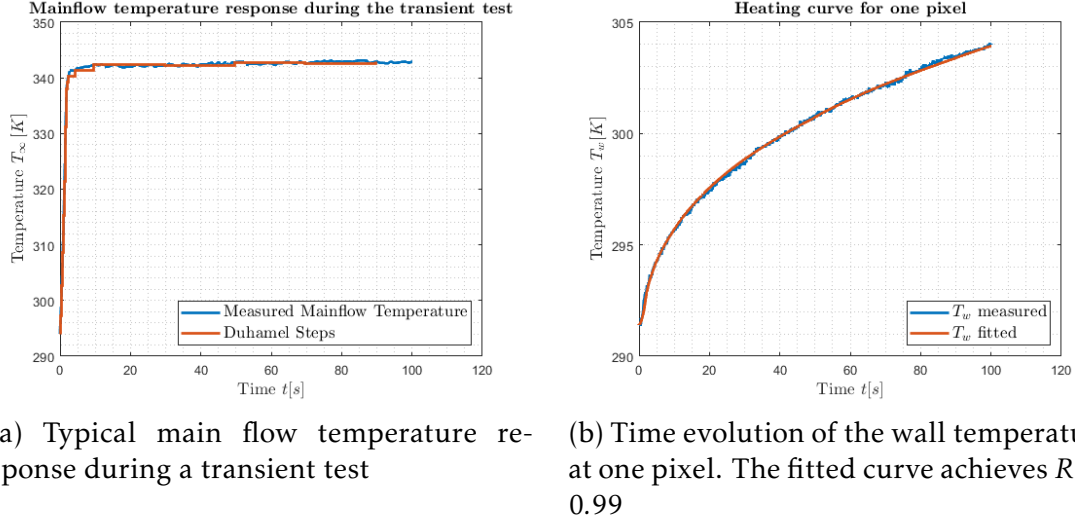
Figure 3.14: 1D solver implementation for the smooth plate

3.5.3.2 Rough

For the rough plates investigated in this study, characterized by spherical structures distributed across the surface, the one-dimensional heat conduction model is no longer sufficient to describe the true nature of the heat transfer. Therefore, a fully three-dimensional approach is required to obtain physically meaningful results. The heat transfer coefficient (HTC) on the rough surface is computed through an inverse procedure that involves solving both a direct and an adjoint problem. This process is implemented in an internal proprietary software named *C3D*.

Once the IR camera data are mapped onto the nodes of a 3D computational mesh, the HTC distribution is adjusted iteratively so that the computed nodal temperature profiles match the measured temperature data. This constitutes an inverse heat transfer problem, in which the unknown HTC is inferred from surface temperature measurements. The objective is to minimize the difference between the measured and the simulated wall temperature by optimizing the local HTC distribution. This requires the solution of a transient direct heat conduction problem and its corresponding adjoint formulation, as described in Jaksch [67].

The governing equations for the direct problem are:

$$\begin{cases} \rho c \dfrac{\partial T}{\partial t} = \nabla \cdot (k \nabla T) & \text{in } \Omega, \quad 0 \le t \le t_f \\[2ex] k \dfrac{\partial T}{\partial \vec{n}} = h\left(T - T_g\right) & \text{on } \Gamma, \quad 0 \le t \le t_f \\[2ex] T(x, t = 0) = T_0(x) & \text{in } \Omega \end{cases} \tag{3.10}$$

Here, $k(x, T)$ is the thermal conductivity, $\rho(x, T)$ is the density, $c(x, T)$ is the specific heat capacity, $h(x, T)$ is the heat transfer coefficient to be optimized, $T_g(x, T)$ is the bulk

gas temperature (commonly denoted T_∞ in the smooth case), $\vec{n}$ is the outward-pointing normal vector at the boundary Γ, and Ω denotes the domain of the solid.

The goal is to determine the spatial distribution of $h(x)$ such that the objective function J, quantifying the deviation between simulated and measured wall temperatures, is minimized:

$$J = \frac{1}{2} \int_0^{t_f} \int_\Gamma \left(T(x,t) - T_m(x,t)\right)^2 d\Gamma \, dt \tag{3.11}$$

In Eq. (3.11), $T_m(x,t)$ represents the wall temperature measured by the IR camera. As the Reynolds and Prandtl numbers are assumed constant during the experiment, the Nusselt number, and hence the HTC, is considered time-independent:

$$Nu \neq f(t)$$

To solve the inverse problem, a Lagrangian function $\mathcal{L}(h, \lambda)$ is constructed, incorporating the constraint imposed by the heat conduction PDE via the adjoint variable $\lambda(x,t)$:

$$\mathcal{L}(h, \lambda) = J + \int_0^{t_f} \int_\Omega \lambda(x,t) \left(\rho c \frac{\partial T}{\partial t} - \nabla \cdot (k \nabla T)\right) d\Omega \, dt \tag{3.12}$$

Even though h does not appear explicitly in Eq. (3.12), any variation δh affects T, and consequently $\mathcal{L}$. To locate stationary points of $\mathcal{L}$, the gradients $\partial \mathcal{L}/\partial h$ and $\partial \mathcal{L}/\partial \lambda$ must be equal to zero. In numerical practice, the derivative with respect to h is approximated using finite differences:

$$\frac{\partial \mathcal{L}}{\partial h} \approx \frac{\mathcal{L}(h + \delta h) - \mathcal{L}(h)}{\delta h}$$

After algebraic manipulations, as detailed in [67], the variation $\delta \mathcal{L}_h$ becomes:

$$\begin{aligned}
\delta \mathcal{L}_h = &\int_0^{t_f} \int_\Omega \delta T \left(-\rho c \frac{\partial \lambda}{\partial t}\right) d\Omega \, dt \\
&+ \int_0^{t_f} \int_\Gamma \delta T \left(T - T_m + k \frac{\partial \lambda}{\partial \vec{n}} - h\lambda\right) d\Gamma \, dt \\
&+ \int_\Omega \lambda \rho c \, \delta T(t = t_f) \, d\Omega - \int_0^{t_f} \int_\Gamma \lambda \, \delta h \left(T - T_g\right) d\Gamma \, dt
\end{aligned}$$

To ensure that $\delta \mathcal{L}_h = 0$ for arbitrary δh, the adjoint variable $\lambda(x,t)$ must satisfy the following equations:

$$
\begin{cases}
-\rho c \dfrac{\partial \lambda}{\partial t} = \nabla \cdot (k \nabla \lambda) & \text{in } \Omega, \quad 0 \le t \le t_f \\[2mm]
k \dfrac{\partial \lambda}{\partial \vec{n}} = h\lambda - (T - T_m) & \text{on } \Gamma, \quad 0 \le t \le t_f \\[2mm]
\lambda(x, t_f) = 0 & \text{in } \Omega
\end{cases}
$$

With this, the variation of the Lagrangian becomes:

$$
\delta \mathcal{L}_h = \int_0^{t_f} \int_\Gamma -\lambda \, \delta h \left(T - T_g \right) d\Gamma \, dt \tag{3.13}
$$

Using the substitution $\tau = t_f - t$, the adjoint problem can be reformulated as:

$$
\begin{cases}
\rho c \dfrac{\partial \lambda}{\partial \tau} = \nabla \cdot (k \nabla \lambda) & \text{in } \Omega, \quad 0 \le \tau \le t_f \\[2mm]
k \dfrac{\partial \lambda}{\partial \vec{n}} = h\lambda - (T - T_m) & \text{on } \Gamma, \quad 0 \le \tau \le t_f \\[2mm]
\lambda(x, 0) = 0 & \text{in } \Omega
\end{cases} \tag{3.14}
$$

Equation (3.14) define the adjoint problem, which is structurally similar to the direct problem in Eq. (3.10). While solving $\delta \mathcal{L}_h$ leads to the adjoint problem, solving $\delta \mathcal{L}_h$ will lead back to the direct problem. To know how δh will cause the change in the target function J, it is necessary to find the sensitivity of J which is defined as the derivative of J with respect to h at a certain point x and time t denoted as J_h'. From Eq. (3.12) and the fact that T always satisfies the direct problem, it implies that $J_h' \equiv \mathcal{L}_h'$. And from Eq. (3.13), $\mathcal{L}_h'$ can be written as:

$$
\mathcal{L}_h' = -\lambda \left(T - T_g \right)
$$

The overall solution procedure can be summarized as follows:

1. Provide an initial guess for h and solve the direct problem to obtain the temperature field $T(x, t)$;

2. Using T and the measured temperature T_m as inputs, solve the adjoint problem to compute $\lambda(x, t)$;

3. Compute the sensitivity $J_h'(x, t)$ from λ and T;

4. Apply a gradient-based optimization method to update $h(x)$ and reduce J;

5. Repeat the process until convergence is achieved (i.e., when residuals fall below a predefined tolerance).

This inverse optimization loop is executed for six specific time instances:

$$t = 0, 10, 20, 40, 70, 100\,\text{s}$$

The method is fully implemented in the in-house software *C3D* developed at Siemens Energy AB, as described in [67].

3.6 Uncertainty Analysis

In modern experimental research, results are incomplete without an uncertainty analysis, which provides an estimation of the reliability of the measured or computed quantities. It offers a quantified perspective on the possible error margins and lends credibility to the experimental conclusions. The overall uncertainty in an experimental campaign arises from multiple sources, including instrumentation, setup conditions, data acquisition, and post-processing techniques.

3.6.1 Introduction to Uncertainty Analysis

The uncertainty of a measurement is defined as:

"Parameter, associated with the result of a measurement, that characterizes the dispersion of the values that could reasonably be attributed to the measurand."

When measuring a physical quantity X, the true value X_{real} is inherently unknown. The act of measuring introduces disturbances or limitations, leading to measurement errors. As a result, only a best estimate X_{best} of the actual value can be provided, along with an associated uncertainty δ_X, which defines a confidence interval around the estimate:

$$X = X_{\text{best}} \pm \delta_X$$

Even when multiple measurements are performed, X_{real} generally remains unknown and differs from the average value:

$$X_{\text{real}} \neq X_{\text{best}}$$

For N repeated measurements X_i, the best estimate is usually given by the arithmetic mean:

$$X_{\text{best}} = \overline{X} = \frac{1}{N} \sum_{i=1}^{N} X_i$$

In the case of a single measurement, X_{best} corresponds to the measured value, and the uncertainty is dictated by the instrument's resolution and accuracy specifications.

Sources of uncertainty are commonly categorized into two main types:

- *Systematic errors:* These arise from inherent limitations in the measurement instruments or setup, introducing a consistent bias in the results. Reducing systematic errors typically requires improved instrumentation or calibration procedures.

- *Random errors:* These result from uncontrolled fluctuations in the experimental procedure, including human factors and environmental influences. Statistical analysis is used to quantify them, particularly when the sample size is large.

If a measured result Y is a function of several input quantities $X_1, X_2, \ldots, X_N$, each with its own uncertainty, the total uncertainty in Y must account for the propagation of uncertainties from all inputs:

$$Y = f(X_1, X_2, X_3, \ldots, X_N)$$

According to Coleman and Steele [71], two principal methods are used to evaluate uncertainty in experimental studies:

1. *Monte Carlo Method (MCM):* A stochastic approach that involves sampling from assumed probability distributions of input variables to obtain a statistical distribution of the output, from which uncertainty estimates can be drawn.

2. *Taylor Series Method (TSM):* A deterministic approach based on expanding the output function in a Taylor series and retaining first-order terms. The uncertainty is then derived using partial derivatives of Y with respect to each X_i, assuming known standard uncertainties for each input.

3.6.2 Uncertainties for the SRHT Rig

The complexity of the heat transfer coefficient (HTC) evaluation process required the application of both uncertainty quantification methods. For smooth surfaces, the *Monte Carlo Method (MCM)* was selected due to the large number of variables influencing the results. In contrast, for rough surfaces, the difficulty in formulating a descriptive equation for each contributing process made exclusive use of the MCM impractical. Therefore, the *Taylor Series Method (TSM)* was also employed to supplement the analysis. The procedures used to evaluate uncertainties arising from the acquisition, HTC computation, and surface modeling processes are extensively detailed in previous works [103, 105, 106].

In this study, a dedicated analysis was performed to evaluate the impact of camera inclination and test repeatability. Using the *TSM* approach, the HTC uncertainty was expanded to include the camera-induced error. Three different camera configurations were considered, resulting in a total of seven tests: the first three were performed with the camera oriented upstream, while the last four featured a downstream orientation. Among these, the fourth test uniquely positioned the camera to view the side wall of the test section.

All tests were conducted under identical flow conditions and focused on the last available plate. For each configuration, the global Nusselt number was calculated by averaging the local Nusselt values over the entire plate surface. The resulting global values are reported in Fig. 3.15, where the dashed line denotes the overall mean across all
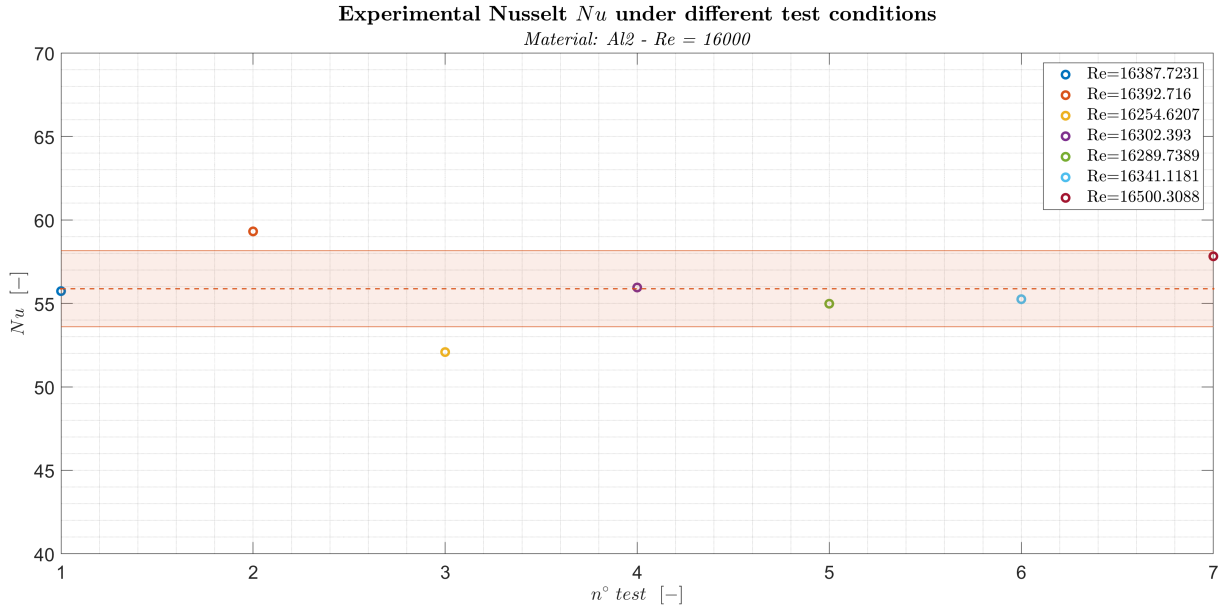
Figure 3.15: Global Nusselt number for each test. The dashed line indicates the average global Nusselt number across all tests, while the shaded area denotes the standard deviation.

tests, and the shaded area indicates the standard deviation from that mean. This standard deviation quantifies the uncertainty associated with camera positioning and test repeatability. It is defined as:

$$\sigma_{Nu} = \sqrt{\sigma_{\text{rep}}^2 + \sigma_{\text{angle}}^2} \simeq 2.2$$

In Fig. 3.16, the streamwise evolution of the laterally averaged Nusselt number is presented using the non-dimensional coordinate. The dashed lines represent the global average Nusselt number for each test, while the markers indicate the local laterally averaged values. Despite slight discrepancies between tests, the profiles exhibit a consistent trend along the streamwise direction, confirming the reliability of the local results.

Figure 3.17 displays the local Nusselt number distributions. The 3.17(a) plot shows the mean local Nusselt value, computed by averaging all seven test cases. On the other hand, Fig. 3.17(b) presents the corresponding standard deviation, which is of particular interest as it highlights spatial uncertainty introduced during the mapping process. Higher standard deviation values are observed near the intersections between the spheres and the plate, where occlusions due to geometric features hinder accurate IR measurement. Notably, these high-deviation zones often coincide with regions of elevated local Nusselt numbers, resulting in a relatively low percentage error (Fig. 3.17(c)). In some instances, however, the standard deviation is comparable to or even exceeds the local value, indicating a relatively larger uncertainty and sug-
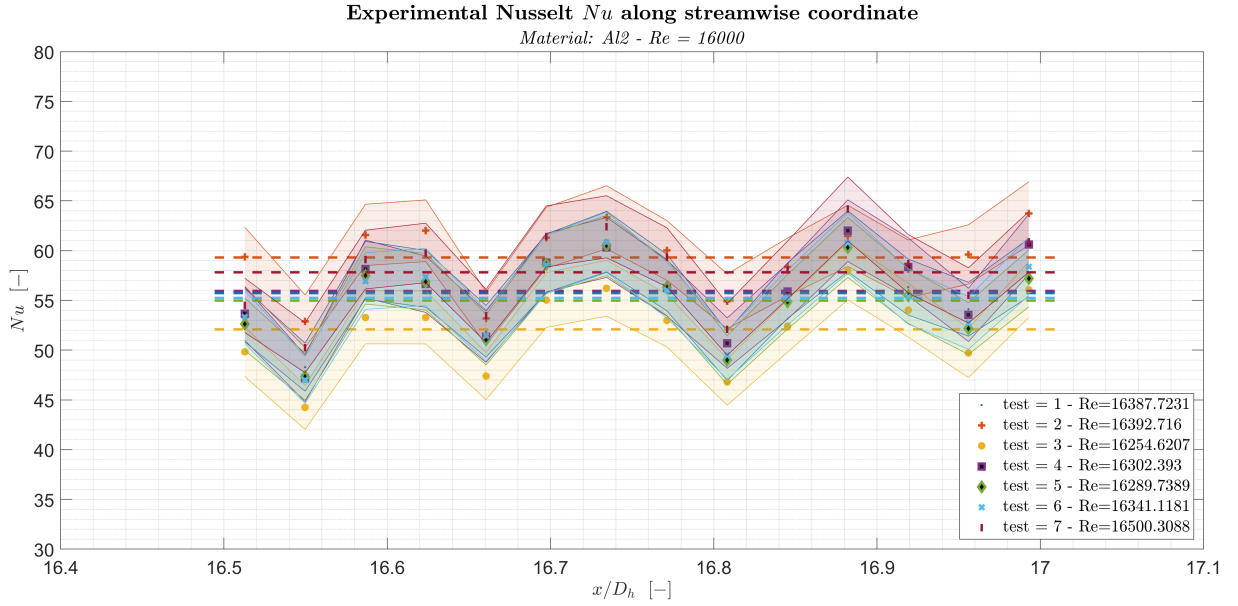
Figure 3.16: Laterally averaged Nusselt number along the streamwise direction for all seven tests. Markers represent local values, while dashed lines correspond to global averages per test.
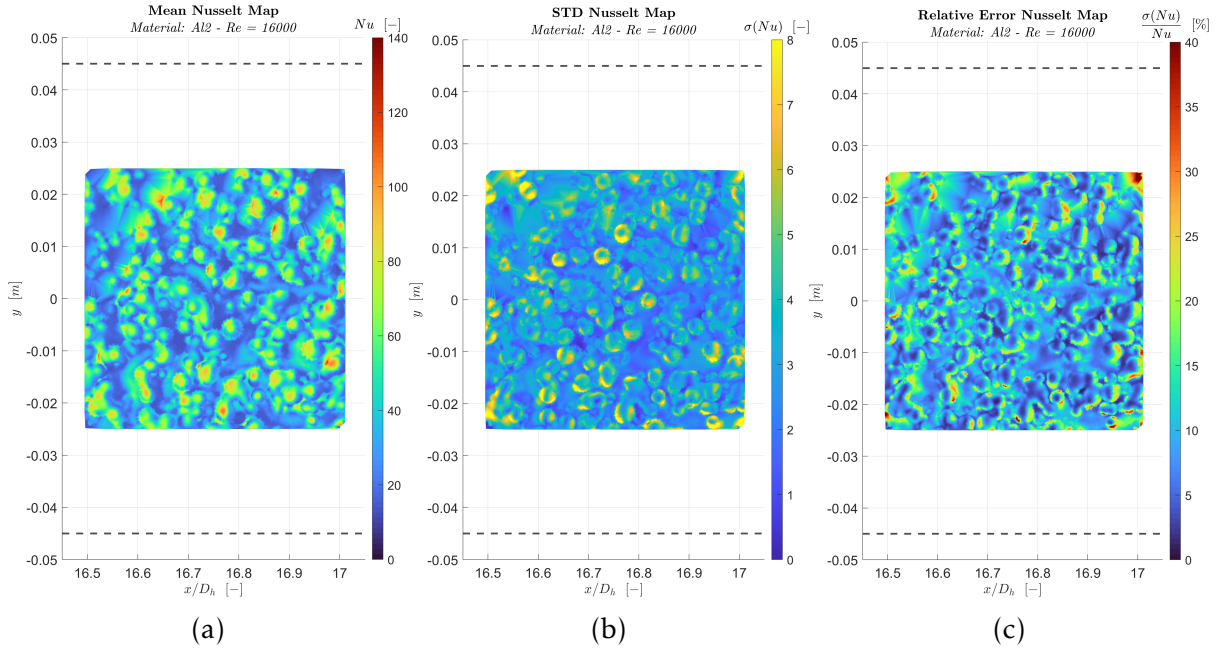
Figure 3.17: (a) Mean local Nusselt number over the seven test cases. (b) Standard deviation of the local Nusselt number. (c) Percentage error of the local Nusselt number, highlighting regions with increased uncertainty due to occlusion or mapping errors near complex geometries.

gesting caution in interpreting those local enhancements. These findings demonstrate that while the overall trends are robust, certain localized features must be analyzed carefully to avoid misinterpretation of the roughness-induced heat transfer mechanisms.

Chapter 4

Results

This chapter presents the results obtained from the experimental and numerical investigations conducted in the present study. The analysis begins with the smooth surface cases, which were used to validate the experimental setup and verify the consistency of the measurements with the underlying physical principles. Following this, the results for the rough surfaces are examined, with a focus on assessing the influence of surface roughness on local heat transfer enhancement.

Finally, the outcomes from the PIV rig experiments [118] are introduced to provide a comparative aerodynamic perspective. These results are correlated with the thermal measurements in order to elucidate the local flow phenomena responsible for variations in heat transfer performance.

4.1   Rig Modification

The primary objective of the SRHT rig modifications was to ensure the development of a fully established turbulent flow within the test section. In the previous configuration, Brogliato [106] validated his results against the modified Gnielinski correlation, which accounts for entrance effects. Although a reasonable agreement was obtained, the hydraulic length of the channel (L/D_h) remained below the recommended minimum development length of $x_{f_{d,h}} \gtrsim 10$.

To enhance the accuracy of the heat transfer measurements, within the constraints imposed by the available laboratory space, the flow straightener was shortened by 50%, and the length of the test section was doubled. Additionally, to further improve the flow uniformity at the inlet, a honeycomb element was installed at the entrance of the flow straightener.
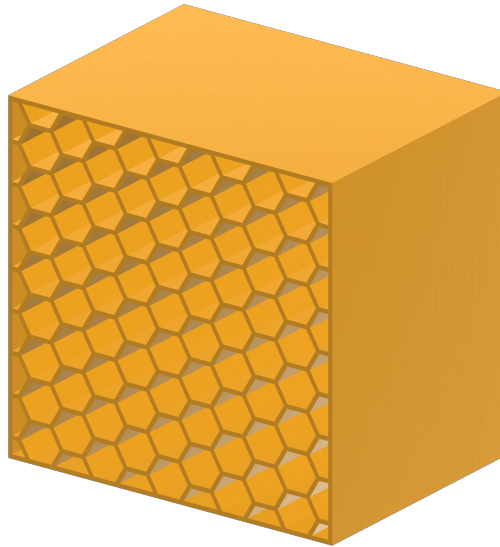
Figure 4.1: Honeycomb for the SRHT Rig

4.1.1   Thermal Boundary Layer Probe
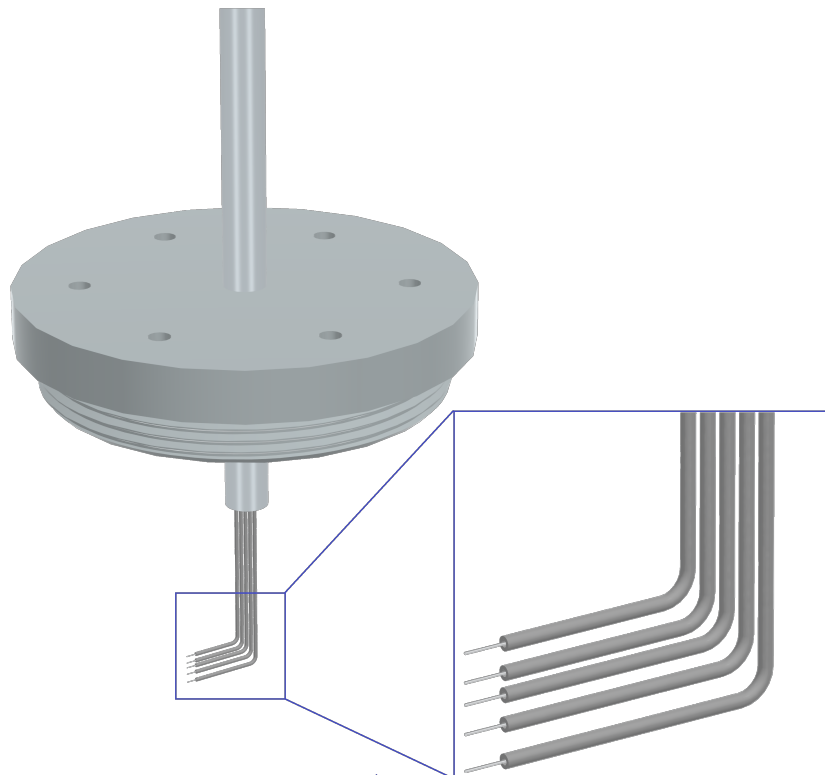
Figure 4.2: Thermal boundary layer probe with five vertically aligned Type K thermo-couples, allowing precise spacing and adjustable wall-normal positioning

To investigate the development of the thermal boundary layer above the surface of the test object, a custom-designed measurement probe was developed and manufactured. The probe consists of five Type K thermocouples arranged in a vertically aligned configuration, forming a rigid thermocouple rake. Type K thermocouples were selected for their fast response time, durability, and broad operating temperature range, making them well suited for convective heat transfer measurements in air.

Each thermocouple junction was carefully bent and fixed to maintain a precise and uniform spacing between measurement points, enabling high-resolution wall-normal temperature profiling. The probe assembly is mounted on a vertically translatable support, allowing precise positional adjustment relative to the test surface. This configuration ensures accurate positioning of the lowest thermocouple at a defined height above the wall, which is essential for resolving the steep near-wall temperature gradients and capturing the structure of the thermal boundary layer in turbulent channel flow.

4.2 Smooth Surface

The hydraulically smooth channel, with plates coated in thermal paint, was tested at four different Reynolds numbers. The heat transfer coefficient (HTC) was evaluated over the entire bottom surface, along with the laterally averaged trend in the streamwise direction. In the final portion of the channel, the computed Nusselt numbers and thermal boundary layer behavior were compared against established literature correlations. All results are presented in terms of the Nusselt number, which is directly proportional to the HTC according to the relation:

$$Nu = \frac{hD_h}{k_{\text{air}}}$$

The lateral average of the Nusselt number at a given streamwise location x_i is defined as the average over all lateral positions y_j:

$$\overline{Nu}_i = \frac{1}{N} \sum_{j=1}^{N} Nu\left(x_i, y_j\right)$$

The global average Nusselt number over the selected region is then defined as:

$$\overline{Nu} = \frac{1}{M} \sum_{i=1}^{M} \overline{Nu}_i$$
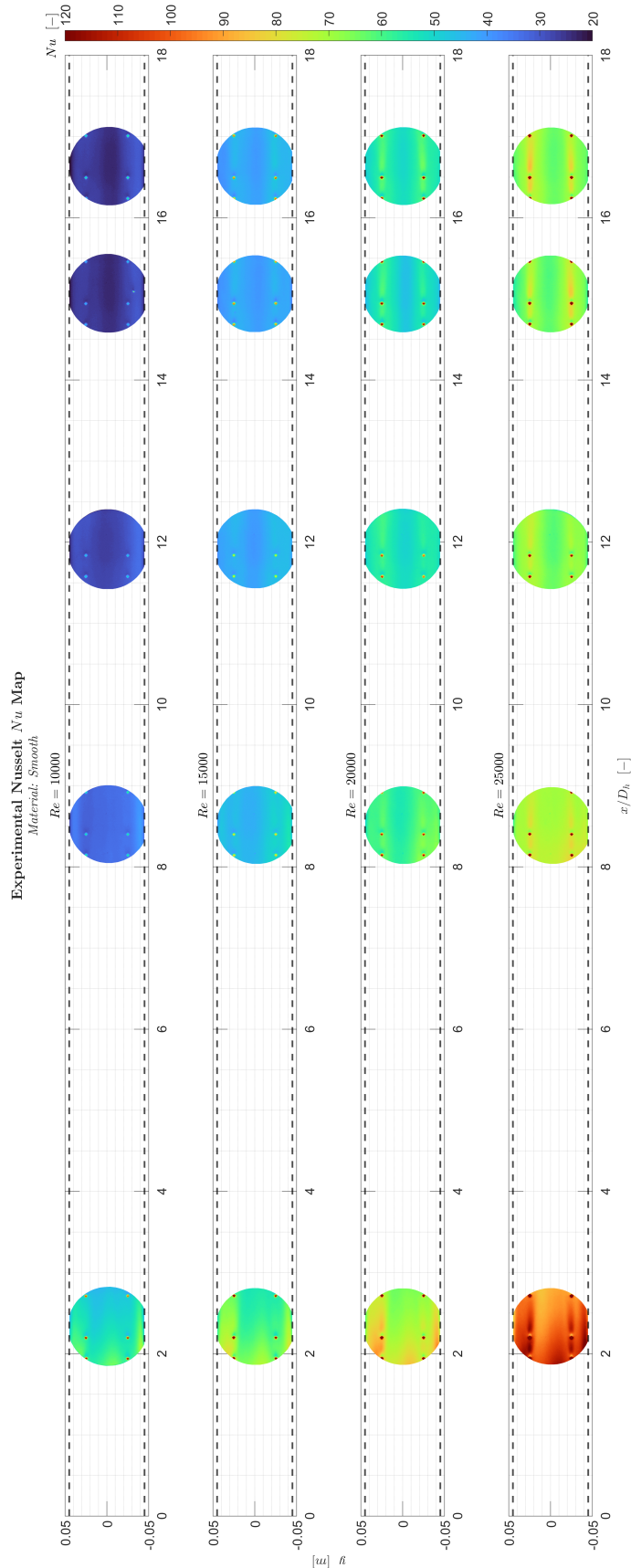
Figure 4.3: Nusselt number distribution over the smooth surfaces along the streamwise direction for the different Reynolds numbers

4.2.1 Nusselt Results

Using the measured wall temperature over the bottom plates, which depends on the physical and thermal properties of the specific material, and the corresponding bulk air temperature, the HTC distribution and, subsequently, the Nusselt number distribution were determined. Figure 4.3 shows the spatial distribution of the Nusselt number along the streamwise direction for each Reynolds number tested. The dashed black lines indicate the lateral boundaries of the test section, within which the region of interest is analyzed.

As expected, the highest Nusselt values are observed at the highest Reynolds number ($Re = 25\,000$). For a given Reynolds number, the Nusselt number exhibits a decreasing trend from the inlet toward the outlet, a typical behavior in the thermal entrance region of a channel. As the flow progresses downstream, the Nusselt number gradually decreases until it reaches an approximately constant value in the last portion of the test section, indicating the onset of thermally fully developed conditions.

Across the lateral direction (y), a small deviation in the Nusselt number is observed, particularly near the side walls, due to wall-induced effects. To minimize wall-induced influences in the averaged values, all statistical analyses were performed within a central region bounded by the reference points.

Although only a limited number of streamwise positions were tested due to time constraints, the Nusselt number trends across the smooth surfaces follow the expected theoretical behavior. Therefore, it is reasonable to infer the intermediate values between the tested positions.
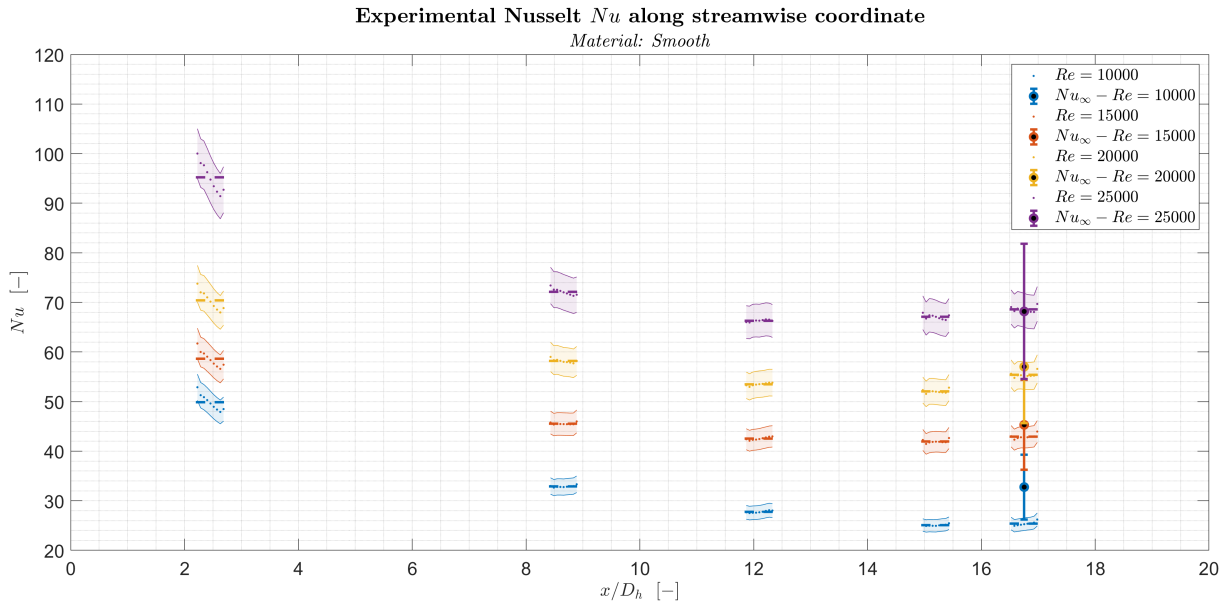
Figure 4.4: Reduced laterally averaged Nusselt number over the smooth surfaces within the reference points along the streamwise coordinate, for different Reynolds numbers

The decreasing trend of the Nusselt number along the channel is clearly observed in the laterally averaged profiles shown in Fig. 4.4. In this figure, each dot represents a local laterally averaged value $\overline{Nu}_i$, the dashed lines indicate the global average $\overline{Nu}$, and the shaded regions denote the associated uncertainty bounds. As the flow develops thermally along the channel, the Nusselt number gradually stabilizes, eventually forming a plateau. According to theoretical expectations, this plateau is reached farther downstream as the Reynolds number increases.

Indeed, previous studies by Lehmann [103] and Brogliato [106] observed a slight decreasing trend in Nusselt number near the channel outlet for $Re = 25\,000$. With the extended test section introduced in the present study, a clear plateau is observed even at such a high Reynolds number, confirming the presence of fully developed thermal conditions.

4.2.2 Thermal Boundary Layer Measurements

The evaluation of the thermal boundary layer (TBL) was performed at different Reynolds numbers over the final test plate, where the flow can be thermally assumed as fully developed. As introduced in Sec. 2.6.4, the thermal boundary layer is composed of distinct regions, including the viscous sublayer and logarithmic region. In the present study, only the logarithmic portion of the TBL is considered, due to the spatial resolution constraints imposed by the thermocouple size and spacing.

Since the structure of the TBL depends not only on the flow regime but also on the Prandtl number, several empirical correlations for the logarithmic layer exist in the literature. A selection of these correlations is reported in Fig. 4.5.
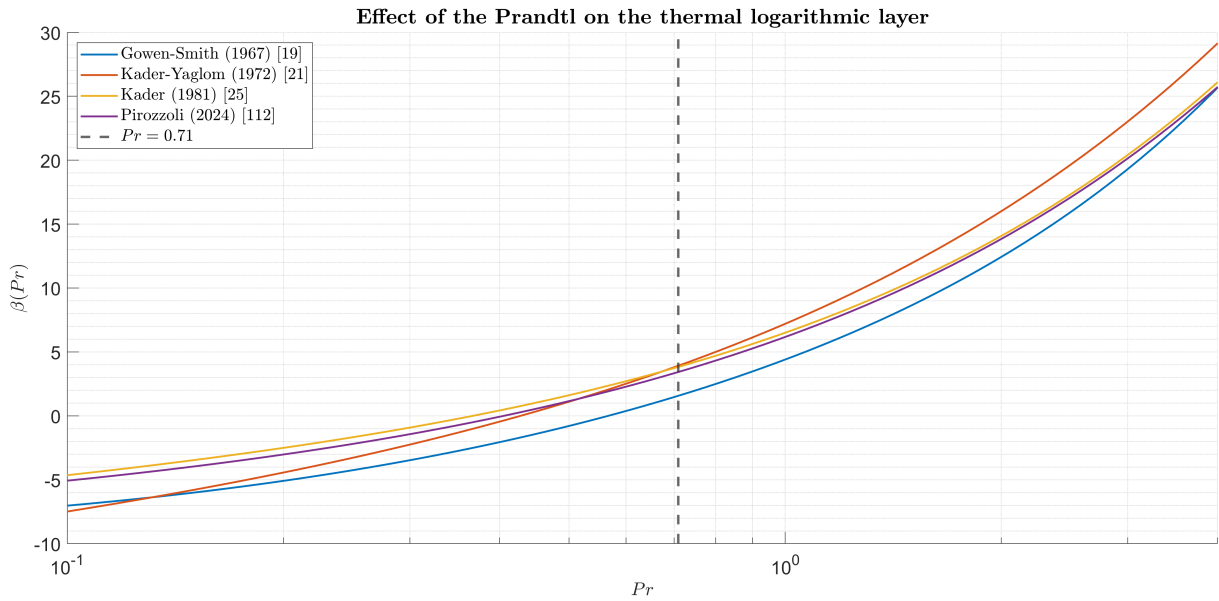
Figure 4.5: Experimental and empirical correlations for the $\beta(Pr)$ function from literature
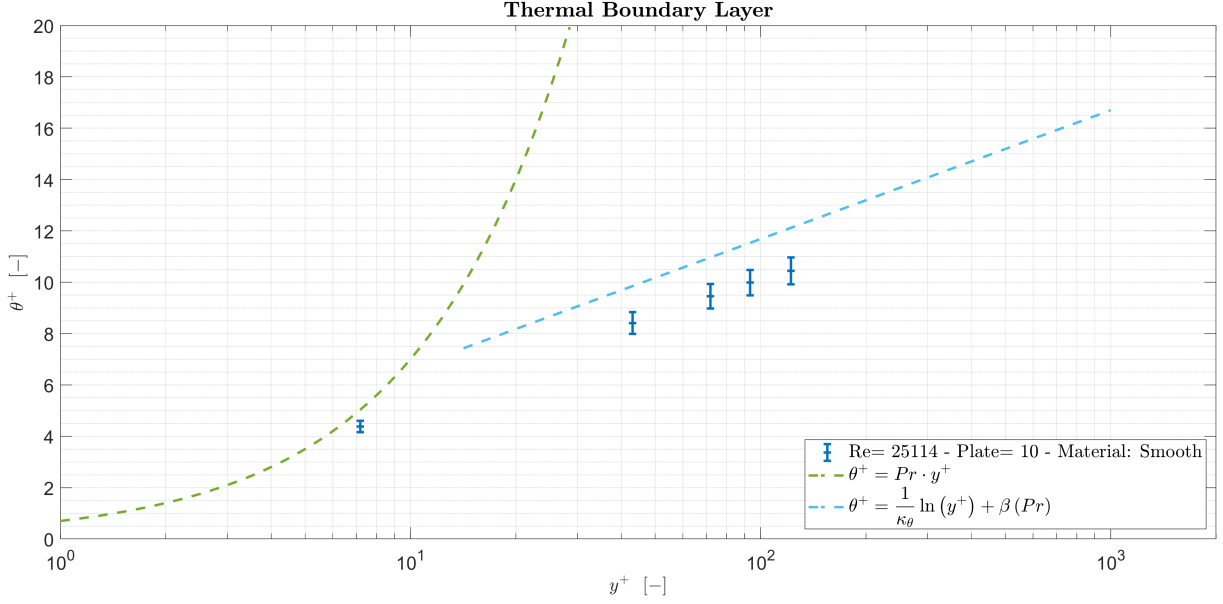
Figure 4.6: Non-dimensional temperature profile within the thermal boundary layer at thermally fully developed conditions for the smooth test object. The measured data are compared to theoretical functions for the viscous sublayer and logarithmic region.

In this work, the correlation proposed by Gowen and Smith [19] is adopted, owing to the similarity between their test setup and the current experimental configuration. Figure 4.6 shows the experimental data for the smooth channel compared with the theoretical temperature profiles for both the viscous sublayer and logarithmic region.

The required adimensional quantities are derived as follows: the friction velocity u_τ is computed from the Darcy friction factor f_D, evaluated via the Colebrook-White equation (Eq. (2.11)), and it is consistent with findings from the PIV rig measurements on the same surfaces [118]. The wall heat flux q_w, which is needed to compute the friction temperature, is obtained from IR thermography using the relation Eq. (2.3).

$$ u_\tau = u_\infty \sqrt{\frac{f_D}{8}} \qquad ; \qquad q_w = h\left(T_\infty - T_w\right) $$

The temperature profiles measured by the thermocouple rake were non-dimensionalized and plotted against the logarithmic temperature law. As shown in Fig. 4.6, the data generally follow the expected logarithmic trend, albeit with a slight downward shift.

This discrepancy may be attributed to several factors:

- inflow disturbances and minor flow instabilities in the channel;

- limited thermocouple accuracy and response time;

- positional uncertainty in the vertical placement of the thermocouple rack;

- uncertainty in the empirical $\beta(Pr)$ function, which is derived from studies on longer and thinner channels.

To account for these sources of uncertainty, an estimated error margin of 5% is included in the experimental data. Despite these limitations, the first thermocouple in the array appears to capture values within the thermal viscous sublayer. Although this region is highly sensitive to measurement errors, the recorded values approximate the theoretical function and reproduce the overall shape of the thermal boundary layer profile.

4.2.3   SRHT Rig Validation

The attainment of a fully developed turbulent flow condition within the SRHT rig was verified by analyzing the streamwise evolution of the velocity profile along the channel. As theoretically expected and illustrated in Fig. 2.31, a fully developed turbulent flow exhibits a velocity profile that remains invariant along the streamwise direction. This profile is characterized by a sharp velocity gradient near the wall and a relatively flat core region, indicative of enhanced momentum transport due to turbulent mixing.

To experimentally confirm this condition, velocity profiles normal to the wall were measured at several streamwise locations using Hot-Wire Anemometry (HWA). It should be noted that the SRHT-rig validation was performed under ambient-temperature flow conditions. The resulting data, shown in Fig. 4.7, demonstrate that the velocity profiles corresponding to the final two test plates are nearly identical. Their overlap confirms the presence of a hydrodynamically fully developed turbulent regime in the downstream portion of the test section, thereby validating the effectiveness of the rig design and its recent modifications.

In addition to confirming the hydrodynamic development, the validity of the experimental results must also be assessed from a thermal perspective. In the final portion of the test section, the flow is expected to be close to thermally fully developed. Therefore, the globally averaged Nusselt number computed in this region can be compared with values predicted by standard empirical correlations for fully developed internal flows, such as the Dittus-Boelter or Gnielinski correlations.

For this purpose, the Dittus-Boelter correlation, introduced in Sec. 2.7.5, is employed in the following form:

$$Nu_\infty = 0.023 \cdot Re_D^{0.8} \cdot Pr^{0.3}$$

In Fig. 4.4, the corresponding theoretical values for fully developed turbulent internal flow, obtained from the Dittus-Boelter correlation (Nu_∞), are shown using black markers in the same color as their respective trend lines. For visualization purposes, the markers are placed arbitrarily at the end of the last test plate (i.e., within the thermally developed region).
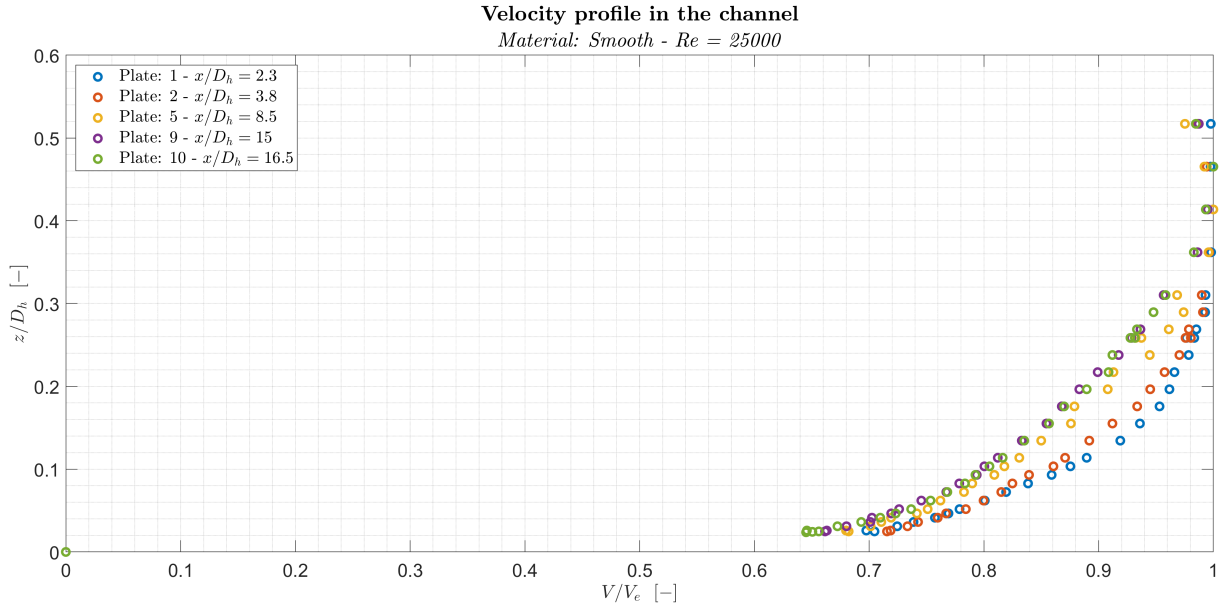
Figure 4.7: Streamwise velocity profiles measured using Hot-Wire Anemometry at different streamwise positions under ambient-temperature flow conditions

For all Reynolds numbers investigated, the Nusselt number trends agree well with the theoretical Nu_∞ values. Although slight deviations exist between the average experimental values and their respective theoretical predictions, the uncertainty intervals overlap entirely. This overlap reinforces the assumption that the last portion of the channel can be regarded as thermally fully developed, thereby validating the experimental methodology and the effectiveness of the SRHT rig for surface heat transfer investigations.

4.3   Rough Surfaces

To investigate the flow characteristics and heat transfer behavior in the presence of various rough surface configurations, dedicated tests were performed on all available rough plates.

4.3.1   Nusselt Results

The results for the rough surfaces in terms of Nusselt number are presented to investigate the general heat transfer behavior. The laterally averaged Nusselt number ($\overline{Nu_i}$) is plotted against the non-dimensional streamwise coordinate. As observed for the smooth channel, a decreasing trend from the inlet to the outlet is confirmed.

Although experiments were conducted at $Re = 10000, 15000, 20000, 25000$, only the results for $Re = 25000$ will be considered and analyzed hereafter.

A key feature in these graphs is the presence of oscillations in the laterally aver-
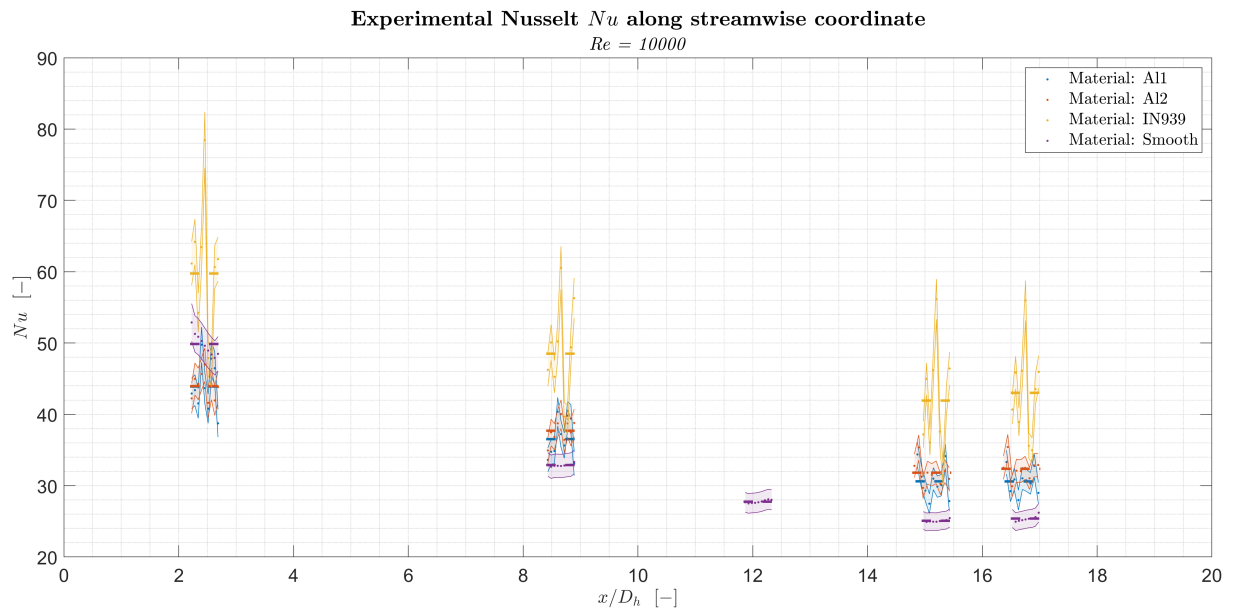
Figure 4.8: Laterally averaged Nusselt number distribution for rough plates at *Re* = 10000
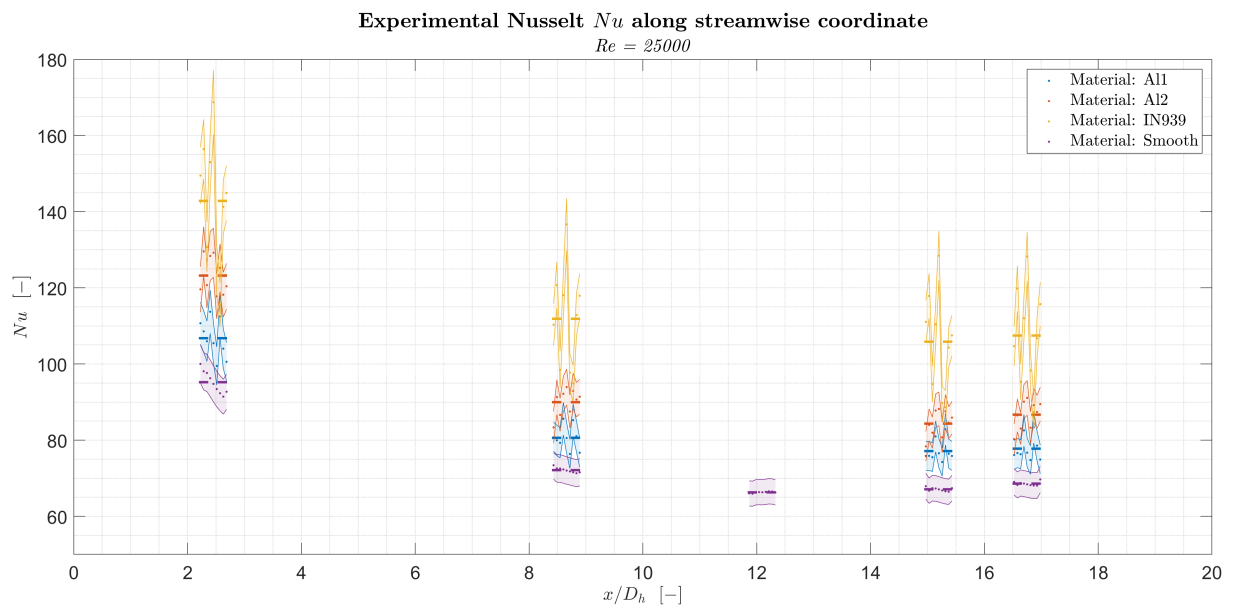
Figure 4.9: Laterally averaged Nusselt number distribution for rough plates at *Re* = 25000

aged Nusselt number. As expected, the introduction of surface roughness causes non-uniform heat transfer conditions across the plate. This results in a spatially varying Nusselt distribution, as clearly visualized in the Nusselt maps shown in Fig. 4.10. The main causes for this non-uniformity include enhanced turbulence, vortex generation by roughness elements, and direct interaction between the flow and rough features.

One immediate observation when looking at Fig. 4.10 is that the Nusselt number increases with increasing Reynolds number. A streamwise decreasing trend is evident, and the last two windows show a plateau, indicating that the flow has become thermally fully developed. The initial region displays the highest Nu peak, a signature of entrance effects caused by the flow expansion as it enters the test section. The presence of roughness elements introduces turbulence and flow impingement, which is manifested in the strong oscillatory behavior of the Nusselt number distribution. Compared with smooth surface results (see Fig. 4.9), the thermally developed region is reached earlier due to enhanced turbulence from the roughness. This observation aligns with recent studies showing that surface roughness can accelerate thermal development in microscale channels, especially in additively manufactured surfaces.

Several effects can be identified from Figs. 4.8 and 4.9:

- *Reynolds Number Effect*: As expected, increasing Reynolds number leads to higher Nusselt values across all roughness configurations. The convective heat transfer is directly affected by flow velocity.

- *Entrance Region Effect*: The typical Nusselt trend shows an initial high value followed by a gradual decline toward a stable plateau. This behavior is more pronounced at higher Reynolds numbers, where the thermal entrance region is longer.

- *Relative Roughness Effect*: The material used and its associated roughness significantly influence heat transfer. Surfaces with higher relative roughness, such as *Inconel 939*, demonstrate superior heat transfer performance compared to smoother configurations like *Aluminium 1* and *Aluminium 2*, and, naturally, the smooth channel. Higher roughness also introduces greater oscillations in the laterally averaged Nusselt due to alternating zones of intense and weak heat transfer.

The local thermal behavior is examined for the three rough plates: *Inconel 939*, *Aluminium 1*, and *Aluminium 2*. The final measurement window (see Fig. 4.12) is considered representative of the thermally fully developed region. Beyond the Reynolds effect previously discussed, surface roughness (SR) characteristics now become critical.
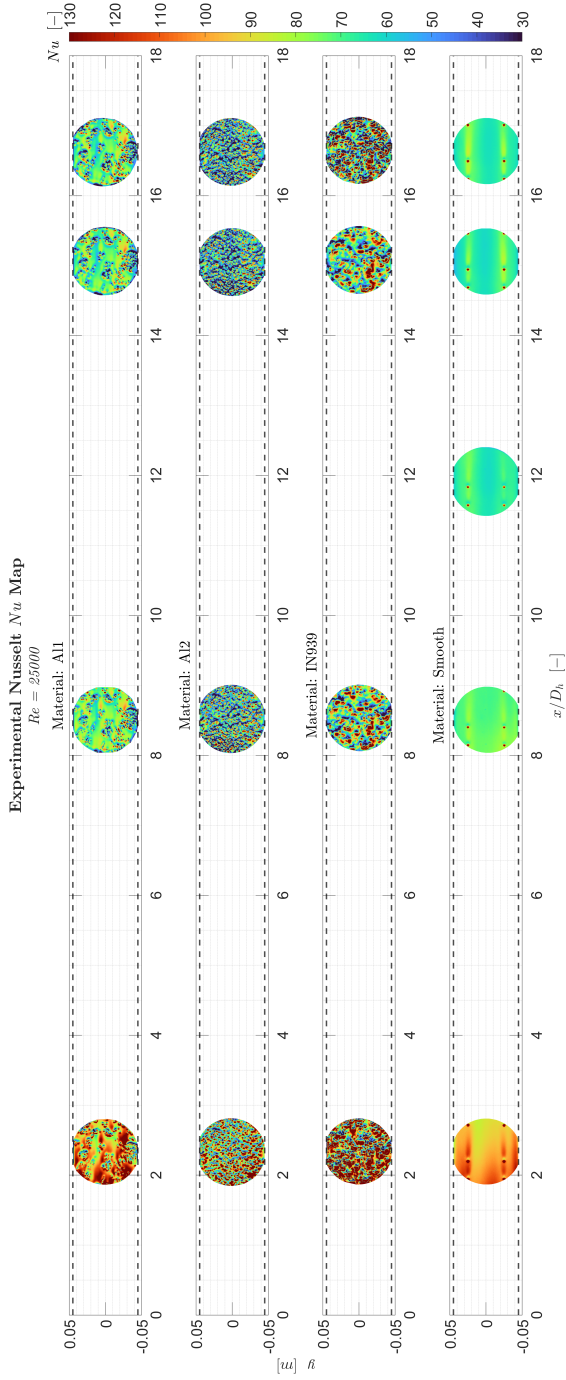
Figure 4.10: Local Nusselt distribution at $Re = 25000$ for all rough plates
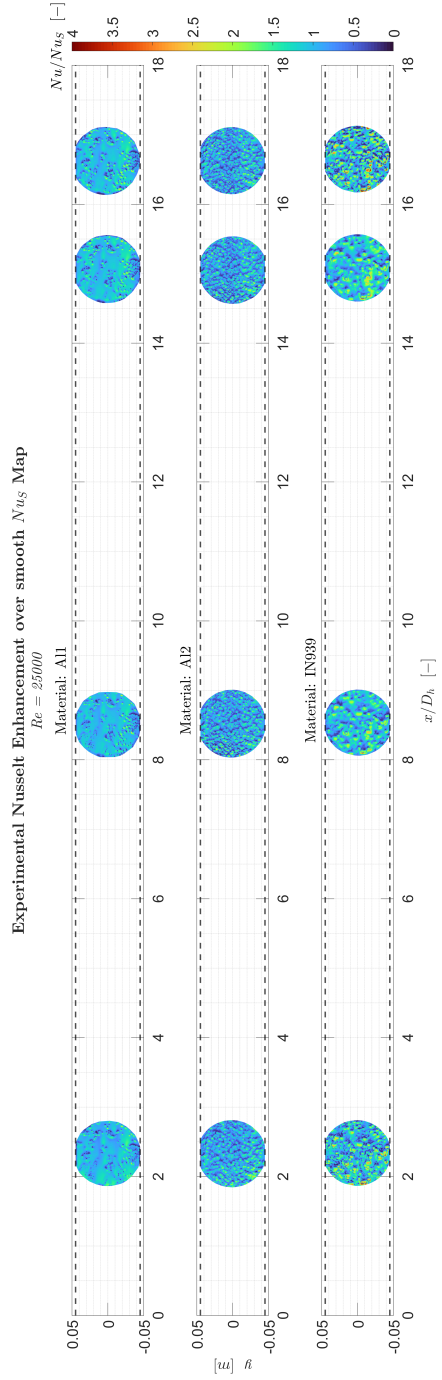
Figure 4.11: Local Nusselt enhancement map (Nu/Nu_S) for all rough plates at $Re = 25000$
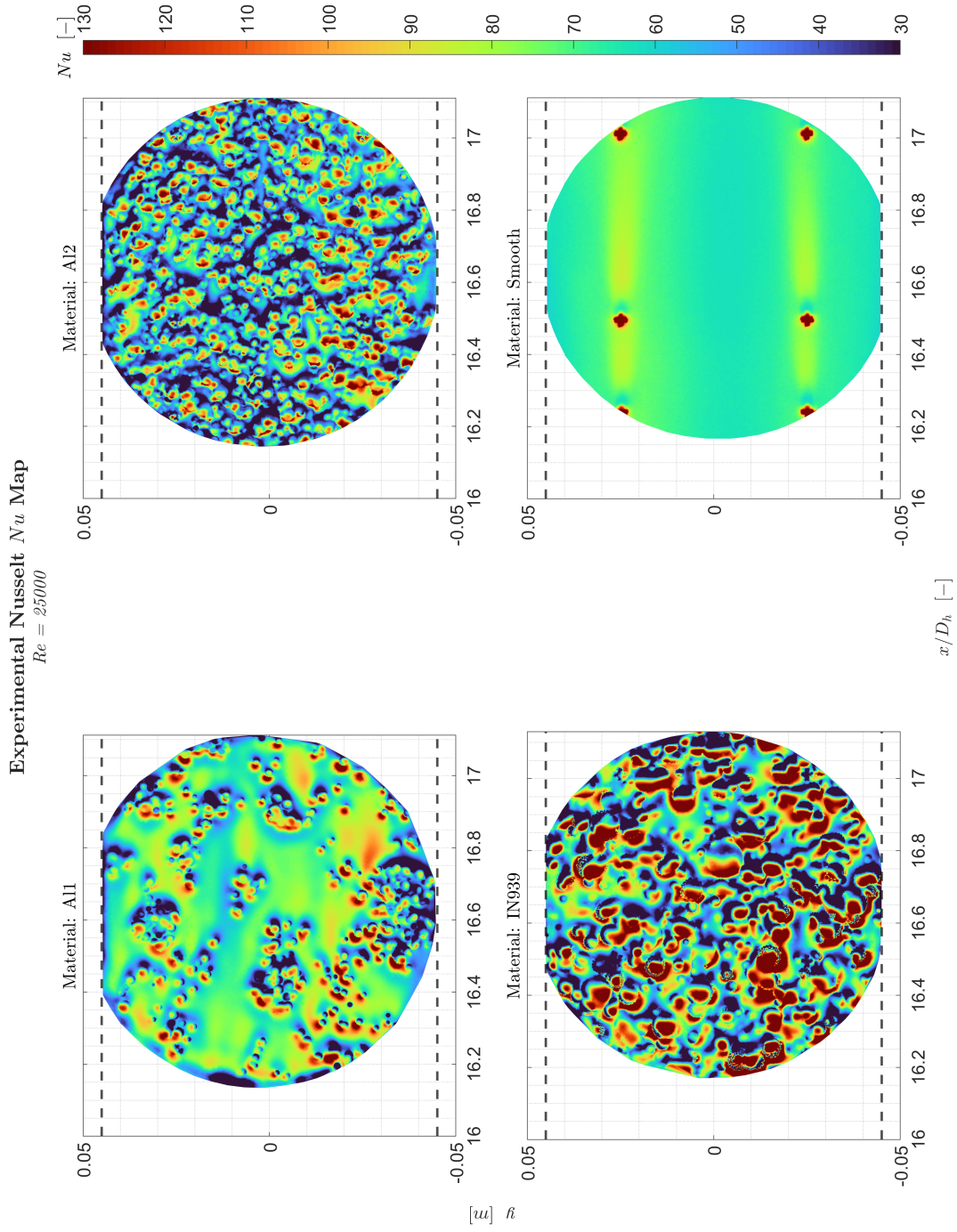
Figure 4.12: Local Nusselt distribution in the last window (thermally fully developed region) at $Re = 25000$

The *Inconel 939* plate features high relative roughness, with small satellite particles anchored to larger roughness elements. Conversely, *Aluminium 1* exhibits wider smooth zones and fewer rough elements, often appearing in clusters. Consequently, *Aluminium 1* shows lower heat transfer performance, particularly in smooth zones with low local Nu. In contrast, *Inconel 939* lacks extensive smooth areas, and the flow-exposed rough elements register high local Nu. It is worth noticing that, for example in the case of *Aluminium 2*, there are instances where rough elements exhibit low heat transfer, likely due to corner flows or separation zones. A more detailed explanation about these phenomena will be provided in the following section.

To assess local heat transfer enhancement, the ratio Nu/Nu_S is evaluated by comparing each rough surface to the corresponding smooth surface. This dimensionless metric helps isolate the contribution of roughness by eliminating the influence of bulk flow conditions.

From Fig. 4.11, two main effects can be inferred [106]:

- *Turbulence-Induced Enhancement*: Roughness-induced vortices increase wall shear stress over smooth spots, boosting heat transfer locally even where direct roughness is absent.

- *Direct Impact Enhancement*: Areas where the flow directly impinges on rough elements experience high local Nu due to stagnation and acceleration effects.

The phenomenon of *Direct Impact Enhancement* can also be analyzed through the frontal solidity parameter, λ_f. As reported in Table 3.1, the *Inconel 939* test object exhibits the highest frontal area, which correlates with the most significant Nusselt number enhancement. Conversely, *Aluminium 1*, characterized by the lowest λ_f, also displays the lowest level of thermal enhancement. The λ_f parameter further enables the classification of roughness types into *d-type* and *k-type* regimes (refer to Sec. 2.7.4.1), providing useful insight into the flow behavior and underlying physics associated with rough surfaces. However, for a complete and reliable characterization of surface roughness, a broader set of geometrical and statistical parameters must be considered in conjunction with λ_f as mentioned in the previous chapters.

4.3.2   Correlations with PIV Rig

The following analysis compares the thermal results obtained from the SRHT rig with aerodynamic insights from the PIV rig [118]. Specifically, flow structures interacting with various rough surfaces are examined graphically to help explain the observed thermal behavior. It is important to note that although the same test section geometry was used in both rigs, the flow conditions slightly differ; for instance, the PIV rig operates at ambient temperature.

PIV measurements were conducted in the same region where the Nusselt number trends and maps were acquired for the three rough surfaces. Pedreño Marín [111] and Brogliato [106] previously hypothesized that zones downstream of roughness ele-

ments could lead to Nusselt number reductions due to vortex formation and recirculating flows.

The results combining thermal and aerodynamic data are illustrated in Figs. 4.13, 4.14, and 4.15, respectively corresponding to the *Inconel 939*, *Aluminium 1*, and *Aluminium 2* surfaces.
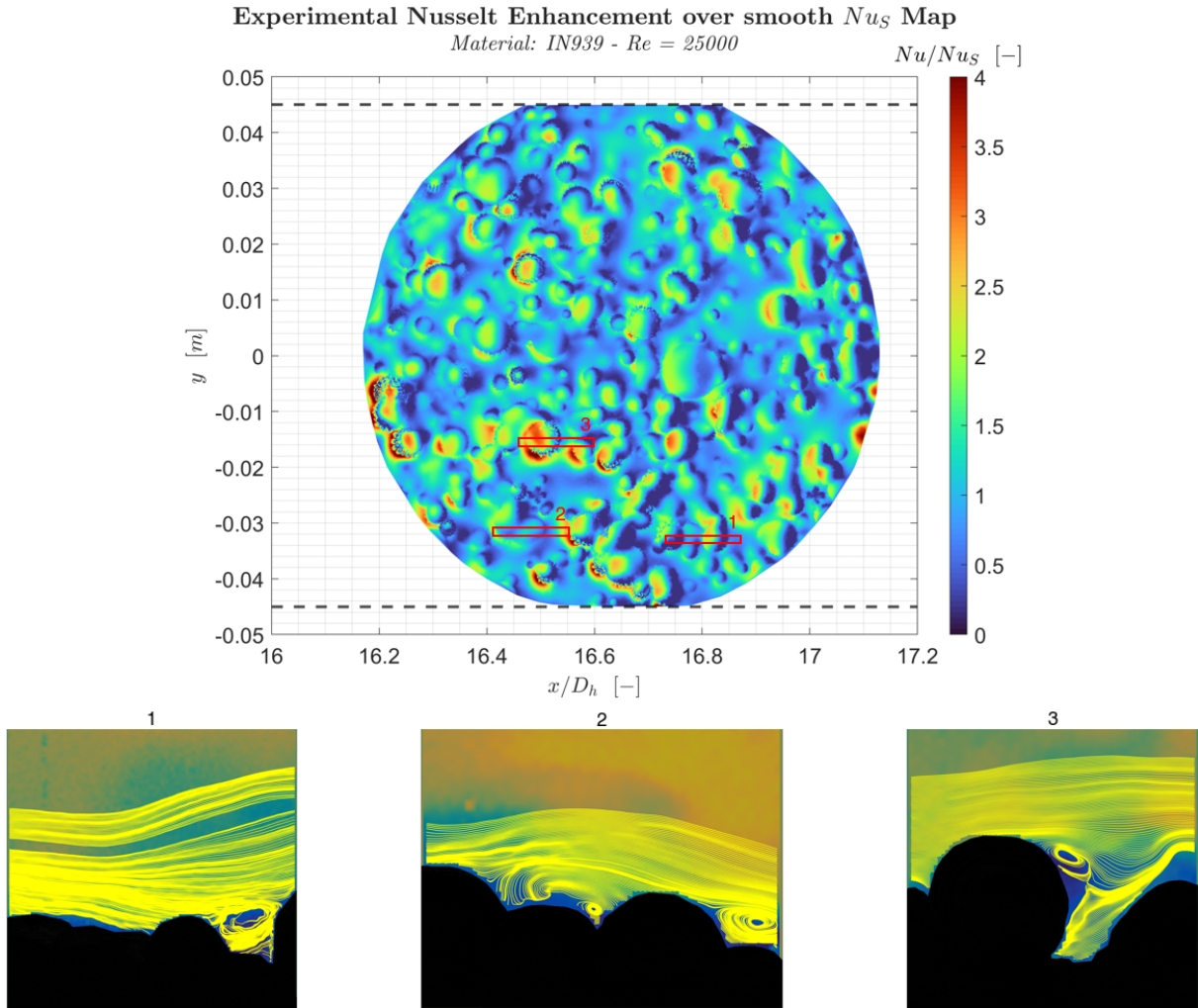
Figure 4.13: Comparison between PIV flow visualization and Nusselt distribution for *Inconel 939*. Analysis areas highlight vortex recirculation and local heat transfer suppression/enhancement.

Multiple analysis areas were defined, categorized by ascending numbering to represent different roughness characteristics. In the case of *Inconel 939*, Fig. 4.13 reveals that regions with high local Nusselt numbers are often followed by downstream regions exhibiting low Nu values. A comparison between PIV data and thermal maps highlights the formation of recirculating "air bearings" behind roughness peaks. These so-called "impermeability zones" prevent direct contact between the main flow and the

wall, resulting in decreased convective heat transfer. Conversely, in regions where the flow is forced to impinge upon the wall, the Nusselt number rises. This can suggests that both increased protrusion into high-velocity regions and a more extended, and therefore more exposed, frontal area lead to stronger heat transfer performance. Additionally, clear vortex shedding events are observed downstream of roughness elements, potentially enhancing flow unsteadiness and mixing.
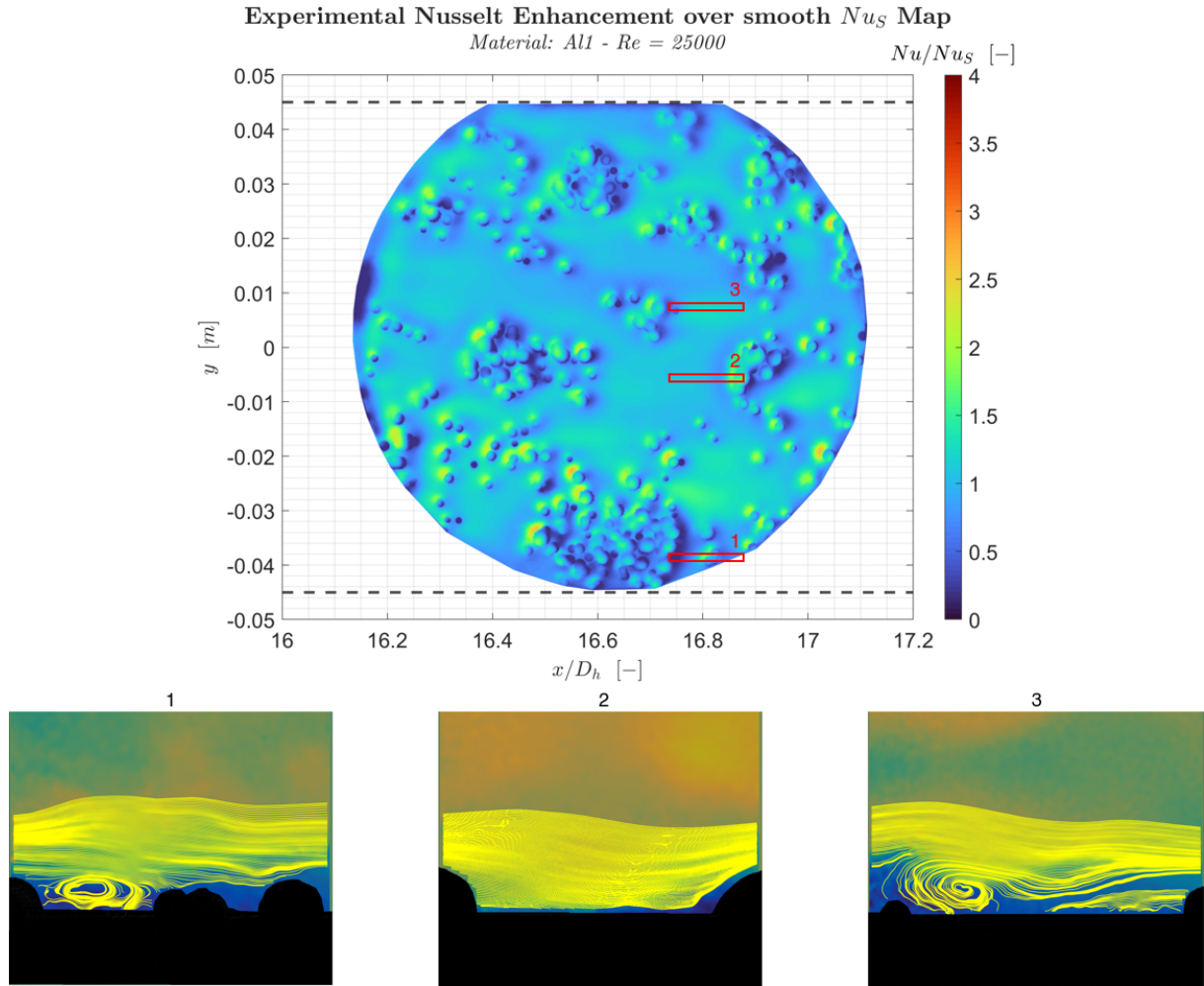
Figure 4.14: Comparison between PIV flow visualization and Nusselt distribution for *Aluminium 1*. Flow behavior is interpreted in terms of *d*- and *k*-type roughness regimes.

As discussed earlier, *Aluminium 1* exhibits a much less severe roughness compared to *Inconel 939*, with isolated peaks separated by wide valleys. In regions 1 and 3 of Fig. 4.14, the behavior can be interpreted in terms of **d**-*type* and **k**-*type* roughness. In region 1, characterized by tightly packed elements, the flow tends to remain trapped between adjacent peaks, forming recirculation bubbles that are largely decoupled from the outer flow. As a result, the flow "glides" over these valleys, with minimal influence

from the actual surface topology. In region 3, where peaks are more widely spaced, the recirculation bubble reaches the outer flow, resulting in a stronger flow deflection and increased wall interaction. Region 2 demonstrates a clear link between roughness and heat transfer: straight streamlines over smooth valleys coincide with low Nusselt values, while local increases in Nu appear immediately where the flow impacts the rising edges of the rough elements.
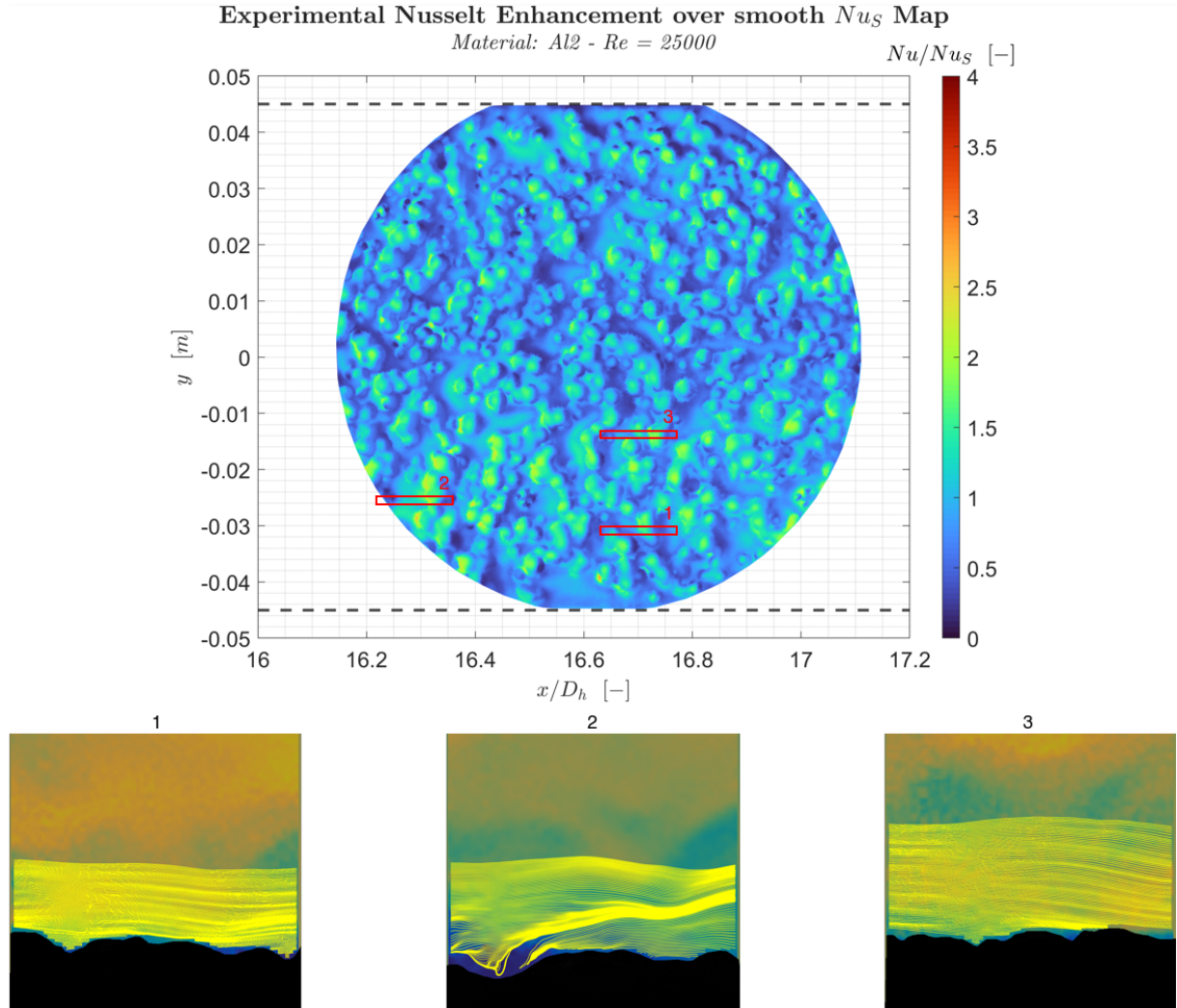
Figure 4.15: Comparison between PIV flow visualization and Nusselt distribution for *Aluminium 2*. Densely packed and uniform roughness limits flow-surface interaction and local Nu variation.

In the case of *Aluminium 2*, the relationship between flow and roughness becomes more complex. This surface features densely packed roughness elements of relatively uniform size and spacing. As a consequence, the Nusselt number distribution appears more homogeneous, with fewer pronounced peaks. This uniformity is consistent with PIV data, which show flow lines passing almost undisturbed above the surface, sug-

111

gesting that the dense roughness prevents flow penetration and inhibits localized mixing. In some isolated areas (e.g., spot 2), where small valleys between rough elements form, the flow exhibits deviations and minor impingement, resulting in localized Nu enhancement. However, these regions are infrequent and not characteristic of the overall surface behavior.
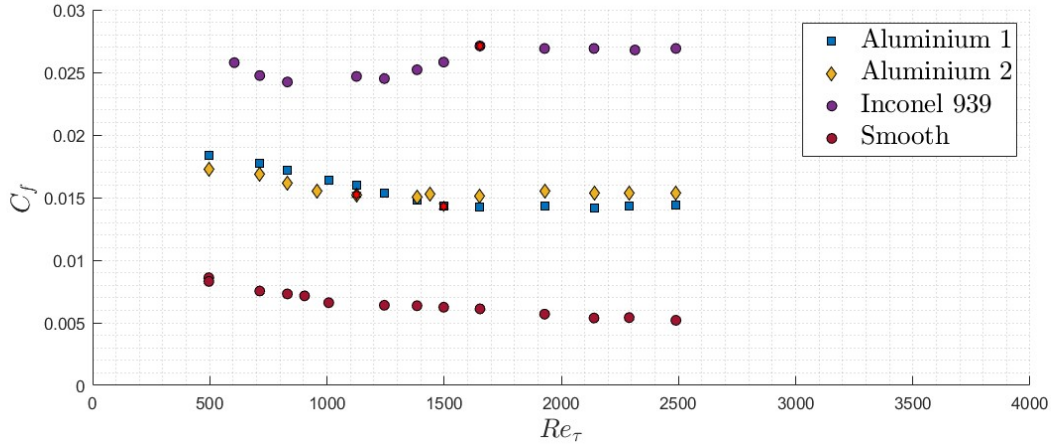
Figure 4.16: Skin-friction coefficient C_f as a function of Reynolds number for all rough plates. The plateau indicates transition to fully rough regime [118]

The PIV rig also enables the determination of the skin-friction coefficient C_f for all rough surfaces. Fig. 4.16 shows the friction coefficients over a range of Reynolds numbers. The fully rough regime is identified by the plateauing of C_f, which signifies the dominance of pressure drag over viscous drag. Naturally, the skin-friction coefficient depends on the amplitude and distribution of the roughness: *Inconel 939*, with prominent peaks, exhibits the highest values, while both *Aluminium* configurations converge toward similar, lower values.

4.3.3 Comparison with QSSHT Rig

The results from the SRHT rig are compared with data obtained from the actual AM channels tested using the qSSHT rig. These AM channels correspond to those shown in the SEM images of Fig. 3.4. In the present study, reference is made to the *Inconel 939* test object, fabricated with a 90° build orientation and a hydraulic diameter of $D_h = 1.25 \, \text{mm}$, previously tested by Pagani [99].

Figure 4.17 presents the comparison between the global Nusselt number obtained from the SRHT and qSSHT rigs as a function of Reynolds number. For the SRHT rig, the global Nusselt number $\overline{Nu}$ is computed as the average over the last two windows of the test plate, which correspond to the thermally fully developed region. The results demonstrate excellent agreement between the two rigs, supporting the reliability and consistency of both experimental approaches despite differences in operating conditions and scale.
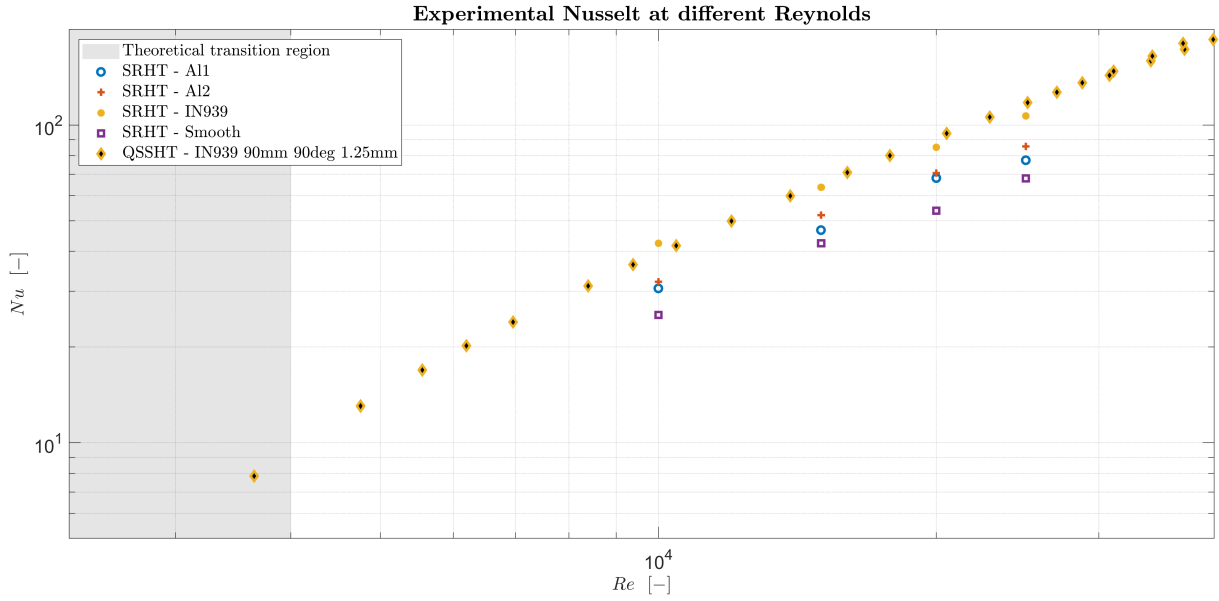
Figure 4.17: Comparison of global Nusselt number for rough surfaces between SRHT and qSSHT rigs across a range of Reynolds numbers. The SRHT data corresponds to the average over the last two windows.

The *Aluminium* test object from the qSSHT rig was excluded from this comparison due to the high uncertainty associated with its measurements.

4.3.4 Thermal Boundary Layer Measurements

The primary distinction between heat and momentum transfer lies in the absence of a direct analogy for convective heat transfer, akin to the pressure-drag relationship governing momentum transfer. In the fully rough regime, unlike wall shear stress (τ_w), the wall heat flux (q_w) does not scale with the inertial sublayer governed by the roughness height (y/k_s). Instead, q_w remains influenced by the Prandtl number and the thermal characteristics of the flow, highlighting the combined effects of roughness and molecular properties on heat transfer.

To quantify the thermal effect of surface roughness, several studies have introduced the temperature shift function, $\Delta\theta^+$, as the thermal analog of the roughness function ΔU^+ used for momentum transfer. In the presence of increasing surface roughness, a downward shift in the non-dimensional temperature profile θ^+ is observed, similar to the velocity profile U^+. However, the magnitude of this thermal shift is consistently lower than that of the velocity shift, i.e., $\Delta U^+ > \Delta\theta^+$, indicating that surface roughness enhances momentum transfer more significantly than heat transfer.

From Fig. 4.18, a qualitative comparison reveals that the *Inconel 939* surface exhibits the largest downward shift in both θ^+ and U^+ profiles [118]. For *Aluminium 1* and *Aluminium 2*, distinct values of $\Delta\theta^+$ are observed despite exhibiting the same ΔU^+, confirming that even similar momentum behavior can yield differing thermal behav-
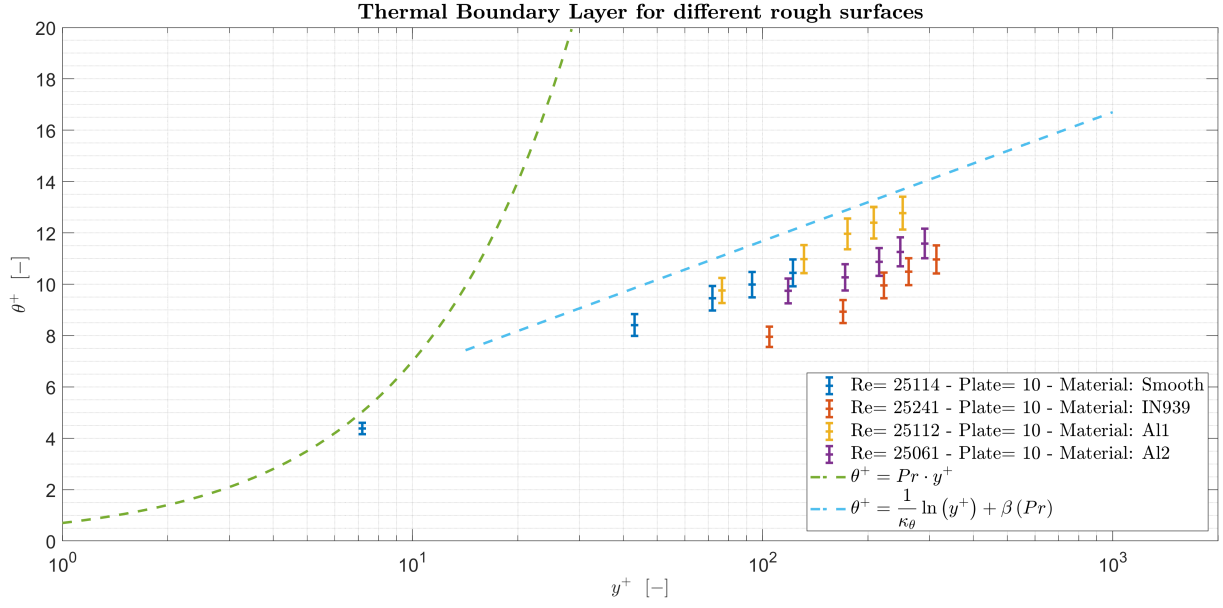
Figure 4.18: Non-dimensional temperature profile θ^+ within the thermal boundary layer under thermally fully developed conditions for the rough test objects. The profiles are compared to theoretical models for the viscous sublayer and logarithmic region.

ior.

Although a discrepancy is observed between the empirical correlation and the experimental data for smooth surfaces, the general shape and trend of the thermal profiles suggest that this approach remains a valid and promising method for future analyses of thermally fully developed rough-wall flows.

4.3.5 Performance Evaluation

Previous studies have demonstrated that surface roughness enhances the heat transfer coefficient (Nu); however, this enhancement is typically accompanied by a significant increase in friction drag (C_f). To assess the overall thermal-hydraulic efficiency of rough surfaces, the Thermal Performance Factor (TPF) is introduced. This dimensionless metric evaluates the trade-off between heat transfer enhancement and the associated pressure losses at constant Reynolds number, thus providing a balanced measure of performance:

$$TPF = \frac{Nu/Nu_S}{\left(C_f/C_{fS}\right)^{1/3}}$$

Here, the subscript $_S$ denotes values obtained for the smooth reference surface.
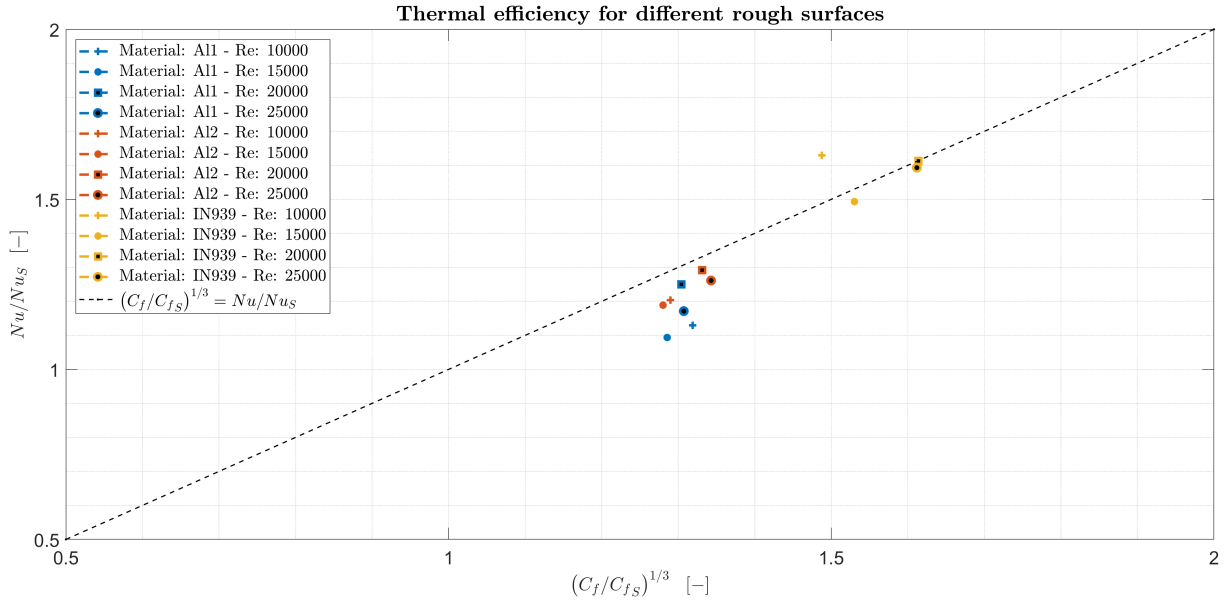
Figure 4.19: Comparison of heat transfer and friction performance for the tested rough surfaces. The ratios Nu/Nu_S and C_f/C_{f_S} are plotted.

Figure 4.19 presents the comparison of rough surfaces in terms of both heat transfer and friction characteristics. In most cases, the increase in friction factor exceeds that of the Nusselt number, resulting in a thermal performance factor $TPF < 1$. This outcome indicates that the enhancement in momentum transfer due to surface roughness dominates over the gain in convective heat transfer, leading to a net reduction in thermal-hydraulic efficiency.

Among the tested configurations, the *Inconel 939* surface generally exhibits the best performance, while the *Aluminium 1* surface performs the worst in terms of TPF. For all roughness types, the TPF shows a local maximum at $Re = 20000$, suggesting that this flow regime may offer a more favorable balance between heat transfer and drag.

To gain a deeper understanding of the mechanisms driving heat transfer enhancement, additional surface configurations must be investigated. A broader dataset would enable a more comprehensive analysis of how different roughness geometries influence the Nusselt number. In particular, the use of the equivalent sand-grain roughness in viscous units (k_s^+) can serve as a useful parameter to classify surfaces into different roughness regimes. This categorization would help to identify patterns or thresholds beyond which certain behaviors emerge. Ultimately, developing more refined correlations between k_s^+, Nu, and C_f is essential for guiding the design of surface roughness patterns that optimize thermal performance while minimizing drag penalties.

Chapter 5

Conclusions & Future Work

5.1   Conclusions

This thesis aimed at investigating the influence of surface roughness on flow behavior and heat transfer in turbine cooling ducts, with a particular focus on developing and validating experimental methodologies. The SRHT rig was upgraded and successfully validated through comparison with established literature correlations. In the final section of the test rig, both thermally and hydrodynamically fully developed conditions were achieved. A dedicated analysis was carried out to assess the effects of camera inclination, providing insights into local measurement uncertainties.

The thermal boundary layer was analyzed for both smooth and rough surfaces. A qualitative comparison with results from the PIV rig confirmed that the Nusselt number increases in regions of direct interaction between flow structures and roughness features, supported by corresponding changes in streamline patterns.

An extended roughness characterization framework was introduced to better interpret the surface-flow interaction. While S_z alone may be insufficient for a comprehensive description, the inclusion of roughness solidity parameters, such as frontal solidity λ_f, proved to be valuable in distinguishing between different flow regimes.

The various tests conducted throughout this study enabled the construction of a robust experimental database, which can serve as a foundation for future investigations. Further insights were gained by evaluating the thermal and velocity shift functions, $\Delta\theta^+$ and ΔU^+, which provided additional means to interpret the heat transfer mechanisms in relation to surface-induced flow behavior.

Finally, the Nusselt number and skin-friction coefficient were combined into a thermal performance factor (TPF), enabling a first assessment of surface roughness efficiency in terms of heat transfer enhancement relative to pressure losses.

5.2 Future Work

The SRHT rig study will be continued in the context of future master's theses, aiming to expand the experimental dataset and improve measurement fidelity. One key development will be the enhancement of the thermal boundary layer acquisition system to enable more accurate and spatially resolved temperature measurements. This will allow a more complete description of the momentum and thermal boundary layers, especially in the presence of complex roughness topologies.

Additional experiments in collaboration with the PIV rig are essential to deepen the understanding of the coupling between local flow behavior and thermal performance. To systematically investigate the role of specific surface parameters, artificially generated roughness patterns could be employed. These surfaces would allow the controlled variation of one geometrical property at a time while keeping others constant.

Moreover, considering that spurious infrared signals may compromise local heat transfer evaluations, a detailed study of IR radiation propagation within the channel, along with improvements to the image-mapping process, could significantly enhance the overall measurement accuracy.

Bibliography

[1] Hagen, *Über den Einfluss der Temperatur auf die Bewegung des Wassers in Röhren : (gelesen in der Akademie der Wissenschaften am 10. November 1853 und am 6. März 1854)*. [nicht ermittelbar], 1854. DOI: 10.3931/E-RARA-68624. (visited on 06/14/2025).

[2] H. Darcy, *Recherches expérimentales relatives au mouvement de l'eau dans les tuyaux par Henry Darcy: Texte*. Mallet-Bachelier, 1857.

[3] O. Reynolds, "An experimental investigation of the circumstances which determine whether the motion of water shall be direct or sinuous, and of the law of resistance in parallel channels," *Philosophical Transactions of the Royal Society of London*, vol. 174, pp. 935–982, Dec. 1883, ISSN: 0261-0523, 2053-9223. DOI: 10.1098/rstl.1883.0029. (visited on 06/11/2025).

[4] W. Sutherland, "The viscosity of gases and molecular force," *The London, Edinburgh, and Dublin Philosophical Magazine and Journal of Science*, vol. 36, no. 223, Dec. 1893, ISSN: 1941-5982, 1941-5990. DOI: 10.1080/14786449308620508. (visited on 06/10/2025).

[5] E. Buckingham, "On Physically Similar Systems; Illustrations of the Use of Dimensional Equations," *Physical Review*, vol. 4, no. 4, pp. 345–376, Oct. 1914, ISSN: 0031-899X. DOI: 10.1103/PhysRev.4.345. (visited on 06/12/2025).

[6] T. V. Kármán, *Mechanical Similitude and Turbulence*. National Advisory Committee for Aeronautics, 1931.

[7] H. Schlichting, "Experimentelle Untersuchungen zum Rauhigkeitsproblem," *Ingenieur-Archiv*, vol. 7, no. 1, pp. 1–34, Feb. 1936, ISSN: 0020-1154, 1432-0681. DOI: 10.1007/BF02084166. (visited on 06/11/2025).

[8] C. F. Colebrook and C. M. White, "Experiments with fluid friction in roughened pipes," *Proceedings of the Royal Society of London. Series A - Mathematical and Physical Sciences*, vol. 161, no. 906, pp. 367–381, Aug. 1937, ISSN: 0080-4630, 2053-9169. DOI: 10.1098/rspa.1937.0150. (visited on 06/10/2025).

[9] C. F. Colebrook, "TURBULENT FLOW IN PIPES, WITH PARTICULAR REFERENCE TO THE TRANSITION REGION BETWEEN THE SMOOTH AND ROUGH PIPE LAWS.," *Journal of the Institution of Civil Engineers*, vol. 11, no. 4, pp. 133–156, Feb. 1939, ISSN: 0368-2455. DOI: 10.1680/ijoti.1939.13150. (visited on 06/14/2025).

[10] W. F. Cope, "The Friction and Heat Transmission Coefficients of Rough Pipes," *Proceedings of the Institution of Mechanical Engineers*, vol. 145, no. 1, pp. 99–105,

Jun. 1941, ISSN: 0020-3483, 2058-1203. DOI: 10.1243/PIME_PROC_1941_145_026_02. (visited on 06/14/2025).

[11] L. F. Moody, "Friction Factors for Pipe Flow," *Journal of Fluids Engineering*, vol. 66, no. 8, pp. 671–678, Nov. 1944, ISSN: 0097-6822. DOI: 10.1115/1.4018140. (visited on 06/10/2025).

[12] J. Nikuradse, *Laws of Flow in Rough Pipes*. National Advisory Commitee for Aeronautics, 1950.

[13] F. H. Clauser, "Turbulent Boundary Layers in Adverse Pressure Gradients," *Journal of the Aeronautical Sciences*, vol. 21, no. 2, pp. 91–108, Feb. 1954, ISSN: 1936-9956. DOI: 10.2514/8.2938. (visited on 06/11/2025).

[14] F. R. Hama, "Boundary layer characteristics for smooth and rough surfaces," *Trans. Soc. Nav. Arch. Marine Engrs.*, vol. 62, pp. 333–358, 1954. (visited on 06/11/2025).

[15] R. Johnk and T. Hanratty, "Temperature profiles for turbulent flow of air in a pipe—II The thermal entrance region," *Chemical Engineering Science*, vol. 17, no. 11, pp. 881–892, Nov. 1962, ISSN: 00092509. DOI: 10.1016/0009-2509(62)87020-1. (visited on 04/18/2025).

[16] A. F. Mills, "Experimental Investigation of Turbulent Heat Transfer in the Entrance Region of a Circular Conduit," *Journal of Mechanical Engineering Science*, vol. 4, no. 1, pp. 63–77, Mar. 1962, ISSN: 0022-2542, 2058-3389. DOI: 10.1243/JMES_JOUR_1962_004_010_02. (visited on 02/21/2025).

[17] D. Dipprey and R. Sabersky, "Heat and momentum transfer in smooth and rough tubes at various prandtl numbers," *International Journal of Heat and Mass Transfer*, vol. 6, no. 5, pp. 329–353, May 1963, ISSN: 00179310. DOI: 10.1016/0017-9310(63)90097-8. (visited on 06/14/2025).

[18] A. L. Braslow, U. S. N. A. a. S. Administration, and L. R. Center, *A Review of Factors Affecting Boundary-layer Transition*. Washington, D.C., USA: National Aeronautics and Space Administration, 1966.

[19] R. Gowen and J. Smith, "The effect of the Prandtl number on temperature profiles for heat transfer in turbulent pipe flow," *Chemical Engineering Science*, vol. 22, no. 12, pp. 1701–1711, Dec. 1967, ISSN: 00092509. DOI: 10.1016/0009-2509(67)80205-7. (visited on 04/16/2025).

[20] A. E. Perry, W. H. Schofield, and P. N. Joubert, "Rough wall turbulent boundary layers," *Journal of Fluid Mechanics*, vol. 37, no. 2, pp. 383–413, Jun. 1969, ISSN: 0022-1120, 1469-7645. DOI: 10.1017/S0022112069000619. (visited on 06/30/2025).

[21] B. Kader and A. Yaglom, "Heat and mass transfer laws for fully turbulent wall flows," *International Journal of Heat and Mass Transfer*, vol. 15, no. 12, pp. 2329–2351, Dec. 1972, ISSN: 00179310. DOI: 10.1016/0017-9310(72)90131-7. (visited on 04/16/2025).

[22] T. Mizushina, T. Matsumoto, and S. Yoneda, "The effect of large temperature difference on the turbulent heat and momentum transfer in an air flow inside a circular tube.," *JOURNAL OF CHEMICAL ENGINEERING OF JAPAN*, vol. 9,

no. 6, pp. 450–457, 1976, ISSN: 0021-9592, 1881-1299. DOI: 10.1252/jcej.9.450. (visited on 04/18/2025).

[23] M. Dalle Donne and L. Meyer, "Turbulent convective heat transfer from rough surfaces with two-dimensional rectangular ribs," *International Journal of Heat and Mass Transfer*, vol. 20, no. 6, pp. 583–620, Jun. 1977, ISSN: 00179310. DOI: 10.1016/0017-9310(77)90047-3. (visited on 06/14/2025).

[24] H. Schlichting, *Boundary-Layer Theory* (McGraw-Hill Series in Mechanical Engineering), 7. ed. New York: McGraw-Hill, 1979, ISBN: 978-0-07-055334-7.

[25] B. Kader, "Temperature and concentration profiles in fully turbulent boundary layers," *International Journal of Heat and Mass Transfer*, vol. 24, no. 9, pp. 1541–1544, Sep. 1981, ISSN: 00179310. DOI: 10.1016/0017-9310(81)90220-9. (visited on 04/16/2025).

[26] W. Zhi-qing, "Study on correction coefficients of liminar and turbulent entrance region effect in round pipe," *Applied Mathematics and Mechanics*, vol. 3, no. 3, pp. 433–446, Jun. 1982, ISSN: 0253-4827, 1573-2754. DOI: 10.1007/BF01897224. (visited on 06/11/2025).

[27] D. E. Metzger and D. E. Larson, "Use of Melting Point Surface Coatings for Local Convection Heat Transfer Measurements in Rectangular Channel Flows With 90-deg Turns," *Journal of Heat Transfer*, vol. 108, no. 1, pp. 48–54, Feb. 1986, ISSN: 0022-1481, 1528-8943. DOI: 10.1115/1.3246903. (visited on 06/18/2025).

[28] W. M. Kays and M. E. Crawford, *Convective Heat and Mass Transfer* (McGraw-Hill Series in Mechanical Engineering), 3rd ed. New York St. Louis Paris [etc.]: McGraw-Hill, 1993, ISBN: 978-0-07-033721-3.

[29] L. Glicksman, M. Hyre, and P. Farrell, "Dynamic similarity in fluidization," *International Journal of Multiphase Flow*, vol. 20, pp. 331–386, Aug. 1994, ISSN: 03019322. DOI: 10.1016/0301-9322(94)90077-9. (visited on 06/12/2025).

[30] W. M. Rohsenow, J. P. Hartnett, and Y. I. Cho, Eds., *Handbook of Heat Transfer* (McGraw-Hill Handbooks), 3rd ed. Chicago, Ill: McGraw-Hill Education LLC, 1998, ISBN: 978-0-07-053555-8.

[31] T. Astarita, G. Cardone, G. Carlomagno, and C. Meola, "A survey on infrared thermography for convective heat transfer measurements," *Optics & Laser Technology*, vol. 32, no. 7-8, pp. 593–610, Oct. 2000, ISSN: 00303992. DOI: 10.1016/S0030-3992(00)00086-4. (visited on 06/09/2025).

[32] H. I. H. Saravanamuttoo, G. F. C. Rogers, H. Cohen, H. I. H. Saravanamuttoo, and G. F. C. Rogers, *Gas Turbine Theory*, 5. ed. Harlow: Prentice Hall, 2001, ISBN: 978-0-13-015847-5.

[33] M. P. Boyce, *Gas Turbine Engineering Handbook*, 2nd ed. Boston, MA: Gulf Professional Pub, 2002, ISBN: 978-0-88415-732-8.

[34] E. Gadelmawla, M. Koura, T. Maksoud, I. Elewa, and H. Soliman, "Roughness parameters," *Journal of Materials Processing Technology*, vol. 123, no. 1, pp. 133–145, Apr. 2002, ISSN: 09240136. DOI: 10.1016/S0924-0136(02)00060-2. (visited on 06/07/2025).

[35] M. P. Schultz, J. A. Finlay, M. E. Callow, and J. A. Callow, "Three Models to Relate Detachment of Low Form Fouling at Laboratory and Ship Scale," *Bio-*

fouling, vol. 19, no. sup1, pp. 17–26, Jan. 2003, ISSN: 0892-7014, 1029-2454. DOI: 10.1080/0892701031000089516. (visited on 06/11/2025).

[36] J. Jiménez, "Turbolent Flows Over Rough Walls," *Annual Review of Fluid Mechanics*, vol. 36, no. 1, pp. 173–196, Jan. 2004, ISSN: 0066-4189, 1545-4479. DOI: 10.1146/annurev.fluid.36.050802.122103. (visited on 06/30/2025).

[37] J. D. Anderson, "Ludwig Prandtl's Boundary Layer," *Physics Today*, vol. 58, no. 12, pp. 42–48, Dec. 2005, ISSN: 0031-9228, 1945-0699. DOI: 10.1063/1.2169443. (visited on 06/10/2025).

[38] F. E. Jørgensen, "How to measure turbulence with hot-wire anemometers," Aug. 2005.

[39] Y. A. Çengel and M. A. Boles, *Thermodynamics: An Engineering Approach* (McGraw-Hill Series in Mechanical Engineering), 5. ed. Boston, Mass.: McGraw-Hill Higher Education, 2006, ISBN: 978-0-07-288495-1 978-0-07-310768-4 978-0-07-288498-2.

[40] J.-C. Han, "Turbine Blade Cooling Studies at Texas A&M University: 1980-2004," *Journal of Thermophysics and Heat Transfer*, vol. 20, no. 2, pp. 161–187, Apr. 2006, ISSN: 0887-8722, 1533-6808. DOI: 10.2514/1.15403. (visited on 06/06/2025).

[41] S. E. Coleman, V. I. Nikora, S. R. McLean, and E. Schlicke, "Spatially Averaged Turbulent Flow over Square Ribs," *Journal of Engineering Mechanics*, vol. 133, no. 2, pp. 194–204, Feb. 2007, ISSN: 0733-9399, 1943-7889. DOI: 10.1061/(ASCE)0733-9399(2007)133:2(194). (visited on 06/30/2025).

[42] F. P. Incropera and F. P. Incropera, Eds., *Fundamentals of Heat and Mass Transfer*, 6th ed. Hoboken, NJ: John Wiley, 2007, ISBN: 978-0-471-45728-2.

[43] C. P. Kothandaraman, *Fundamentals of Heat and Mass Transfer*, 3., rev. ed., repr. New Delhi: Wiley Eastern, 2007, ISBN: 978-81-224-1772-2.

[44] F. Liebmann, "Infrared calibration development at Fluke Corporation Hart Scientific Division," in *SPIE Defense and Security Symposium*, V. P. Vavilov and D. D. Burleigh, Eds., Orlando, FL, Mar. 2008, p. 693906. DOI: 10.1117/12.781510. (visited on 06/17/2025).

[45] P. Ajersch, "Detailed measurements on a row of jets in a crossflow : With applications," 2009. DOI: 10.14288/1.0081025. (visited on 06/06/2025).

[46] "Dias cs110," (DIAS Infrared GmbH), Jan. 2009. [Online]. Available: https://dias-infrared.de/pdf/cs110_ger.pdf (visited on 06/17/2025).

[47] L. Prandtl and A. Betz, Eds., *Ergebnisse Der Aerodynamischen Versuchsanstalt Zu Göttingen - IV. Lieferung* (Göttinger Klassiker Der Strömungmechanik). Göttingen: Göttingen University Press, 2009, vol. 7, ISBN: 978-3-941875-42-5. DOI: 10.17875/gup2009-104. (visited on 06/11/2025).

[48] J. P. Bons, "A Review of Surface Roughness Effects in Gas Turbines," *Journal of Turbomachinery*, vol. 132, no. 2, p. 021004, Apr. 2010, ISSN: 0889-504X, 1528-8900. DOI: 10.1115/1.3066315. (visited on 06/14/2025).

[49] K. A. Flack and M. P. Schultz, "Review of Hydraulic Roughness Scales in the Fully Rough Regime," *Journal of Fluids Engineering*, vol. 132, no. 4, p. 041203,

Apr. 2010, ISSN: 0098-2202, 1528-901X. DOI: 10.1115/1.4001492. (visited on 04/15/2025).

[50] M. Vollmer and K.-P. Möllmann, *Infrared Thermal Imaging: Fundamentals, Research and Applications*, 1st ed. Wiley, Aug. 2010, ISBN: 978-3-527-40717-0 978-3-527-63086-8. DOI: 10.1002/9783527630868. (visited on 06/09/2025).

[51] J. D. Anderson, *Fundamentals of Aerodynamics* (McGraw-Hill Series in Aeronautical and Aerospace Engineering), 5. ed. in SI Units. New York, NY: McGraw-Hill, 2011, ISBN: 978-0-07-339810-5 978-1-259-01028-6 978-0-07-128908-5.

[52] J. Hong, J. Katz, and M. P. Schultz, "Near-wall turbulence statistics and flow structures over three-dimensional roughness in a turbulent channel flow," *Journal of Fluid Mechanics*, vol. 667, pp. 1–37, Jan. 2011, ISSN: 0022-1120, 1469-7645. DOI: 10.1017/S0022112010003988. (visited on 06/14/2025).

[53] M. Rahman, T. K. Ibrahim, K. Kadirgama, R. Mamat, and R. A. Bakar, "Influence of Operation Conditions and Ambient Temperature on Performance of Gas Turbine Power Plant," *Advanced Materials Research*, vol. 189–193, pp. 3007–3013, Feb. 2011, ISSN: 1662-8985. DOI: 10.4028/www.scientific.net/AMR.189-193.3007. (visited on 06/06/2025).

[54] T. J. Horn and O. L. A. Harrysson, "Overview of Current Additive Manufacturing Technologies and Selected Applications," *Science Progress*, vol. 95, no. 3, Sep. 2012, ISSN: 0036-8504, 2047-7163. DOI: 10.3184/003685012X13420984463047. (visited on 06/06/2025).

[55] B. Lane, E. Whitenton, V. Madhavan, and A. Donmez, "Uncertainty of temperature measurements by infrared thermography for metal cutting applications," *Metrologia*, vol. 50, no. 6, pp. 637–653, Dec. 2013, ISSN: 0026-1394, 1681-7575. DOI: 10.1088/0026-1394/50/6/637. (visited on 06/17/2025).

[56] S. Saha, J. Klewicki, A. Ooi, H. Blackburn, and T. Wei, "Scaling properties of the equation for passive scalar transport in wall-bounded turbulent flows," *International Journal of Heat and Mass Transfer*, vol. 70, pp. 779–792, Mar. 2014, ISSN: 00179310. DOI: 10.1016/j.ijheatmasstransfer.2013.11.057. (visited on 04/19/2025).

[57] L. Ventola *et al.*, "Rough surfaces with enhanced heat transfer for electronics cooling by direct metal laser sintering," *International Journal of Heat and Mass Transfer*, vol. 75, pp. 58–74, Aug. 2014, ISSN: 00179310. DOI: 10.1016/j.ijheatmasstransfer.2014.03.037. (visited on 06/14/2025).

[58] Y. A. Çengel and A. J. Ghajar, *Heat and Mass Transfer: Fundamentals & Applications*, 5th edition. New York, NY: McGraw-Hill Education, 2015, ISBN: 978-0-07-339818-1.

[59] S. Leonardi, P. Orlandi, L. Djenidi, and R. A. Antonia, "Heat transfer in a turbulent channel flow with square bars or circular rods on one wall," *Journal of Fluid Mechanics*, vol. 776, pp. 512–530, Aug. 2015, ISSN: 0022-1120, 1469-7645. DOI: 10.1017/jfm.2015.344. (visited on 06/07/2025).

[60] D. Herzog, V. Seyda, E. Wycisk, and C. Emmelmann, "Additive manufacturing of metals," *Acta Materialia*, vol. 117, pp. 371–392, Sep. 2016, ISSN: 13596454. DOI: 10.1016/j.actamat.2016.07.019. (visited on 06/06/2025).

[61] B. M. Lane and E. P. Whitenton, "Calibration and Measurement Procedures for a High Magnification Thermal Camera," National Institute of Standards and Technology, Tech. Rep. NIST IR 8098, Jan. 2016, NIST IR 8098. DOI: 10.6028/NIST.IR.8098. (visited on 01/06/2025).

[62] W. Minkina and D. Klecha, "Atmospheric transmission coefficient modelling in the infrared for thermovision measurements," *Journal of Sensors and Sensor Systems*, vol. 5, no. 1, pp. 17–23, Jan. 2016, ISSN: 2194-878X. DOI: 10.5194/jsss-5-17-2016. (visited on 01/23/2025).

[63] J. C. Snyder, C. K. Stimpson, K. A. Thole, and D. Mongillo, "Build Direction Effects on Additively Manufactured Channels," *Journal of Turbomachinery*, vol. 138, no. 5, p. 051006, May 2016, ISSN: 0889-504X, 1528-8900. DOI: 10.1115/1.4032168. (visited on 06/14/2025).

[64] C. K. Stimpson, J. C. Snyder, K. A. Thole, and D. Mongillo, "Roughness Effects on Flow and Heat Transfer for Additively Manufactured Channels," *Journal of Turbomachinery*, vol. 138, no. 5, p. 051008, May 2016, ISSN: 0889-504X, 1528-8900. DOI: 10.1115/1.4032167. (visited on 03/23/2025).

[65] A. Townsend, N. Senin, L. Blunt, R. Leach, and J. Taylor, "Surface texture metrology for metal additive manufacturing: A review," *Precision Engineering*, vol. 46, pp. 34–47, Oct. 2016, ISSN: 01416359. DOI: 10.1016/j.precisioneng.2016.06.001. (visited on 06/14/2025).

[66] S. Brack, R. Poser, and J. V. Wolfersdorf, *A comparison between transient heat transfer measurements using TLC and IR thermography*, 2017. DOI: 10.18419/OPUS-9723. (visited on 06/16/2025).

[67] P. Jaksch, "Implementation of an adjoint thermal solver for inverse problems," in *European Conference on Turbomachinery Fluid Dynamics and Hermodynamics*, Stockholm, Sweden, 2017. DOI: 10.29008/ETC2017-336. (visited on 06/18/2025).

[68] A. V. Singh and R. R. Singh, "Turbine blade cooling techniques," *INTERNATIONAL JOURNAL OF RESEARCH IN AERONAUTICAL AND MECHANICAL ENGINEERING*, vol. 5, no. 5, 2017, ISSN: 2321-3051. (visited on 06/06/2025).

[69] C. K. Stimpson, J. C. Snyder, K. A. Thole, and D. Mongillo, "Scaling Roughness Effects on Pressure Loss and Heat Transfer of Additively Manufactured Channels," *Journal of Turbomachinery*, vol. 139, no. 2, p. 021003, Feb. 2017, ISSN: 0889-504X, 1528-8900. DOI: 10.1115/1.4034555. (visited on 11/19/2024).

[70] J.-M. Clemenson, T. A. Shannon, and S. T. McClain, "A Novel Method for Constructing Analog Roughness Patterns to Replicate Ice Accretion Characteristics," in *2018 Atmospheric and Space Environments Conference*, Atlanta, Georgia: American Institute of Aeronautics and Astronautics, Jun. 2018, ISBN: 978-1-62410-558-6. DOI: 10.2514/6.2018-3015. (visited on 06/17/2025).

[71] H. W. Coleman and W. G. Steele, *Experimentation, Validation, and Uncertainty Analysis for Engineers*, 1st ed. Wiley, May 2018, ISBN: 978-1-119-41751-4 978-1-119-41798-9. DOI: 10.1002/9781119417989. (visited on 06/20/2025).

[72] P. Forooghi, A. Stroh, P. Schlatter, and B. Frohnapfel, "Direct numerical simulation of flow over dissimilar, randomly distributed roughness elements: A systematic study on the effect of surface morphology on turbulence," *Physi-*

cal Review Fluids, vol. 3, no. 4, p. 044 605, Apr. 2018, ISSN: 2469-990X. DOI: 10.1103/PhysRevFluids.3.044605. (visited on 06/07/2025).

[73] M. P. S. Patil and B. Dr. Sachin Lotan, "Recent Studies in Internal Cooling of gas turbine blade: A Review," vol. 13, no. 9, 2018. (visited on 06/06/2025).

[74] S. A. Tofail, E. P. Koumoulos, A. Bandyopadhyay, S. Bose, L. O'Donoghue, and C. Charitidis, "Additive manufacturing: Scientific and technological challenges, market uptake and opportunities," *Materials Today*, vol. 21, no. 1, pp. 22–37, Jan. 2018, ISSN: 13697021. DOI: 10.1016/j.mattod.2017.07.001. (visited on 06/06/2025).

[75] D. R. Hanson, S. T. McClain, J. C. Snyder, R. F. Kunz, and K. A. Thole, "Flow in a Scaled Turbine Coolant Channel With Roughness due to Additive Manufacturing," in *Volume 5B: Heat Transfer*, Phoenix, Arizona, USA: American Society of Mechanical Engineers, Jun. 2019, V05BT21A004, ISBN: 978-0-7918-5865-3. DOI: 10.1115/GT2019-90931. (visited on 06/14/2025).

[76] J. Peeters and N. Sandham, "Turbulent heat transfer in channels with irregular roughness," *International Journal of Heat and Mass Transfer*, vol. 138, pp. 454–467, Aug. 2019, ISSN: 00179310. DOI: 10.1016/j.ijheatmasstransfer.2019.04.013. (visited on 06/14/2025).

[77] S. Taylor, E. C. Forrest, and B. H. Jared, "Investigating Applicability of Surface Roughness Parameters in Describing the Metallic Additive Manufacturing Process.," in *Sandia National Lab. (SNL-NM)*, Albuquerque, NM (United States), Aug. 2019.

[78] American Society of Mechanical Engineers, Ed., *Surface Texture: (Surface Roughness, Waviness, and Lay): An International Standard* (ASME B46.1-2019). New York, NY: The American Society of Mechanical Engineers, Jun. 2020, ISBN: 978-0-7918-7325-0.

[79] S. Han, F. Salvatore, J. Rech, and J. Bajolet, "Abrasive flow machining (AFM) finishing of conformal cooling channels created by selective laser melting (SLM)," *Precision Engineering*, vol. 64, pp. 20–33, Jul. 2020, ISSN: 01416359. DOI: 10.1016/j.precisioneng.2020.03.006. (visited on 06/14/2025).

[80] A. Razavykia, E. Brusa, C. Delprete, and R. Yavari, "An Overview of Additive Manufacturing Technologies—A Review to Technical Synthesis in Numerical Study of Selective Laser Melting," *Materials*, vol. 13, no. 17, p. 3895, Sep. 2020, ISSN: 1996-1944. DOI: 10.3390/ma13173895. (visited on 06/06/2025).

[81] N.-E. Sad Chemloul, *Dimensional Analysis and Similarity in Fluid Mechanics*. Newark: John Wiley & Sons, Incorporated, 2020, ISBN: 978-1-119-78803-4.

[82] J. C. Snyder and K. A. Thole, "Understanding Laser Powder Bed Fusion Surface Roughness," *Journal of Manufacturing Science and Engineering*, vol. 142, no. 7, p. 071 003, Jul. 2020, ISSN: 1087-1357, 1528-8935. DOI: 10.1115/1.4046504. (visited on 06/13/2025).

[83] N. Van De Werken, H. Tekinalp, P. Khanbolouki, S. Ozcan, A. Williams, and M. Tehrani, "Additively manufactured carbon fiber-reinforced composites: State of the art and perspective," *Additive Manufacturing*, vol. 31, p. 100 962, Jan. 2020, ISSN: 22148604. DOI: 10.1016/j.addma.2019.100962. (visited on 06/06/2025).

[84]   C. Zhang, S. Wang, J. Li, Y. Zhu, T. Peng, and H. Yang, "Additive manufacturing of products with functional fluid channels: A review," *Additive Manufacturing*, vol. 36, p. 101 490, Dec. 2020, ISSN: 22148604. DOI: 10.1016/j.addma.2020.101490. (visited on 06/13/2025).

[85]   J. Zhang, S. Zhang, C. Wang, and X. Tan, "Recent advances in film cooling enhancement: A review," *Chinese Journal of Aeronautics*, vol. 33, no. 4, pp. 1119–1136, Apr. 2020, ISSN: 10009361. DOI: 10.1016/j.cja.2019.12.023. (visited on 06/06/2025).

[86]   D. Chung, N. Hutchins, M. P. Schultz, and K. A. Flack, "Predicting the Drag of Rough Surfaces," *Annual Review of Fluid Mechanics*, vol. 53, no. 1, pp. 439–471, Jan. 2021, ISSN: 0066-4189, 1545-4479. DOI: 10.1146/annurev-fluid-062520-115127. (visited on 03/02/2025).

[87]   K. Dziarski and A. Hulewicz, "Determination of Transmittance of IR Windows made of CaF2 within Operational Temperatures of Electric Devices," *Pomiary Automatyka Robotyka*, vol. 25, no. 4, pp. 25–30, Dec. 2021, ISSN: 14279126. DOI: 10.14313/PAR_242/25. (visited on 01/23/2025).

[88]   M. Kadivar, D. Tormey, and G. McGranaghan, "A review on turbulent flow over rough surfaces: Fundamentals and theories," *International Journal of Thermofluids*, vol. 10, p. 100 077, May 2021, ISSN: 26662027. DOI: 10.1016/j.ijft.2021.100077. (visited on 11/18/2024).

[89]   H. Ritchie, "How have the world's energy sources changed over the last two centuries?" *Our World in Data*, 2021. [Online]. Available: https://ourworldindata.org/global-energy-200-years.

[90]   A. Salama, "Velocity Profile Representation for Fully Developed Turbulent Flows in Pipes: A Modified Power Law," *Fluids*, vol. 6, no. 10, p. 369, Oct. 2021, ISSN: 2311-5521. DOI: 10.3390/fluids6100369. (visited on 06/11/2025).

[91]   SiemensEnergy-AB. "Sgt-800 industrial gas turbine." (2021), [Online]. Available: https://www.siemens-energy.com/global/en/home/products-services/product/sgt-800.html (visited on 06/05/2025).

[92]   SiemensEnergy-AB. "Sgt6-9000hl heavy-duty gas turbine." (2021), [Online]. Available: http://siemens-energy.com/global/en/home/products-services/product/sgt5-9000hl.html (visited on 06/05/2025).

[93]   R. Subramanian, D. Rule, and O. Nazik, "Dependence of LPBF Surface Roughness on Laser Incidence Angle and Component Build Orientation," in *Volume 7: Industrial and Cogeneration; Manufacturing Materials and Metallurgy*, Virtual, Online: American Society of Mechanical Engineers, Jun. 2021, V007T17A015, ISBN: 978-0-7918-8500-0. DOI: 10.1115/GT2021-59755. (visited on 06/07/2025).

[94]   X. Yang, R. A. Barrett, N. M. Harrison, and S. B. Leen, "A physically-based structure-property model for additively manufactured Ti-6Al-4V," *Materials & Design*, vol. 205, p. 109 709, Jul. 2021, ISSN: 02641275. DOI: 10.1016/j.matdes.2021.109709. (visited on 06/06/2025).

[95]   K. Yeranee and Y. Rao, "A review of recent studies on rotating internal cooling for gas turbine blades," *Chinese Journal of Aeronautics*, vol. 34, no. 7, pp. 85–

113, Jul. 2021, ISSN: 10009361. DOI: 10.1016/j.cja.2020.12.035. (visited on 06/06/2025).

[96] "BM-CHE-S204-Heat Transfer," (UIET CSJM University), Jan. 2022. [Online]. Available: https://gyansanchay.csjmu.ac.in/wp-content/uploads/2022/01/CHE-S204-Chapter-8-Radiation_G2.pdf (visited on 06/09/2025).

[97] ISO, *Geometrical product specifications (GPS) — Surface texture: Profile*, ISO 21920-2:2021, Jun. 2022.

[98] S. R. Narasimharaju *et al.*, "A comprehensive review on laser powder bed fusion of steels: Processing, microstructure, defects and control methods, mechanical properties, current challenges and future trends," *Journal of Manufacturing Processes*, vol. 75, pp. 375–414, Mar. 2022, ISSN: 15266125. DOI: 10.1016/j.jmapro.2021.12.033. (visited on 06/06/2025).

[99] R. Pagani, "Experimental Analysis of the Thermal and Hydraulic Performance in Straight and Complex Additively Manufactured Mini-Channels," Ph.D. dissertation, Politecnico di Milano, Milano, Italy, 2022.

[100] U. Unnikrishnan and V. Yang, "A review of cooling technologies for high temperature rotating components in gas turbine," *Propulsion and Power Research*, vol. 11, no. 3, pp. 293–310, Sep. 2022, ISSN: 2212540X. DOI: 10.1016/j.jppr.2022.07.001. (visited on 06/06/2025).

[101] G. Zhang, R. Zhu, G. Xie, S. Li, and B. Sundén, "Optimization of cooling structures in gas turbines: A review," *Chinese Journal of Aeronautics*, vol. 35, no. 6, pp. 18–46, Jun. 2022, ISSN: 10009361. DOI: 10.1016/j.cja.2021.08.029. (visited on 06/06/2025).

[102] T. S. Chowdhury, F. T. Mohsin, M. M. Tonni, M. N. H. Mita, and M. M. Ehsan, "A critical review on gas turbine cooling performance and failure analysis of turbine blades," *International Journal of Thermofluids*, vol. 18, p. 100 329, May 2023, ISSN: 26662027. DOI: 10.1016/j.ijft.2023.100329. (visited on 06/06/2025).

[103] P. V. Lehmann, "Investigation of the Local Heat Transfer Characteristics on Additively Manufactured Surfaces Using Infrared Thermography," Ph.D. dissertation, Technical University of Munich, Munich, Germany, Jan. 2023.

[104] C. Venturi, "Investigation of Thermal Performance of AM Channels and the Influence of the Printing Angle.," Ph.D. dissertation, Politecnico di Torino, Torino, Italy, 2023.

[105] K. Wen, "Investigation of Roughness Effects on Heat Transfer of Upscaled Additively Manufactured Channels in the Turbulent Region Using Infrared Thermography," Ph.D. dissertation, KTH, Stockholm, Sweden, 2023.

[106] A. Brogliato, "Investigation of the Effect of Additive Manufacturing Induced Surface Roughness on Local Heat Transfer Properties Using IR Thermography," Ph.D. dissertation, Politecnico di Torino, Torino, Italy, Jul. 2024.

[107] A. Brugnera, "Experimental investigation of heat transfer in additive manufactured channels with different Prandtl.," Ph.D. dissertation, Politecnico di Torino, Torino, Italy, Oct. 2024.

[108] H. Garg, G. Sahut, E. Tuneskog, K.-J. Nogenmyr, and C. Fureby, "Large eddy simulations of flow over additively manufactured surfaces: Impact of rough-

ness and skewness on turbulent heat transfer," *Physics of Fluids*, vol. 36, no. 8, p. 085 143, Aug. 2024, ISSN: 1070-6631, 1089-7666. DOI: 10.1063/5.0221006. (visited on 03/11/2025).

[109] H. Garg, L. Wang, and C. Fureby, "Heat transfer enhancement with additively manufactured rough surfaces: Insights from large-eddy simulations," *Physics of Fluids*, vol. 36, no. 2, p. 025 109, Feb. 2024, ISSN: 1070-6631, 1089-7666. DOI: 10.1063/5.0189115. (visited on 03/11/2025).

[110] Q. Mi, S. Yi, D. Gang, X. Lu, and X. Liu, "Research progress of transpiration cooling for aircraft thermal protection," *Applied Thermal Engineering*, vol. 236, p. 121 360, Jan. 2024, ISSN: 13594311. DOI: 10.1016/j.applthermaleng.2023.121360. (visited on 06/06/2025).

[111] A. Pedreño Marin, "PIV flow measurements for heat transfer characterization in upscaled AM surface roughness," Ph.D. dissertation, TU Delft, Delft. Netherlands, Nov. 2024.

[112] S. Pirozzoli and D. Modesti, "Mean temperature profiles in turbulent internal flows," *International Journal of Heat and Fluid Flow*, vol. 109, p. 109 544, Oct. 2024, ISSN: 0142727X. DOI: 10.1016/j.ijheatfluidflow.2024.109544. (visited on 03/09/2025).

[113] S. Pourrahimi and L. A. Hof, "On the Post-Processing of Complex Additive Manufactured Metallic Parts: A Review," *Advanced Engineering Materials*, vol. 26, no. 10, p. 2 301 511, May 2024, ISSN: 1438-1656, 1527-2648. DOI: 10.1002/adem.202301511. (visited on 06/07/2025).

[114] C. Tamagnini and F. Agostino, "Thermo-fluid dynamic characterization of an additive manufactured rough channel and development of an experimental PIV apparatus," Ph.D. dissertation, Politecnico di Milano, Milano, Italy, 2024.

[115] L. Zhou *et al.*, "Additive Manufacturing: A Comprehensive Review," *Sensors*, vol. 24, no. 9, p. 2668, Apr. 2024, ISSN: 1424-8220. DOI: 10.3390/s24092668. (visited on 06/06/2025).

[116] ZygoCorporation. "Roughness measurements - let's take a closer look." (Sep. 12, 2024), [Online]. Available: https://www.zygo.com/insights/blog-posts/roughness-measurements (visited on 06/07/2025).

[117] M. Kadivar and H. Garg, "Turbulent Heat Transfer over roughness: A comprehensive review of theories and turbulent flow structure," *International Journal of Thermofluids*, vol. 26, p. 100 967, Mar. 2025, ISSN: 26662027. DOI: 10.1016/j.ijft.2024.100967. (visited on 02/21/2025).

[118] M. Laguardia, "Impact of AM-induced upscaled surface roughness on flow dynamics, heat transfer and friction properties: A particle image velocimetry study," Ph.D. dissertation, Politecnico di Torino, Torino, Italy, Jul. 2025.

[119] Thermalytica. "Thermal barrier coating service." (2025), [Online]. Available: https://www.thermalytica.com/coating-service-en/ (visited on 06/06/2025).

[120] "Turbine cooling group," (Oxford Thermofluids Institute), 2025. [Online]. Available: https://oti.eng.ox.ac.uk/research/research-groups/turbine-cooling-group/ (visited on 06/06/2025).

Appendix A

Dimensional Analysis

In the development of technical applications, it is often necessary to conduct experimental investigations on a scaled model before the actual product can be fabricated. However, the conditions under which such experiments are performed frequently differ from real-world operating conditions, such as geometry, temperature, or working fluid properties [81]. In such cases, dimensional analysis and similarity theory become essential tools.

Dimensional analysis enables a reduction in the number of independent variables governing a physical problem [29]. By applying established techniques, such as the Buckingham π-theorem [5], or through non-dimensionalization of governing equations, dimensionless correlations can be derived. These correlations are generally valid across a wide range of operating conditions and geometries, making them valuable for practical engineering applications [81].

The primary benefit of dimensional analysis in applied sciences lies in its ability to establish scaling laws between a physical system and its model, such that both exhibit *dynamic similarity*. This requires that the systems be geometrically similar (i.e. all linear dimensions must be scaled by a constant factor and all angles preserved) and that all relevant independent dimensionless numbers match [29]. Consequently, the dependent dimensionless quantities will also be comparable.

In this work, dimensional analysis and similarity principles were employed to ensure that experimental measurements conducted under laboratory conditions can be meaningfully extrapolated to real-scale turbine cooling channel applications.

A.1   Flow Properties

In this section, all the thermodynamic equations and underlying assumptions used in the data analysis are presented and described.

The "ideal gas" assumption has been adopted in the present work to evaluate the air

properties under all test conditions:

$$p = \rho R T \qquad \text{with} \quad R = 287.05\,\text{J/(kg\,K)}$$

A.1.1 Dimensionless Parameters

A.1.1.1 Bulk Velocity

For a general-section duct, the average (bulk) velocity is defined as:

$$\overline{U} = \frac{\int_A \rho u\, dA}{\rho A} = \frac{\dot{m}}{\rho A}$$

In this work, for clarity and generality, the bulk velocity $\overline{U}$ in an internal channel and the free-stream velocity u_∞ over a flat plate are treated as equivalent in the context of boundary layer development.

A.1.1.2 Reynolds Number

The *Reynolds number* quantifies the ratio between inertial and viscous forces in a fluid. For internal flows, it is defined as:

$$Re_D = \frac{\overline{U} D_h}{\nu}$$

In this study, it is also expressed using the continuity equation ($\dot{m} = \rho A u_\infty$):

$$Re_D = \frac{\dot{m} D_h}{A \mu}$$

Since the test channel has a non-circular cross-section, the hydraulic diameter D_h is introduced:

$$D_h = 4\frac{A}{P}$$

where A is the cross-sectional area and P is the wetted perimeter of the duct.

A.1.1.3 Dynamic Viscosity

The dynamic viscosity μ depends on temperature and is calculated using Sutherland's law [4]:

$$\frac{\mu}{\mu_0} = \left(\frac{T}{T_0}\right)^{3/2} \frac{T_0 + S_\mu}{T + S_\mu} \qquad \text{with} \quad \begin{cases} \mu_0 = 1.716 \cdot 10^{-5}\,\text{Ns/m}^2 \\ T_0 = 273.15\,\text{K} \\ S_\mu = 110.56\,\text{K} \end{cases}$$

A.1.1.4 Prandtl Number

The *Prandtl number* is defined as the ratio of momentum diffusivity (kinematic viscosity ν) to thermal diffusivity α. Physically, it reflects the ratio between momentum and heat transport capability. When $\mathrm{Pr} \approx 1$, the velocity and thermal boundary layers tend to coincide:

$$\mathrm{Pr} = \frac{\nu}{\alpha} = \frac{\left(\frac{\mu}{\rho}\right)}{\left(\frac{k}{\rho c_p}\right)} = \frac{c_p \mu}{k_{\mathrm{air}}}$$

In this work, given the relatively small variation in fluid temperature, a constant Prandtl number of $\mathrm{Pr} = 0.71$ is assumed.

A.1.1.5 Stanton Number

The *Stanton number* relates the heat transfer coefficient to the thermal and flow properties of the fluid:

$$St = \frac{h}{\rho c_p u_\infty} = \frac{Nu}{Re_L\, Pr}$$

A.1.1.6 Thermal Conductivity

The thermal conductivity of air is evaluated using the modified Eucken correlation, where c_v is the specific heat at constant volume:

$$k_{\mathrm{air}} = \mu c_v \left(1.32 + 1.77\, \frac{R}{c_v}\right) \qquad \text{with} \quad c_v = 720\,\mathrm{J/(kg\,K)}$$

A.1.1.7 Nusselt Number

The *Nusselt number* represents the ratio of convective to pure conductive heat transfer:

$$Nu = \frac{hL}{k} = \frac{hD_h}{k_{\mathrm{air}}}$$

For forced convection where viscous dissipation and compressibility are negligible, the Nusselt number is typically expressed as a function of Reynolds and Prandtl numbers:

$$Nu = f\,(Re, Pr)$$

A.2 Buckingham Theorem

Dimensional analysis is grounded in the principle of *dimensional homogeneity*, which must be satisfied when expressing mathematical relationships involving dimensional physical quantities. This principle states that:

The dimensional physical quantities on both sides of an equation must combine such a way that the resulting dimensions are consistent.

For instance, in a dimensional equation of the form $X + Y + Z = W$, all quantities (X, Y, Z, and W) must have the same dimensional representation. The same expression can be reformulated in a dimensionless form by dividing all terms by one of the quantities, for example W, yielding:

$$\frac{X}{W} + \frac{Y}{W} + \frac{Z}{W} = 1$$

This transformation reduces the number of independent variables from four to three and introduces dimensionless quantities.

Each dimensional physical quantity can be expressed using fundamental units. The most common sets of base quantities are the International System (SI) and the Technical System, summarized in Table A.1:

International System		Technical System	
Length	**L**	Length	**L**
Mass	**M**	Force	**F**
Time	**T**	Time	**T**

Table A.1: Comparison between International System and Technical System

The *Buckingham π-theorem* offers a powerful framework for simplifying complex physical problems by reducing the number of governing parameters. It enables the identification of dimensionless groups, referred to as π terms, based on the dimensional analysis of the original physical variables.

Suppose a physical phenomenon is described by N dimensional quantities:

$$Q_1, Q_2, Q_3, \ldots, Q_N$$

Each quantity can be expressed using K fundamental physical dimensions (e.g., Length, Mass, Time).

The general functional relationship among these N physical quantities is written as:

$$f(Q_1, Q_2, Q_3, \ldots, Q_N) = 0$$

or alternatively:

$$Q_1 = F(Q_2, Q_3, \ldots, Q_N) \tag{A.1}$$

Demonstrating the validity of the Buckingham π-theorem is beyond the scope of this thesis; however, its fundamental steps will be outlined, and the methodology will be applied to relevant problems in fluid dynamics using SI units.

A.2.1 Definition

The Buckingham π-theorem states that if N is the number of dimensional physical quantities involved in a phenomenon, and K is the number of fundamental physical

dimensions (e.g., mass, length, time), then it is possible to construct $N - K$ independent dimensionless groups, called Π groups. Using these groups, the original dimensional relationship in Eq. A.1 can be reformulated in a dimensionless form:

$$F(\Pi_1, \Pi_2, \Pi_3, \ldots, \Pi_{N-K}) = 0$$

The Π_i groups are obtained by combining the original dimensional quantities Q_i into products of powers such that the resulting group is dimensionless. Each Π group is constructed from $K + 1$ dimensional variables, ensuring that the dimensional units cancel out:

$$\Pi_1 = F_1(Q_1, Q_2, Q_3, \ldots, Q_K, Q_{K+1})$$
$$\Pi_2 = F_2(Q_1, Q_2, Q_3, \ldots, Q_K, Q_{K+2})$$
$$\vdots$$
$$\Pi_{N-K} = F_{N-K}\left(Q_1, Q_2, Q_3, \ldots, Q_K, Q_{K+(N-K)}\right)$$

This transformation results in a reduction of the total number of variables in the physical problem, from N dimensional quantities to $N - K$ dimensionless groups. These Π groups are central to similarity analysis, enabling generalization of experimental results across different physical scales.

A.2.2 Structure of the Generic Adimensional Group Π_i

Each dimensionless group Π_i is constructed as the product of dimensional physical quantities, each raised to a suitable exponent. These exponents are determined through dimensional analysis. To justify the theorem, without delving into the detailed proof, consider Eq. A.2:

$$f(Q_1, Q_2, Q_3, \ldots, Q_N) = 0 \tag{A.2}$$

This relation can be reformulated in monomial form, where the dimensional quantities are raised to powers α_i:

$$\left[Q_1^{\alpha_1} \cdot Q_2^{\alpha_2} \cdot Q_3^{\alpha_3} \cdots Q_N^{\alpha_N}\right] = [1] \tag{A.3}$$

The exponents α_i must be chosen such that the resulting product is dimensionless. An obvious (but trivial) solution is $\alpha_1 = \alpha_2 = \cdots = \alpha_N = 0$.

Let $M, L, T, \ldots$ represent the K fundamental dimensions through which each quantity Q_i is expressed. For each physical quantity:

$$Q_1 = g_1(M, L, T, \ldots),$$
$$Q_2 = g_2(M, L, T, \ldots),$$
$$\vdots$$
$$Q_N = g_N(M, L, T, \ldots).$$

Substituting these into Eq. A.3 leads to:

$$\left[g_1(M, L, T, \ldots)^{\alpha_1} \cdot g_2(M, L, T, \ldots)^{\alpha_2} \cdots g_N(M, L, T, \ldots)^{\alpha_N} \right] = [1]$$

The equation is dimensionless if the overall exponents of all fundamental dimensions simply to zero. Under the International System, where $K = 3$ (length L, mass M, and time T), each of these must appear with an overall exponent equal to zero. Hence, each exponent is a function $H_j(\alpha_1, \alpha_2, \ldots, \alpha_N)$ of the α_i:

$$\left[M^{H_1(\alpha_1, \ldots, \alpha_N)} \cdot L^{H_2(\alpha_1, \ldots, \alpha_N)} \cdot T^{H_3(\alpha_1, \ldots, \alpha_N)} \right] = [1]$$

The condition for this product to be dimensionless is:

$$H_1(\alpha_1, \alpha_2, \ldots, \alpha_N) = 0,$$
$$H_2(\alpha_1, \alpha_2, \ldots, \alpha_N) = 0,$$
$$H_3(\alpha_1, \alpha_2, \ldots, \alpha_N) = 0.$$

Thus, K linear equations are obtained in N unknowns $\alpha_1, \ldots, \alpha_N$. Since $K < N$, the system is underdetermined. The K exponents can be expressed as functions of the remaining $N - K$ free parameters. Substituting these into Eq. A.3 allows the construction of $N - K$ independent, dimensionless groups:

$$\left[Q_1^{\alpha_1} \cdot Q_2^{\alpha_2} \cdot Q_3^{\alpha_3} \cdot \ldots \cdot Q_N^{\alpha_N} \right] = [1]$$

Dimensional analysis thus offers a systematic way to identify these groups and reduce the complexity of experimental or theoretical formulations. However, it does not guarantee that the correct physical variables have been selected, nor does it determine the specific form of the functional relationships between them [43].

In fluid mechanics and heat transfer, many widely used dimensionless numbers (e.g. the Reynolds, Nusselt, or Prandtl numbers) were derived through this approach. These form the basis of many empirical correlations. A list of the most common dimensionless groups used in fluid dynamics is provided in Table A.2.

The following section will present various practical examples that illustrate the construction and application of these dimensionless groups.

A.2.3   Example: Incompressible, Viscous Flow in a Horizontal Pipe with Convective Heat Transfer

This case study represents the typical flow and heat transfer conditions investigated in the present thesis. The dimensional analysis is performed on a pipe in which both hydrodynamic and thermal phenomena are present. For clarity, the analysis is separated into two parts: hydrodynamic similarity and convective heat transfer similarity.

Non-Dimensional Number	Definition	Physical Meaning	Typical Value
Reynolds	$Re = \dfrac{\rho u L}{\mu}$	Inertial forces / Viscous forces	$\gg 1$
Mach	$M = \dfrac{u}{c}$	Inertial forces / Compressibility forces	~ 1
Prandtl	$Pr = \dfrac{c_p \mu}{k}$	Momentum diffusivity / Thermal diffusivity	~ 1
Nusselt	$Nu = \dfrac{hL}{k}$	Convective / Conductive heat transfer	$\gg 1$
Stanton	$St = \dfrac{Nu}{Re \cdot Pr} = \dfrac{h}{\rho u c_p}$	Heat transfer rate / Fluid thermal capacity	$\ll 1$
Schmidt	$Sc = \dfrac{\mu}{\rho D_2}$	Momentum diffusivity / Mass diffusivity	~ 1

Table A.2: Common dimensionless groups in fluid dynamics

A.2.3.1   Hydrodynamic Similarity

In this case, the primary interest lies in evaluating the pressure drop between the pipe's inlet and outlet. The geometry is characterized by a length l, a hydraulic diameter D_h, and a surface roughness k. The relevant flow properties include the fluid density ρ, dynamic viscosity μ, and bulk velocity $\overline{U}$. Therefore, the pressure drop Δp is assumed to depend on the following variables:

$$\Delta p = f\left(l, D_h, k, \rho, \mu, \overline{U}\right)$$

Obtaining a general correlation based directly on these variables would require a large number of experiments. For example, testing five values for each variable would result in $5^6 = 15625$ possible configurations. To reduce the complexity, the number of parameters can be decreased using dimensional analysis. Here, $N = 7$ dimensional variables and $K = 3$ fundamental dimensions (mass M, length L, time T) are present. According to the Buckingham π-theorem, the system can be reduced to $N - K = 4$ dimensionless groups:

$$\begin{cases} \Pi_1 = \dfrac{\Delta p}{\frac{1}{2}\rho \overline{U}^2} & \text{(pressure drop ratio)} \\[2ex] \Pi_2 = \dfrac{l}{D_h} & \text{(geometry ratio)} \\[2ex] \Pi_3 = \dfrac{k}{D_h} & \text{(relative roughness)} \\[2ex] \Pi_4 = \dfrac{\overline{U}\rho D_h}{\mu} & \text{(Reynolds number)} \end{cases}$$

The dimensional relationship can now be rewritten as:

$$g\left(\Pi_1, \Pi_2, \Pi_3, \Pi_4\right) = \text{const}$$

Solving for Π_1, and recognizing Π_4 as the Reynolds number Re yields the following equation:

$$\frac{\Delta p}{\frac{1}{2}\rho \overline{U}^2} = F\left(\frac{l}{D_h}, \frac{k}{D_h}, Re\right)$$

In fully developed pipe flow, the function F becomes linear in $\Pi_2 = l/D_h$, and the commonly used friction factor f_D is defined as:

$$f_D = \frac{\Delta p / l}{\frac{1}{2}\rho \overline{U}^2 / D_h} = f_D\left(\frac{k}{D_h}, Re\right)$$

Thus, experiments are needed only to establish the empirical relationship between f_D, Re, and k/D_h. By ensuring both geometric and hydrodynamic similarity, experimental data can be extrapolated to full-scale systems.

A.2.3.2 Convective Heat Transfer Similarity

In convective heat transfer problems, the quantity of interest is the convective heat flux q, rather than the total heat transfer Q. In forced convection regimes, typical of high-speed flows in turbine cooling ducts, the influence of buoyancy (natural convection) is negligible.

The heat flux depends on the following variables:

- hydraulic diameter of the duct, D_h;

- heat transfer surface area, A;

- wall temperature distribution, T_w;

- bulk fluid temperature, T_∞;

- velocity field, u;

- thermophysical properties: thermal conductivity k, specific heat at constant pressure c_p, density ρ, and dynamic viscosity μ.

Assuming fixed geometry and temperature-independent properties, the heat flux can be written as:

$$q = f\left(D_h, A, T_w, T_\infty, k, c_p, \rho, \mu\right)$$

To reduce complexity, Newton's law of cooling is introduced:

$$q = h\left(T_w - T_\infty\right)$$

where h is the convective heat transfer coefficient. Although this relationship is not derived from first principles, it is experimentally validated and widely adopted in engineering applications.

The heat transfer coefficient h depends on:

$$h = f\left(D_h, k, c_p, \rho, \mu\right)$$

The associated dimensionless groups are:

$$
\begin{cases}
\Pi_1 = \dfrac{hD_h}{k} & \text{(Nusselt number)} \\[2ex]
\Pi_2 = \dfrac{c_p\mu}{k} & \text{(Prandtl number)} \\[2ex]
\Pi_3 = \dfrac{\rho u D_h}{\mu} & \text{(Reynolds number)}
\end{cases}
$$

Hence, the general form of the convective heat transfer correlation becomes:

$$f\left(Nu, Pr, Re\right) = 0 \quad \Rightarrow \quad Nu = f\left(Pr, Re\right)$$

If other factors such as friction or geometric parameters are significant, the correlation can be extended as:

$$Nu = f\left(Pr, Re, f_D, \frac{l}{D_h}\right)$$

This formulation highlights the role of experimental studies in determining valid empirical correlations, allowing reliable predictions of convective heat transfer behavior under dynamically similar conditions.

Nomenclature

Acronyms / Abbreviations

Symbol	Description
AM	Additive Manufacturing
CAD	Computer-Aided Design
CFD	Computational Fluid Dynamics
CT	Computed Tomography
DA	Dimensional Analysis
DNS	Direct Numerical Simulation
FOV	Field of View
HTC	Heat Transfer Coefficient
IR	Infrared
L-PBF	Laser Powder Bed Fusion
LBGT	Land-Based Gas Turbine
MCM	Monte Carlo Method
PIV	Particle Image Velocimetry
QSSHT	Quasi-Steady State Heat Transfer
ROI	Region of Interest
SEM	Scanning Electron Microscope
SLA	Stereolithography
SRHT	Single Roughness Heat Transfer
TIT	Turbine Inlet Temperature
TO	Test Object
TSM	Taylor Series Method

Dimensionless Numbers

Symbol	Description	Definition
C_f/C_{fS}	Friction factor enhancement	$\dfrac{C_f}{C_{fS}}$
k_s^+	Roughness height in viscous units	$\dfrac{k_s u_\tau}{\nu}$
Nu	Nusselt number	$\dfrac{hD_h}{k}$
Nu/Nu_S	Nusselt enhancement factor	$\dfrac{Nu}{Nu_S}$
Pr	Prandtl number	$\dfrac{c_p\mu}{k}$
Pr_t	Turbulent Prandtl number	$\dfrac{\varepsilon_M}{\varepsilon_H}$
Re	Reynolds number	$\dfrac{UD_h}{\nu}$
St	Stanton number	$\dfrac{h}{\rho u c_p}$
TPF	Thermal performance factor	$\dfrac{Nu/Nu_S}{(C_f/C_{fS})^{1/3}}$
x/D_h	Dimensionless streamwise coordinate	$\dfrac{x}{D_h}$

Symbols

Symbol	Description	Dimensions	Units
A	Cross-sectional area	L^2	m^2
α	Thermal diffusivity	$L^2 \cdot T^{-1}$	m^2/s
C_f	Skin-friction coefficient	–	1
D_h	Hydraulic diameter	L	m
δ	Momentum Bounadry Layer Thickness	L	m
δ_T	Thermal Bounadry Layer Thickness	L	m
$\Delta\theta^+$	Temperature shift in wall units	–	1
ΔU^+	Velocity shift in wall units	–	1
ε_H	Thermal eddy diffusivity	$L^2 \cdot S^{-1}$	m^2/s
ε_M	Momentum eddy diffusivity	$L^2 \cdot S^{-1}$	m^2/s

f_D	Darcy friction factor	–	1
h	Convective heat transfer coefficient	$M \cdot T^{-3} \cdot \Theta^{-1}$	W/(m^2 K)
k	Thermal conductivity	$M \cdot L \cdot T^{-3} \cdot \Theta^{-1}$	W/(m K)
k_s	Equivalent sand-grain roughness height	L	m
L	Length of the test section	L	m
λ_f	Frontal solidity	–	1
μ	Dynamic viscosity	$M \cdot L^{-1} \cdot T^{-1}$	Pa s
ν	Kinematic viscosity	$L^2 \cdot T^{-1}$	m^2/s
$\dot{q}$	Heat flux	$M \cdot T^{-3}$	W/m^2
σ_{angle}	Uncertainty due to camera inclination	–	1
σ_{Nu}	Standard deviation of global Nusselt number	–	1
σ_{rep}	Uncertainty due to test repeatability	–	1
τ_w	Wall shear stress	$M \cdot L^{-1} \cdot T^{-2}$	Pa
T	Absolute Temperature	Θ	K
T_w	Wall Surface Temperature	Θ	K
T_∞	Bulk Temperature	Θ	K
θ^+	Non-dimensional temperature in inner units	–	1
$\overline{U}$	Bulk velocity	$M \cdot T^{-1}$	m/s
U^+	Non-dimensional velocity in inner units	–	1
y^+	Wall-normal coordinate in inner units	–	1

Subscripts

Symbol	Description
S	Reference smooth surface

Superscripts

Symbol	Description
$+$	Wall unit (dimensionless) scaling